UCLouvain

AGRO LOUVAIN

Faculté des bioingénieurs

Modelling the response of forests to climate change: the impact of drought.

The case of Walloon forests simulated with the HETEROFOR model

Auteur : Jérôme Bruneau
Promoteur(s) : Hugues Goosse, Mathieu Jonard
Lecteur(s) : Valentin Couvreur, François Massonnet
Année académique 2025-2026
Mémoire de fin d'études présenté en vue de l'obtention du diplôme de Bioingénieur : Bioingénieur en sciences et technologies de l'environnement, à finalité spécialisée

Remerciements

Je tiens à remercier chaleureusement mes promoteurs, Hugues Goosse et Mathieu Jonard, pour leur accompagnement tout au long de ce travail, depuis la définition du sujet jusqu'aux nombreuses réunions et réponses qu'ils m'ont apportées durant toute cette année.

Je remercie également Frédéric André, François de Coligny et Arthur Guignabert, qui ont pris le temps de répondre à mes questions chaque fois que j'en ai eu besoin au cours de l'année.

Author Contributions

Role	Jérôme Bruneau	Other contributor(s)	Artificial intelligence
Conceptualization	Co-development of the topic and objectives, throughout the year	H. Goosse and M. Jonard: co-development of the topic and objectives	
Methodology	Design of the research protocol, with the promoters	H. Goosse (climate component) and M. Jonard (HETEROFOR component): methodological design	
Investigation	Literature search, implementation of HETEROFOR simulations, data collection and processing		
Formal analysis	Design of the statistical analyses, on the advice of the promoters	Methodological guidance (H. Goosse, M. Jonard)	AI (Claude): assistance writing the Python code used to implement the statistical analyses
Validation	Verification and interpretation of the results	Critical review of the results (H. Goosse, M. Jonard)	
Writing – original draft	Writing of the first draft of the manuscript		Translation tool (DeepL): assistance with certain English translations
Writing – review & editing	Revision and correction of content and form	Critical review (H. Goosse, M. Jonard)	AI (Claude): assistance with rewording and style improvement
Visualization	Design of the figures	Guidance on visualization choices (H. Goosse, M. Jonard)	AI (Claude): assistance writing the Python code used to generate the figures
Supervision		Hugues Goosse and Mathieu Jonard	

Table of contents

1. Introduction 1
1.1 Climate change in Europe: observations, drivers and modelling challenges 2
1.1.1 Global temperature and precipitation trends 2
1.1.2 Increased frequency of droughts and climate extremes 2
1.1.3 Accelerated warming in Europe : observations and spatial heterogeneity 3
1.1.4 Drivers of accelerated warming in Europe 4
1.1.5 Discrepancy between climate models and observations, and implications for projections 5
1.2 Impacts of climate change on forests 7
1.2.1 Physiological responses of trees to climate change 7
1.2.2 Observed impacts on European forest productivity 8
1.2.3 Specific vulnerability of Walloon forests 10
1.3 Process-based forest modelling for climate impact assessment 10
1.3.1 The need for forest models in a context of climate changes 10
1.3.2 The main approaches to modelling forest growth 11
1.4 Objectives 13
2. Material and methods 14
2.1. Study sites and stands 14
2.2 HETEROFOR model 15
2.2.1 Modules 15
2.2.2. Parametrization 17
2.3. Climate data 17
2.4. Simulation design 19
2.5. Model evaluation 20
2.6. Statistical analyses 20
3. Results 22
3.1 General responses to climate change 22
3.1.1 Model evaluation 22
3.1.2 Water stress indicator robustness 23
3.1.3 Effect of atmospheric CO_2 concentration 25
3.1.4 Effect of the cavitation module 26
3.2 Mechanisms and drivers of forest responses to climate change 28
3.2.1 Site and species effects on water stress and NPP 28
3.2.2. Climatic drivers of forest indicators 30
3.2.3. Interacting effects of temperature and water stress on NPP 32

3.2.4. Relationship between water stress and defoliation 36
3.3 Evolution of climate extremes 38
3.3.1 Changes in distributions 38
3.3.2 Impact of extreme dry years on productivity 39
3.3.3 Temporal dynamics and underlying mechanisms of NPP decline 41
3.3.4 Seasonality and duration of drought episodes 43
3.4 Climate model biases and their propagation into HETEROFOR 44
3.4.1 Climatic bias between GFDL-ESM4 and IRM interpolation 44
3.4.2 Propagation of climate trend biases into HETEROFOR simulations 46
3.4.3. Disentangling the effect of temperature level from trend 50
4. Discussion 53
4.1 Model performance 53
4.2 General responses to climate change: water stress, CO_2 fertilisation and structural inertia 54
4.3 Site and species variability: the role of soil buffering capacity and hydraulic strategies 55
4.4 Temperature-NPP regime shift 57
4.5 From episodic to chronic drought: implications for forest vulnerability 59
4.6 Climate model biases and their implications for projections 60
4.6.1. Separating climate change from climate source 60
4.6.2. The structural limits of trend correction in ISIMIP3 61
4.6.3. Heterogeneous propagation mechanisms across sites and indicators 61
4.6.4. Implications for the interpretation of future projections 62
4.7 Limitations and research perspectives 63
Conclusion 65
References 67
Appendix A : 74
Appendix B : 77
Appendix C 85
Appendix D 86
Appendix E 87
Appendix F 91
Appendix G 94
Appendix H 96
Appendix I 98
Appendix J 102

List of figures

Figure 1. Projected changes in drought frequency (DRF; number of drought events per decade, top panels), extreme drought frequency (ExDRF; number of extreme drought events per decade, middle panels), and drought severity (DRS; average severity of drought events, bottom panels) between the near future (2041-2070) and the recent past (1981-2010), averaged over 11 climate model simulations at the 12-month accumulation scale. Left panels show results under RCP4.5 and right panels under RCP8.5. Positive values indicate an increase relative to the reference period. Adapted from Spinoni et al. (2018). _____ *3*

Figure 2. Linear trends in surface air temperature (SAT, °C per decade) over the period 1979-2022 based on ERA5 reanalysis. Panels (a) and (b) show absolute SAT trends in winter (DJF) and summer (JJA), respectively. Panels (c) and (d) show the ratio of local SAT trends to the global mean trend for the same seasons. The black rectangle delimits the European region used for averaging. Dots indicate trends significantly different from zero at the 10% level (Mann-Kendall test). Adapted from Dong & Sutton (2025).4

Figure 3. Observed and simulated summer warming over Western and central Europe (1980-2022). (a) Observed change in mean summer temperature (ERA5). (b) Difference between the CORDEX model median and ERA5, showing the underestimation of summer warming by regional climate models. (c, d) Time series of cumulative summer warming in Western and central Europe for CORDEX (n=49) and CMIP6 (n=43) ensembles compared to ERA5 observations; the model median, 5th-95th percentile range, and hottest realization are shown. (e) Total warming trends (°C per decade) for all seasons and annual mean; observed values (ERA5 and E-OBS) consistently exceed both CORDEX and CMIP6 model distributions. (Schumacher et al., 2024). _____ *6*

Figure 4. Projected relative changes in European beech (Fagus sylvatica) basal area increment (BAI, in %) compared to the 1986-2016 reference period, under SSP1-2.6 (a-c) and SSP5-8.5 (d-f) CMIP6 climate scenarios for three future periods: 2020-2050 (a, d), 2040-2070 (b, e), and 2060-2090 (c, f). Negative values (red) indicate growth decline. The most severe declines are projected towards the Southern distribution limit of the species under the high-emission scenario. From Martinez del Castillo et al. (2022). _____ *9*

Figure 5. Location of the five study stands across three sites in Wallonia, Belgium, and their respective bioclimatic zones (Van der Perre et al., 2015) _____ *14*

Figure 6. HETEROFOR model evaluation for (a) soil water dynamics (relative extractable water, REW) and (b) circumference increment. Each point represents one site × configuration combination (filled circles = no cavitation module, open triangles = cavitation module). Colours indicate the site (green = Baileux beech, purple = Baileux oak, orange = Chimay). The x-axis shows the mean bias (simulated − observed) and the y-axis the root mean square error (RMSE). Points closer to the origin indicate better model performance. Detailed metrics by horizon and species are provided in Appendix A . _____ *22*

Figure 7. Relationship between water stress, expressed as the number of days per year with REW below 0.32, and the relative transpiration deficit (ratio of transpiration deficit to potential transpiration), for all plot-years under the constant-CO_2 scenarios. Colour indicates site (Baileux, Chimay, LLN); marker shape indicates species (circle = beech, cross = oak). _____ *24*

Figure 8. Distributions of NPP (a), water stress (b), stand volume (c) and basal area (d) under two CO_2 scenarios across all stands, in historical and future period. Box limits represent the 25th and 75th percentiles (interquartile range), the horizontal line indicates the median, whiskers extend to 1.5× the interquartile range, and points beyond whiskers are individual outliers. Different letters above boxplots

indicate significant differences between scenarios (Tukey HSD, $p < 0.05$). Without the cavitation module. _____ *25*

Figure 9. Defoliation distributions under the two CO_2 scenarios (constant and variable) across all stands, without the cavitation module. _____ *26*

Figure 10. Effect of the cavitation module on water stress (a), NPP (b) and defoliation (c) across all stands. Scenarios with and without the cavitation module use a constant CO_2 concentration (317.8 ppm). _____ *27*

*Figure 11. Empirical cumulative distribution functions (ECDF) of defoliation across all plots and years, for four scenarios combining period (historical 1961-2024 vs future 2025-2100) and cavitation module (enabled vs disabled), under constant CO_2 conditions. Filled circles indicate the 90th percentile of each distribution.*_____ *28*

*Figure 12. Site and species effects on water stress (a-b) and NPP (c-d) under historical and future CO_2 constant scenarios, without cavitation.*_____ *29*

Figure 13. Spearman correlations between climatic variables and forest indicators across all stands, without cavitation. Filled symbols indicate significant correlations ($p < 0.05$). _____ *31*

*Figure 14. NPP vs water stress for all stands under CO_2 constant scenarios, without cavitation. Colour indicates mean summer temperature. Dashed line = linear regression, drawn when the correlation is statistically significant. * $p < 0.05$.*_____ *33*

Figure 15. Relationship between net primary productivity (NPP) and mean summer temperature for each plot, distinguished by water stress class (defined by tertiles). Blue = low stress, orange = medium stress, red = high stress. Circles = historical period (1961-2024), triangles = future period (2025-2100). Solid lines indicate statistically significant regressions ($p < 0.05$), dashed lines indicate non-significant regressions. Stress tercile thresholds (in days/year) are indicated in the panel titles. All simulations use a constant CO_2 concentration. _____ *34*

*Figure 16. Defoliation vs water stress for all stands under CO_2 constant scenarios, without cavitation. Colour indicates mean summer temperature. Dashed line = linear regression, drawn when the correlation is statistically significant. * $p < 0.05$.*_____ *36*

Figure 17. Historical vs future distributions of water stress (a), NPP (b) and defoliation (c) across all stands, without cavitation, at constant CO2. Dashed lines indicate medians. _____ *38*

Figure 18. NPP in dry vs normal years for all stands, without cavitation and with constant CO2. Dry years defined as years exceeding the 90th percentile of water stress, computed separately for each period. __ *40*

*Figure 19. Mean time series of net primary productivity (NPP, dark blue) and gross primary productivity (GPP, light blue dashed), leaf area index (LAI, green) and transpiration deficit (purple dashed) averaged across all five plots, under constant CO_2 scenarios (1961-2100). Thin lines show annual values; thick lines show 10-year moving averages. The vertical dotted line indicates the transition between the historical period (1961-2024, IRM observed climate data) and the future period (2025-2100, GFDL-ESM4 climate simulations).*_____ *41*

Figure 20. Temporal evolution of mean summer temperature (June-August) as simulated by GFDL-ESM4 and interpolated from IRM observations for the three study sites (1961-2024). Solid lines show annual values, dashed lines show 10-year moving averages. _____ *44*

Figure 21. Temporal evolution of total summer precipitation (June-August) as simulated by GFDL-ESM4 and interpolated from IRM observations for the three study sites (1961-2024). The annotated bias corresponds to the mean difference over the full period, expressed in mm and as a percentage of the observed mean. _____ *45*

Figure 22. Comparison of trend slopes (1961-2024) between IRM- and GFDL-ESM4-forced simulations, without cavitation, for water stress days (A), NPP (B), and total defoliation (C). For each site × species, the grey point represents the IRM slope and the red diamond the GFDL-ESM4 slope, connected by a segment whose colour indicates whether GFDL-ESM4 amplifies (red) or attenuates (blue) the trend observed under IRM; a dashed grey segment indicates that at least one of the two slopes is not statistically significant ($p \geq 0.05$). An asterisk above a point indicates that the corresponding slope is individually significant ($p < 0.05$), regardless of the other. _____ *47*

Figure 23 : Slope difference (GFDL-ESM4 − IRM) by 20-year block, without cavitation, for water stress days (A), NPP (B), and total defoliation (C). Blocks are anchored from 2024 backwards in time so as not to truncate the most recent years. Red shades indicate a stronger slope under GFDL-ESM4 than under IRM, blue shades the reverse. An asterisk next to a value indicates that both the IRM and GFDL-ESM4 slopes are statistically significant ($p < 0.05$) for that block. _____ *48*

Figure 24 : Sensitivity of each indicator to warming (ratio of the indicator's slope to the corresponding summer temperature slope), compared between IRM and GFDL-ESM4, without cavitation. Each point represents a site × species × indicator combination (circle: water stress days; square: NPP; triangle: total defoliation). The left panel shows the full range of values, the right panel a zoom on the cluster of values near zero (delimited by the dashed box in the left panel). The diagonal ($y = x$) represents a response perfectly proportional to the rate of warming, identical under both forcings. Filled, black-outlined points correspond to cases where all four quantities involved (slope of the indicator and slope of temperature, for IRM and for GFDL-ESM4) are statistically significant; pale, not outlined points indicate that at least one of these four values is not. A gold outline indicates a sign change in sensitivity between IRM and GFDL-ESM4. _____ *49*

Figure 25 : Trend slope (1961-2024) under three successive climate configurations, without cavitation: IRM (observed climate), IRM+bias (IRM's trend and interannual variability, with mean temperature level adjusted to that of GFDL-ESM4), and GFDL-ESM4, for water stress days (A), NPP (B), and total defoliation (C). The first segment (solid line) isolates the effect of temperature level alone; the second segment (dashed line) isolates a residual effect once this level is equalised, including in particular the climate trend. Each colour represents a site × species combination (see legend). Filled markers indicate a statistically significant slope ($p < 0.05$), open markers a non-significant slope. _____ *51*

List of tables

Table 1. Main stand characteristics at the start of the simulations (1961), based on field inventories conducted between 1999 and 2001. The same inventory file was used to initialise both the historical (1961-2024) and future (2025-2100) simulations. _____ *15*

Table 2. Overview of all datasets used in this study, including their source, temporal coverage, resolution and purpose. Daily climate data were disaggregated to hourly resolution using empirical coefficients calibrated as part of the REGE+ project (André et al., 2025). _____ *18*

Table 3. Overview of the eight simulation designs used in this study. _____ *19*

Table 4. Daily agreement between observed (TDR) and simulated relative extractable water (REW) in classifying growing-season days as water stress days (REW < 0.32), at Baileux (beech, oak) and Chimay, under the reference configuration without cavitation. Sensitivity and specificity indicate, respectively, the proportion of observed stress days correctly identified by the model and the proportion of observed non-stress days correctly identified. Cohen's kappa quantifies the agreement between the two classifications beyond what would be expected by chance alone (Landis & Koch, 1977). _____ *24*

*Table 5. Spearman correlations between water stress (days/year) and cavitation-driven defoliation across all plots, for the historical (1961-2024) and future (2025-2100) periods, with the cavitation module activated. * indicates significant correlation (p < 0.05); n.s. = non-significative.* _____ *37*

1. Introduction

Forests cover about 30% of the earth's surface and play a central role in the functioning of the biosphere. Beyond their direct economic value as a source of wood and non-wood products, forests provide a wide range of ecosystem services that are essential to both environmental sustainability and human wellbeing. These services include carbon sequestration, regulation of hydrological processes, biodiversity conservation, soil protection and recreational benefits (André et al., 2025; Farooqi et al., 2020; Harrison et al., 2014; Nolander & Lundmark, 2024). Their role in the global carbon cycle is particularly crucial. The global forest carbon sink, which has remained stable at around 3.5 to 3.6 Pg C per year over the last three decades, compensates for nearly half of current emissions from fossil fuels, making forests an indispensable buffer against climate change (Pan et al., 2024). In Wallonia, forests cover about 560,000 hectares, nearly one third of the territory, and constitute an economic and ecological heritage whose sustainability depends on the ability of forest managers to adapt to constantly changing conditions.

However, this capacity for adaptation is severely tested by the acceleration of climate change. Over the past four decades, Europe has warmed at more than twice the global average rate, with summer temperatures rising particularly sharply (Douville et al., 2025). This warming is accompanied by an increase in the frequency and intensity of extreme events like heatwaves, prolonged droughts, and combined hot-dry episodes, which are already leaving visible traces on European forest ecosystems. The droughts of 2003, 2018 and 2022 illustrated the extent of the damage that trees can suffer when exposed simultaneously to high temperatures and severe water deficits (Tijerín-Triviño et al., 2025). More broadly, increasing rates of tree mortality, canopy dieback and productivity decline have been documented across European forests over recent decades, with canopy mortality having approximately doubled since the 1980s (Senf et al., 2018, 2020). For example, in Wallonia, spruce stands, which represent about a quarter of the regional forest, have already suffered massive die-offs following the combined effects of drought, storms, and bark beetle infestations (André et al., 2025). These recent episodes are therefore not isolated incidents but rather early signals of a trajectory that projections suggest will intensify considerably over the coming decades. Faced with these challenges, forest managers must make long-term decisions about species composition, stand structure and silvicultural practices, whose consequences will only be visible decades later and whose effectiveness depends heavily on accurate projections of future climatic conditions.

Yet, despite growing evidence of climate impacts on forests at the European scale, the precise quantification of these effects at the scale of individual Walloon stands remains insufficiently documented. Broad-scale studies do not fully capture species-specific responses, stand structural heterogeneity, local soil properties or the specific climatic trajectory of the region.

To assess future forest vulnerability, climate projections are commonly used as inputs for forest impact models. These models simulate tree growth, mortality, regeneration and ecosystem functioning under future climatic conditions. Their outputs are therefore strongly dependent on the quality of the climate data used as forcing. Even relatively small biases in temperature or precipitation can propagate through models and influence projections of forest productivity, drought stress or species suitability. However, these projections are themselves subject to systematic biases that can lead to an underestimation of future warming and the severity of droughts, which raises important questions about the reliability of the resulting impact projections.

State of the art

1.1 Climate change in Europe: observations, drivers and modelling challenges

1.1.1 Global temperature and precipitation trends

Since the pre-industrial era, the Earth's climate system has undergone unprecedented changes, mainly attributable to anthropogenic greenhouse gas emissions. According to the IPCC's Sixth Assessment Report (AR6), average global surface temperature increased by 1.1°C (± 0.1°C) between the 1850-1900 period and the 2011-2020 decade (IPCC, 2021). Each of the last four decades has been hotter than the previous one, and the rate of warming since 1970 has reached 0.18 °C per decade (Hansen et al., 2023).

This warming is not spatially uniform, with stronger increases over land than over oceans, which is consistent with differences in heat capacity, evaporative cooling, and land-atmosphere feedbacks (IPCC, 2021). The Arctic is experiencing the most significant warming, with an increase of up to +3 °C since the 1980s (Rantanen et al., 2022), while the tropics and the Southern hemisphere are warming more slowly. Europe and the Northern hemisphere mid-latitudes show warming rates above the global average (Douville et al., 2025; Yin et al., 2024)

Global rainfall is also affected. On average, it increases by between 1 and 3% per degree Celsius of global warming (IPCC, 2021), but the trends vary greatly between regions. An increase in rainfall has been observed at middle and high latitudes in the Northern hemisphere since the mid-20th century, while several subtropical regions like the Mediterranean basin, Southern Africa and parts of South America are recording a decline (IPCC, 2021). These contrasts are partly explained by the global hydrological cycle. A warmer atmosphere can retain more moisture (about 7% per degree Celsius, in accordance with the Clausius-Clapeyron relationship), which intensifies the water cycle and tends to accentuate the existing contrasts between humid and dry regions (Held & Soden, 2006). Extreme precipitation events have also most likely intensified over the majority of land areas (IPCC, 2021).

1.1.2 Increased frequency of droughts and climate extremes

Global warming is accompanied by a marked change in the frequency and intensity of extreme weather events. The frequency and severity of agricultural and ecological droughts have increased across Europe over recent decades, particularly in Southern and Western regions, a trend observed since the mid-20th century and especially pronounced during summer months (Hanel et al., 2018; Spinoni et al., 2018). Long-term reconstructions reveal unprecedented drying trends in soil moisture, largely associated with rising temperatures and enhanced evaporative demand (Hanel et al., 2018). These trends are expected to intensify in the future, with projections indicating up to a 40% increase in drought-affected area under a +3°C warming scenario compared to 1.5°C warming (Samaniego et al., 2018). Moreover, the probability of compound events combining long drought duration and extreme heat has significantly increased across Europe over the period 1950-2013, with rising temperatures identified as the main driver (Manning et al., 2019). Recent events such as the droughts of 2003, 2018 and 2022 are among the most intense in the last five centuries, with seasonal temperatures exceeding historical averages by 3°C to 5°C (Schumacher et al., 2024). The summer of 2022 was particularly extreme, with 63% of European territory on drought alert and historically low soil moisture levels (River Discharge | Copernicus, 2022). These episodes illustrate the convergence between heat and water deficit, whose combined effects on forest ecosystems are of particular concern. Marchi et al. (2024) show that the

probability of having a hot day during drought increases with the duration of the drought, and that Walloon forests are particularly vulnerable when they are simultaneously confronted with a heat wave and a water deficit.

Future projections indicate that these observed trends will continue and intensify further. In Europe, drought intensity is projected to be 2.8 times higher by 2061-2100 under the high-emission SSP585 scenario compared to the historical period, placing the region, along with the Amazon basin, among those facing the highest risk of future drought (Li et al., 2021). Spinoni et al. (2017) also project a significant increase in the frequency and severity of droughts in Southern and central Europe during the 21st century, regardless of season. As shown in Figure 1, these projected increases are particularly pronounced in Southern Europe and the Mediterranean basin under both scenarios (RCP4.5 and RCP8.5), with extreme drought frequency and severity intensifying substantially under RCP8.5. The contrast between the two scenarios highlights the strong dependence of future drought risk on the magnitude of greenhouse gas emissions. Furthermore, temperature and precipitation extremes are expected to intensify across the entire European continent, with marked regional contrasts (Cardell et al., 2020). Mediterranean regions would be particularly exposed to more frequent heat waves and reduced summer rainfall, while Northern regions could experience increased winter precipitation.

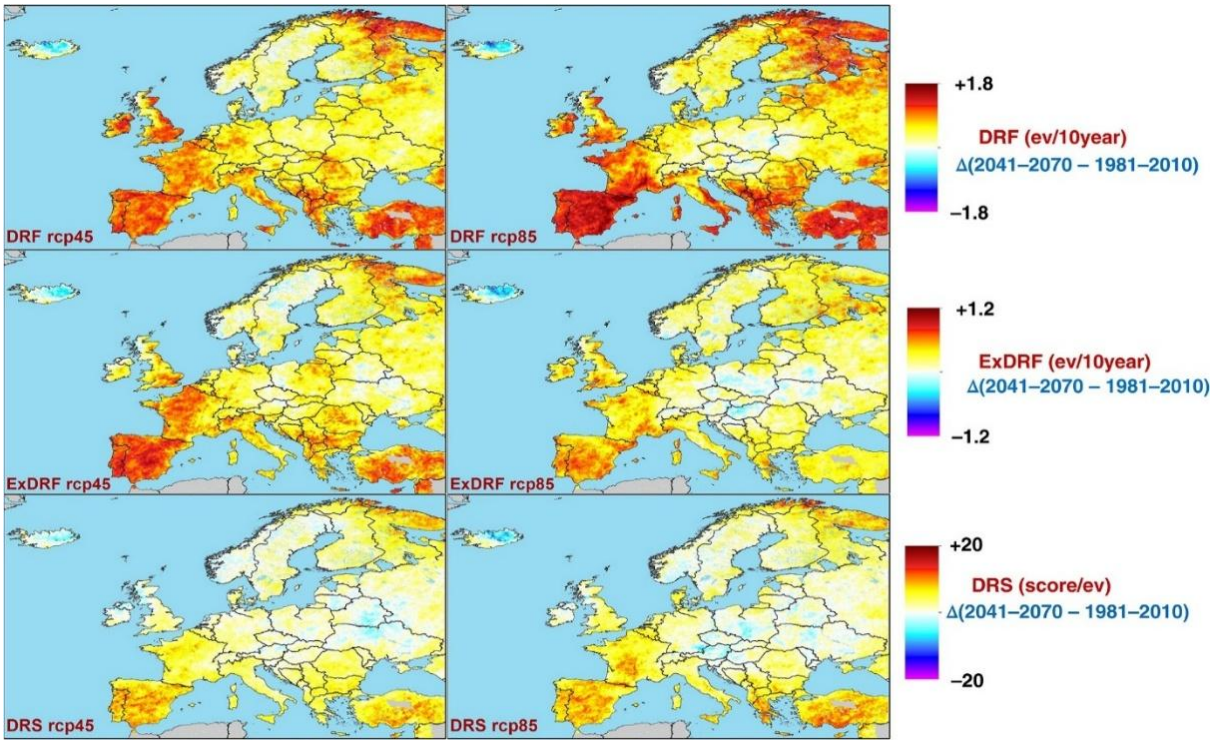

Figure 1. Projected changes in drought frequency (DRF; number of drought events per decade, top panels), extreme drought frequency (ExDRF; number of extreme drought events per decade, middle panels), and drought severity (DRS; average severity of drought events, bottom panels) between the near future (2041-2070) and the recent past (1981-2010), averaged over 11 climate model simulations at the 12-month accumulation scale. Left panels show results under RCP4.5 and right panels under RCP8.5. Positive values indicate an increase relative to the reference period. Adapted from Spinoni et al. (2018).

1.1.3 Accelerated warming in Europe : observations and spatial heterogeneity

Among the world's regions, Europe stands out for its particularly rapid warming, which consistently exceeds the global mean across multiple indicators. European surface air temperatures have warmed at around three times the global mean rate over the period 1979-2022, in both winter and summer (Dong & Sutton, 2025; Figure 2). This acceleration has been particularly pronounced in recent decades: since

the mid-1990s, European temperatures have risen by approximately 0.56°C per decade, more than double the global average rate of 0.27°C per decade over the same period (C3S/ECMWF & WMO, 2026). The intensification of heat extremes follows a similar pattern, with heatwave frequency increasing at more than twice the global rate (Yin et al., 2024).

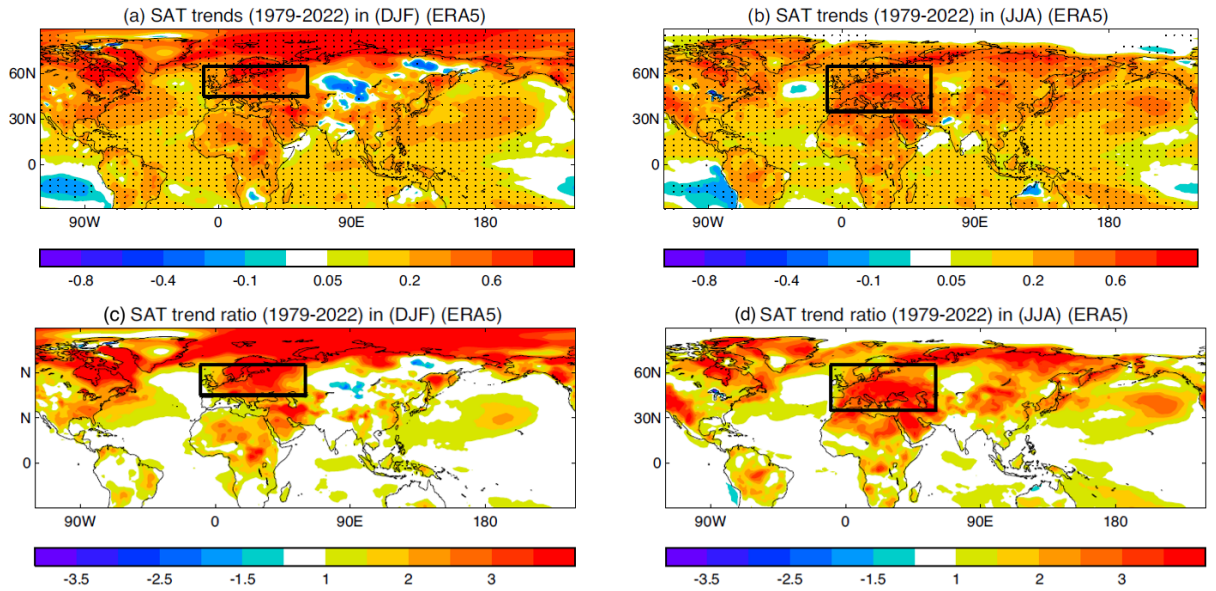

Figure 2. Linear trends in surface air temperature (SAT, °C per decade) over the period 1979-2022 based on ERA5 reanalysis. Panels (a) and (b) show absolute SAT trends in winter (DJF) and summer (JJA), respectively. Panels (c) and (d) show the ratio of local SAT trends to the global mean trend for the same seasons. The black rectangle delimits the European region used for averaging. Dots indicate trends significantly different from zero at the 10% level (Mann-Kendall test). Adapted from Dong & Sutton (2025).

Despite this overall warming signal, important regional differences exist across Europe. The strongest summer warming trends are observed in Southern and central Europe, whereas north-Eastern Europe experiences the most pronounced warming during winter and spring (Twardosz et al., 2021). Precipitation trends also display a marked north-south contrast, with decreasing rainfall observed in Southern and Western Europe and increasing precipitation in Northern regions (Caloiero et al., 2018). These spatial differences contribute to substantial regional disparities in drought exposure and climate vulnerability.

1.1.4 Drivers of accelerated warming in Europe

The accelerated warming observed in Europe results from the combined influence of external forcings and internal climate variability, which interact through several physical mechanisms.

Greenhouse gases are the main driver of Europe's long-term warming. The large ensemble simulations analysed by Deser & Phillips (2023) show that anthropogenic forcing accounts for most of the temperature increase in Europe, while internal variability modulates this trend at ±0.5°C over periods of 30 to 50 years. The decline in anthropogenic aerosol emissions since the 1980s is a second important factor, especially during summer. The reduction in aerosol optical thickness of about 50% in Central and Eastern Europe during the summer half-year (April-September), comparing the 1980s to the 2010s, led to an increase in incident solar radiation at the surface that could contribute up to about 1°C of additional warming in this region (Glantz et al., 2022). Dong & Sutton (2025) point out that aerosols are the main contributor to the thermodynamic component of excessive European warming in summer, while greenhouse gases dominate in winter. However, these radiative drivers alone do not fully explain the observed spatial and seasonal structure of European warming.

Atmospheric dynamics also play a major role in amplifying the warming observed in Western Europe. Recent studies show that persistent changes in atmospheric circulation, notably an increase in the frequency of meridional flows from the south, account for a significant proportion of the intensification of summer heatwaves and may help to explain why climate models underestimate the observed trends (Vautard et al., 2023). These circulation anomalies result in more frequent and persistent anticyclonic conditions, favouring subsidence, a reduction in cloud cover and an increase in solar radiation reaching the surface in Western Europe. Dong & Sutton (2025) estimate that approximately 29 ± 10 per cent of the amplification in European summer warming is attributable to these changes in circulation, while Yin et al. (2024) estimate this contribution at around 38 per cent for the trend in summer maximum temperatures. Using a different methodological approach based on the identification of time regimes, Carvalho-Oliveira et al. (2026) estimate that the increase in the frequency of southerly flows accounts for around 70 per cent of the excess summer warming (a metric that isolates regional deviation from global warming rather than the full warming trend) observed in Western Europe compared with the global average. These estimates, while consistent in identifying atmospheric circulation as a major contributor, vary substantially depending on the methodological approach used, highlighting the ongoing uncertainty in precisely quantifying this contribution.

One of the mechanisms proposed to explain these changes in circulation is the slowing of the Eurasian subtropical jet stream in summer. Dong et al. (2022) show that the summer slowdown of the Eurasian subtropical jet stream, which is largely attributed to the reduction in anthropogenic aerosol emissions, has altered meridional temperature gradients and favoured the establishment of circulation patterns conducive to summer warming.

Ocean variability, in particular the Atlantic Multi-Decadal Variability (AMV), also modulates European warming at the decadal scale. Deser et al. (2023) show that positive phases of the AMV tend to reinforce summer warming in Europe, and Yin et al. (2024) document the role of AMV-type sea surface temperature anomalies in amplifying summer temperatures and heatwaves through dynamic processes.

Overall, the literature converges towards the idea that these different mechanisms do not act independently. Atmospheric circulation changes and regional feedbacks are not mutually exclusive explanations for the amplified summer warming in Western Europe (Douville et al., 2025). This complexity has direct consequences for climate modelling. If current models fail to capture the full interplay between these mechanisms, they may systematically underestimate the observed warming.

1.1.5 Discrepancy between climate models and observations, and implications for projections

Current climate models tend to underestimate the amplification of warming observed in Western Europe over recent decades (since the early 1980s). Douville et al. (2025) show that CMIP6 models reproduce the average global warming relatively well, but systematically underestimate the intensity of summer warming in Western Europe, despite correctly simulating the global trend. This discrepancy is illustrated in Figure 3, where the observations and reanalyses (ERA5 and E-OBS) lie above almost all CORDEX (Coordinate Regional Climate Downscaling Experiment) and CMIP6 (Coupled Model Intercomparison Project Phase 6) simulations, particularly for the summer season and across central and Western Europe.

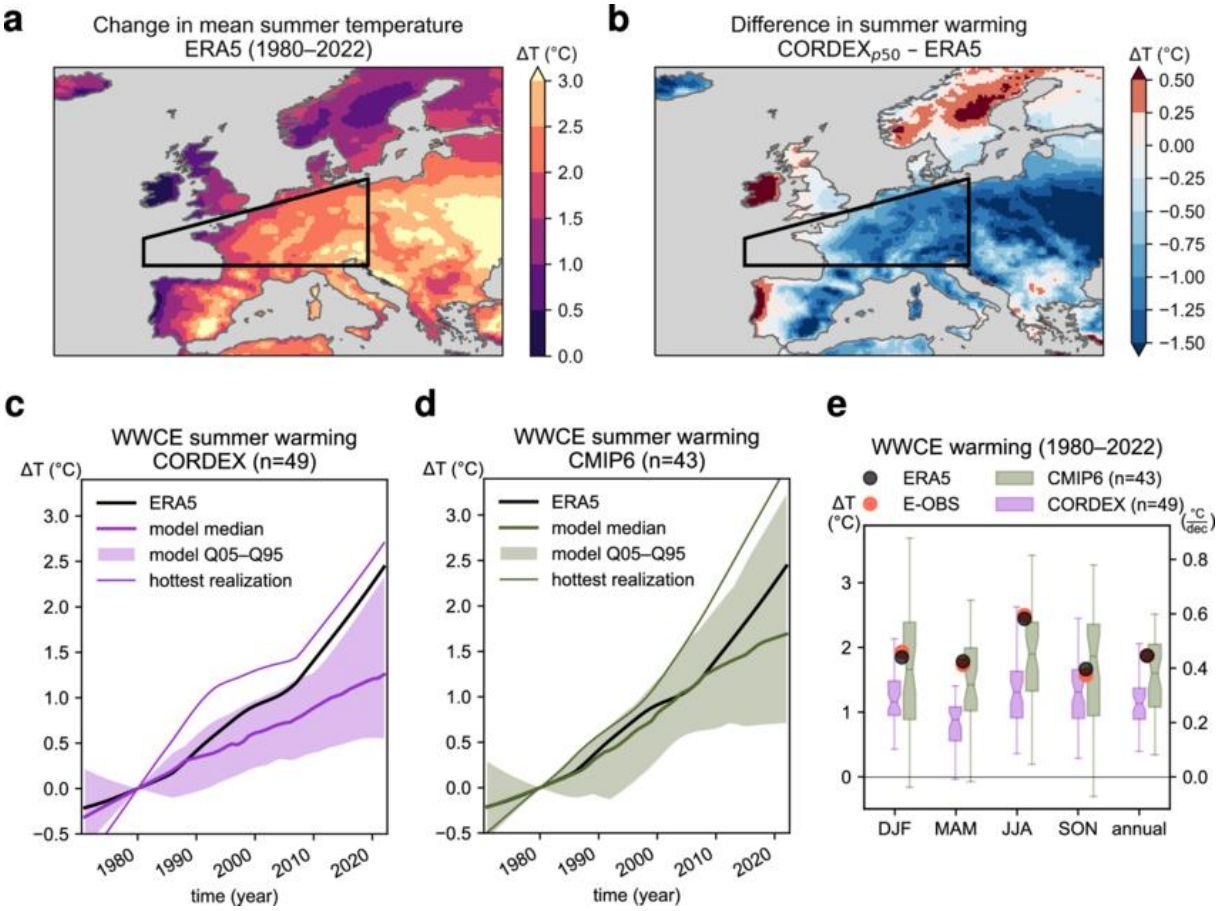

Figure 3. Observed and simulated summer warming over Western and central Europe (1980-2022). (a) Observed change in mean summer temperature (ERA5). (b) Difference between the CORDEX model median and ERA5, showing the underestimation of summer warming by regional climate models. (c, d) Time series of cumulative summer warming in Western and central Europe for CORDEX (n=49) and CMIP6 (n=43) ensembles compared to ERA5 observations; the model median, 5th-95th percentile range, and hottest realization are shown. (e) Total warming trends (°C per decade) for all seasons and annual mean; observed values (ERA5 and E-OBS) consistently exceed both CORDEX and CMIP6 model distributions. (Schumacher et al., 2024).

More specifically, Dong & Sutton (2025) quantify this bias by showing that although the total average warming over Europe may appear to be correctly reproduced in the ensemble average, this results from a balancing of errors between global warming that is sometimes overestimated and regional amplification that is underrepresented. Expressed in terms of European warming relative to global warming, the CMIP6 models underestimate this amplification by approximately 16 per cent in summer and 43 per cent in winter. Although the absolute discrepancy appears most visible in summer, this larger relative winter underestimate reflects the greater contribution of atmospheric circulation changes to excess warming in winter (40 ± 39%) compared to summer (29 ± 10%), a dynamical component that CMIP6 models consistently fail to capture in either season. Yin et al. (2024) obtain consistent results, showing that the observed increase in the frequency of heatwaves in Europe consistently exceeds that simulated by the CMIP6 models.

Several structural mechanisms may explain these discrepancies. Firstly, the representation of aerosols is a major source of uncertainty. Many models fail to accurately reproduce the observed decline in aerosol concentrations since the 1980s, leading to an underestimation of the increase in solar radiation at the surface (Nabat et al., 2025). Soil-atmosphere interactions also play an important role, with models generally underestimating soil drying and thus the strengthening of the positive feedback on summer temperatures (Douville et al., 2025).

Atmospheric circulation biases provide another important explanation for this discrepancy. Douville et al. (2025) show that standard climate models fail to accurately reproduce the observed summer trends in sea-level pressure over Europe, while atmospheric simulations constrained by reanalyses reproduce changes in circulation, as well as the associated surface warming, much more accurately. However, these simulations assimilate atmospheric observations and therefore do not constitute an independent validation of the models, but rather a tool for isolating the role of atmospheric circulation in the observed warming

Dong & Sutton (2025) also show that the circulation trends observed in both summer and winter lie outside the range of variability simulated by the CMIP6 ensemble, suggesting either an underestimation of the forced response of the circulation, an underestimation of low-frequency internal variability, or both.

Finally, several authors suggest that current models may also underestimate the response of atmospheric circulation to greenhouse gas forcing. If this is the case, the model-observation discrepancy would not necessarily disappear as aerosol forcing stabilizes but could persist, implying that future projections of European summer warming may be conservative (Vautard et al., 2023).

These limitations have direct implications for forest impact studies, where projections of summer temperature and water availability strongly influence simulations of tree growth, water stress and mortality. They also highlight the importance of properly characterising the biases and uncertainties in climate projections before using them as input data in forest models. Indeed, whether the biases relate to the representation of aerosols, soil-atmosphere feedback or atmospheric circulation, their consequences for future projections can vary considerably. Forest impact studies must therefore be interpreted in the light of these uncertainties, which can propagate throughout the modelling chain and influence the robustness of the resulting projections (Lindner et al., 2014).

1.2 Impacts of climate change on forests

1.2.1 Physiological responses of trees to climate change

Climate change affects tree functioning through changes in both mean climatic conditions and the increasing frequency of extreme events. Rising atmospheric CO_2, higher temperatures and more frequent droughts alter tree physiology, growth and survival through multiple interacting mechanisms.

Rising temperatures directly modify the phenology of trees. At the European level, spring phases have advanced and autumn senescence has been delayed, leading to a lengthening of the growing season by about 0.26 days per year over the 1951-2018 period, which is strongly attributable to winter and spring warming (Menzel et al., 2020). When enough water is available, this elongation promotes carbon assimilation and growth. The increase in atmospheric CO_2 concentrations also has a fertilising effect on forest productivity, a phenomenon that has been extensively documented in the literature. Higher CO_2 concentrations stimulate photosynthesis and primary production, though the magnitude of this response depends on ecosystem type and environmental conditions (Norby, 2025; Xu et al., 2025; Zhan et al., 2024). In his recent review, Norby (2025) synthesizes four decades of Free-Air CO_2 Enrichment (FACE) experiments and estimates that a CO_2 enrichment of 41% (approximately 550 ppm, expected around 2050 under SSP3-7.0) stimulates forest net primary productivity (NPP) by 21.8% on average, mainly through improved light-use efficiency. Independent evidence from eddy covariance observations across 38 extratropical forest sites corroborates this effect using a different methodological approach, with GPP stimulation rates of $16.4 \pm 4.2\%$ per 100 ppm CO_2 increase (Zhan et al., 2024).

This positive response is, however, not systematic. Xu et al. (2025) propose an integrated framework showing that the net fertilisation effect is constrained by a hierarchy of factors. Photosynthetic acclimation acts as a first limitation at the plant level, while nutrient availability (primarily nitrogen in temperate systems) emerges as the dominant long-term barrier, alongside interactions with the water cycle. Under conditions of prolonged drought or on poor soils, productivity gains may therefore be significantly reduced or even negated (Lévesque et al., 2014; Norby, 2025; Penuelas et al., 2011). The potential benefit associated with increased atmospheric CO_2 cannot therefore be considered in isolation from water constraints.

The potentially positive effects are increasingly being offset by the negative effects of global warming. Higher temperatures increase the atmosphere's evaporative demand and the vapour pressure deficit (VPD), which intensifies the risk of water stress, particularly during dry periods. In response to water stress, stomatal closure limits carbon assimilation while maintaining high temperature-related respiratory costs, leading to a decrease in net productivity. When stress is severe or prolonged, the risk of xylem embolism increases, which can cause the crown to dry out, lead to the death of twigs, or even result in the death of the tree following repeated episodes (Marchi et al., 2024). At the European level, the combined effect of heat and drought has become one of the main factors reducing tree growth and increasing tree mortality (Tijerín-Triviño et al., 2025).

Thus, the fertilising effect of CO_2 does not constitute a uniform response by forests to climate change, but depends heavily on interactions with water, nutritional and physiological constraints that determine trees' ability to convert this potential into actual growth (Xu et al., 2025).

1.2.2 Observed impacts on European forest productivity

The physiological mechanisms described above are now resulting in observable changes in the productivity of European forests. Numerous studies show that climate change is now altering forest growth across the continent, gradually reducing their capacity to continue increasing carbon sequestration. While rising temperatures and increased atmospheric CO_2 concentrations have contributed to increased growth in some regions, particularly Northern Europe, these positive effects are increasingly counterbalanced by droughts, disturbances and changing climatic variability (Lindner et al., 2010, 2014; Tijerín-Triviño et al., 2025). Based on more than 13,900 plots from the Spanish and Swedish national forest inventories, Tijerín-Triviño et al. (2025) show that the effect of temperature anomalies on forest productivity, initially positive in the Mediterranean and boreal regions, became increasingly negative over time across all four studied regions. This shift coincides with a significant decline in forest productivity in every region, ranging from −1.6% to −3.6%.

The impacts of climate change on forest productivity are not uniform across Europe, as the limiting factors vary greatly depending on climatic conditions and ecosystem characteristics. In Mediterranean regions, the increase in the frequency and intensity of droughts, combined with a higher risk of wildfires and mortality linked to water stress, is already leading to a decline in forest growth and biomass accumulation (Lindner et al., 2010). In contrast, Northern forests have historically benefited from favourable effects linked to warming, notably through a longer growing season and a potential increase in productivity. However, these gains are gradually being limited by the emergence of new constraints such as droughts, biotic disturbances and extreme events (Lindner et al., 2010). Thus, the effects of climate change result from a balance between favourable factors, such as rising temperatures in cold regions, and unfavourable factors, mainly linked to water shortages and climatic disturbances, whose

impacts are expected to increase in many European regions (Knutzen et al., 2025; Tijerín-Triviño et al., 2025).

The effects of climate change on forest productivity also vary significantly between species, depending on their physiological traits, their climatic requirements and their ability to adapt to new environmental conditions. Projections carried out at European level show that certain tree species adapted to cold climates, such as the Norway spruce (Picea abies) or the Scots pine (Pinus sylvestris), could maintain or even increase their productivity in certain Northern and central regions thanks to the lengthening of the growing season (Reyer et al., 2014). In contrast, species that are more sensitive to increased water stress, such as the common beech (Fagus sylvatica) or certain Mediterranean tree species, are expected to experience significant reductions in growth in regions where conditions are becoming warmer and drier (Reyer et al., 2014). This variability between species highlights the importance of considering the specific ecological characteristics of each tree species when assessing the future impacts of climate change.

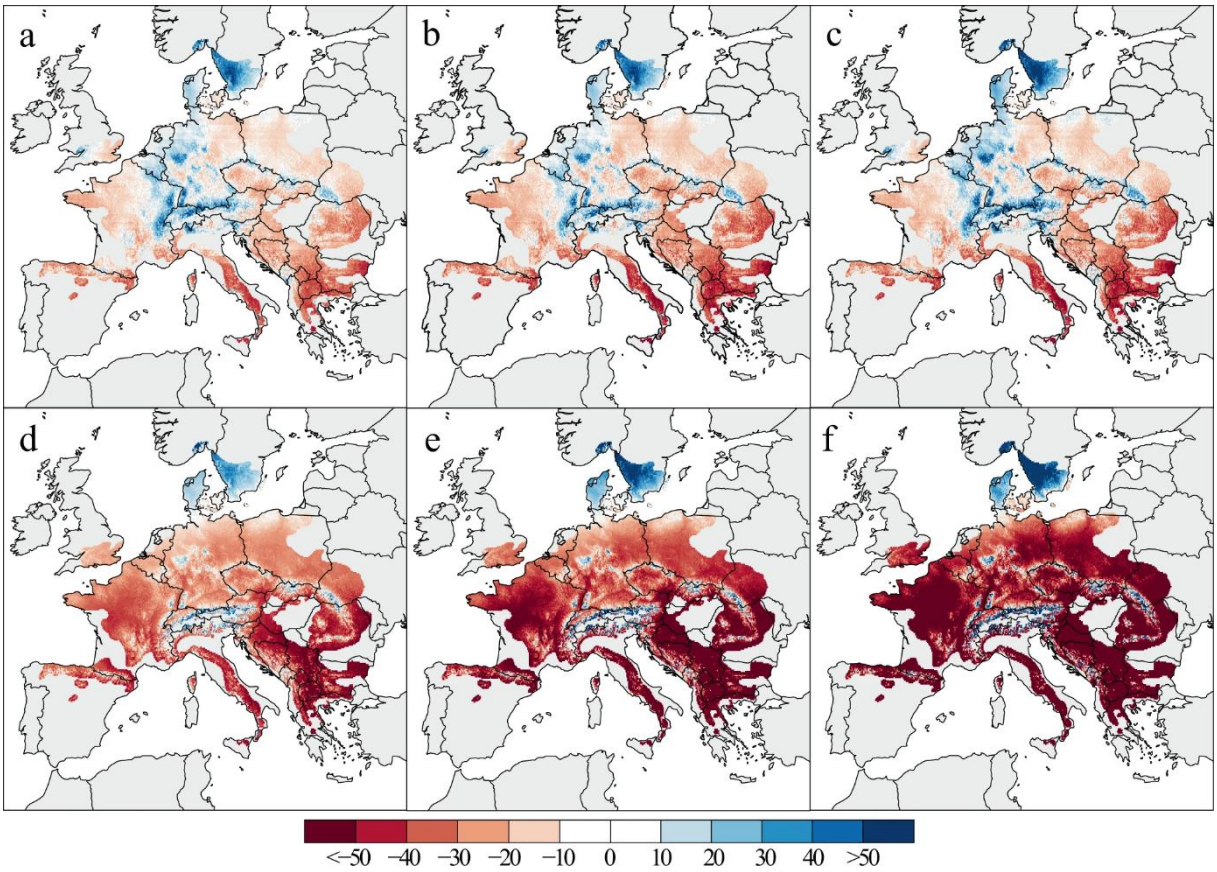

Figure 4. Projected relative changes in European beech (Fagus sylvatica) basal area increment (BAI, in %) compared to the 1986-2016 reference period, under SSP1-2.6 (a-c) and SSP5-8.5 (d-f) CMIP6 climate scenarios for three future periods: 2020-2050 (a, d), 2040-2070 (b, e), and 2060-2090 (c, f). Negative values (red) indicate growth decline. The most severe declines are projected towards the Southern distribution limit of the species under the high-emission scenario. From Martinez del Castillo et al. (2022).

Among these contrasting responses, European beech provides a particularly illustrative example of the vulnerability of certain temperate species to climate change. Based on 5,800 beech trees from 324 sites covering the entire geographical area of the species, Martinez del Castillo et al. (2022) document growth declines of Fagus sylvatica across large parts of its distribution area over the past decades. They further project severe productivity losses ranging from -20% to more than -50% by 2090 under the CMIP6

SSP1-2.6 and SSP5-8.5 scenarios, with the most pronounced declines occurring towards the Southern distribution limit of the range of the species, where persisting high-pressure systems are expected to increase drought severity. Figure 4 illustrates the spatial pattern and temporal progression of these projected declines.

1.2.3 Specific vulnerability of Walloon forests

Walloon forests are among the European forest ecosystems exposed to the effects of climate change. Located in the temperate oceanic zone, they have benefited for a long time from conditions favourable to growth, but the increasing frequency of droughts, heatwaves and biotic disturbances is gradually undermining this dynamic (Campioli et al., 2017). The extreme heat and drought events observed since 2018 have led to a marked decline in the vitality of forest stands, illustrating the growing sensitivity of Walloon forests to new climatic conditions (Knutzen et al., 2025). Climate projections further indicate that prolonged droughts substantially increase the probability of concurrent heat stress, reinforcing the vulnerability of Walloon forests to compound heat-drought events (Marchi et al., 2024).

The Norway spruce (Picea abies), which represented nearly a third of Wallonia's forest area, has suffered significant mortality as a result of successive droughts, storms and bark beetle infestations. These droughts have led to infestations on an unprecedented scale, resulting in massive sanitary felling and the need to regenerate vast areas of forest (Knutzen et al., 2025). These events illustrate the role of droughts as a trigger for major biotic disturbances, now regarded as one of the main threats to Wallonia's coniferous forests (Saintonge et al., 2021)

Deciduous stands are also affected, although their vulnerability varies greatly depending on the species. The beech (Fagus sylvatica), the dominant species in many Walloon beech forests, is recognised as being particularly sensitive to droughts. At a European level, a decline in its growth has already been observed across much of its range. As shown in the previous section, projections indicate that productivity losses could exceed 50 per cent by the end of the century in the most vulnerable regions (Martinez del Castillo et al., 2022). Conversely, the sessile oak (Quercus petraea), with which it frequently coexists, exhibits greater hydraulic resistance to water deficit (Aranda et al., 2005). This difference is particularly significant in Wallonia, where the beech's strong competitiveness under current conditions could become a disadvantage in a warmer and drier climate, reinforcing the case for silvicultural strategies that promote greater species diversification (André et al., 2025).

When faced with these vulnerabilities, quantifying the future effects of climate change on growth, water stress and the productivity of Walloon forests is a key challenge in guiding adaptation strategies. Mechanistic forest models provide a particularly effective framework for this analysis, as they allow the physiological responses of trees to future climatic conditions to be simulated explicitly.

1.3 Process-based forest modelling for climate impact assessment

1.3.1 The need for forest models in a context of climate changes

Forests are ecosystems with a long lifespan, and their responses to environmental changes can only be observed over several decades, or even several centuries. In this context, experimentation alone is not sufficient to anticipate the consequences of climate change or to evaluate potential adaptation strategies within a timeframe compatible with the needs of forest management. Modelling is therefore an indispensable tool for exploring these various possible trajectories, given the wide range of site

conditions, climate scenarios and management practices that cannot realistically be tested through field experiments alone (Jonard et al., 2020; Bosela et al., 2021).

By simulating the functioning and evolution of stands under different climatic and silvicultural scenarios, models make it possible to assess the potential consequences of various management strategies, identify the factors that control the response of forests to environmental changes, and inform management decisions despite the high levels of uncertainty associated with climate projections (Jonard et al., 2020; Bosela et al., 2021). Models are not intended to predict the future state of forests with precision, but rather to explore plausible scenarios and compare the relative effects of different management options in a constantly changing environment (Bugmann & Seidl, 2022).

1.3.2 The main approaches to modelling forest growth

Forest growth models differ in terms of their level of complexity and the ecological processes they integrate, going from simplified representations of forest dynamics to approaches explicitly based on ecophysiological processes (Bosela et al., 2022; Gilson et al., 2025). Empirical models are based on statistical relationships derived from observations of growth and explanatory variables such as age, stand density or site characteristics. Easy to parameterise and often highly effective under the environmental conditions for which they have been calibrated, they have long been widely used tools in forest management. However, their ability to predict stand dynamics in the context of climate change is limited, as they generally assume that relationships observed in the past will remain valid under different future conditions (Gilson et al., 2025; Jonard et al., 2020).

In contrast, process-based models aim to explicitly represent the ecophysiological processes that control tree growth, such as photosynthesis, respiration, carbon allocation and water exchange between the soil and vegetation. By simulating the mechanisms underlying growth rather than directly relating past observations to environmental conditions, these models enable to explore how forests respond to new climatic conditions and to complex interactions between different stress factors (Gilson et al., 2025; Jonard et al., 2020). They therefore constitute a particularly well-suited approach for studying the impacts of climate change, for which relationships established on the basis of historical observations may no longer remain valid under future environmental conditions. However, the explicit representation of ecological processes involves a higher level of complexity, requiring simplification choices in order to find a balance between biological realism and computational feasibility (Bugmann & Seidl, 2022).

The first process-based models of forest dynamics were primarily developed to represent pure, even-aged stands, simplifying the spatial structure of forests in order to limit the complexity of the calculations (Jonard et al., 2020). However, growing interest in mixed and uneven-aged stands has highlighted the need for approaches capable of representing a more complex forest structure. Beyond the distinction between empirical and process-based approaches, forest growth models can also be distinguished according to the spatial scale and level of detail at which they represent stand dynamics (Porté & Bartelink, 2002). Stand-scale models describe the forest as a relatively homogeneous entity, while cohort models allow the differentiation of groups of trees with similar characteristics, particularly in terms of age or size. Although these approaches provide a more detailed representation of forest structure, they remain limited in their ability to describe the spatial heterogeneity of complex stands. At a finer level of representation, individual tree-scale models allow the explicit simulation of the growth of each tree, as well as interactions between neighbouring individuals.

Among these various approaches, spatially explicit models at the individual-tree level appear particularly well suited for studying the dynamics of mixed and structurally complex stands, as they

enable the representation of local interactions between trees and competition for resources. This approach is relevant for Walloon forests, where adaptation strategies increasingly rely on species diversification and the transition from even-aged stands towards more heterogeneous structures (André et al., 2025). In this context, HETEROFOR was specifically developed to simulate these interactions at the individual-tree level.

1.4 Objectives

Walloon forests are facing an intensification of climatic stress whose future consequences on their productivity, water stress and vitality remain insufficiently quantified at the stand scale. Given this, the main objective of this Master thesis is to assess how climate change will affect forest productivity, water stress and defoliation in Walloon forests by 2100 using the HETEROFOR process-based model, and to identify the physiological mechanisms, species characteristics and site conditions governing these responses. Productivity, water stress and defoliation were selected because they jointly characterize forest functioning, tree vitality and the capacity of stands to cope with increasing climatic stress.

The study focuses on five Walloon plots distributed across three sites dominated by common beech (Fagus sylvatica) and sessile oak (Quercus petraea), two species with contrasting hydraulic strategies. The selected sites, which are situated at Baileux, Chimay and Louvain-la-Neuve, are considered to be representative of the pedo-climatic diversity of the Walloon forests. The simulations are primarily forced by observed IRM climate data over the historical period (1961-2024) and by climate projections from a global climate model (GFDL-ESM4) under the SSP3-7.0 scenario over the future period (2025-2100). An additional set of simulations using GFDL-ESM4 data over the historical period was also run to assess the extent to which biases in the climate model propagate to HETEROFOR outputs. Eight simulation configurations, described in the Methodology section, have been designed to assess the impact of climate change on forest indicators, and to isolate the additional contribution of atmospheric CO_2 fertilization on the one hand, and of hydraulic failure by xylem embolism on the other.

This work also pursues three complementary objectives. First, to evaluate the performance of the HETEROFOR model to simulate soil water dynamics and radial tree growth in Walloon conditions, in order to establish the reliability of future projections. Second, to examine to what extent explicitly accounting for CO_2 fertilization and hydraulic failure modifies the projected trajectories of productivity, water stress and defoliation, and assess whether these processes are necessary to accurately simulate forest responses to climate change. Third, to quantify the extent to which climate model biases propagate to HETEROFOR outputs, in order to contextualize the obtained results and their uncertainties. Overall, these objectives aim to provide a scientifically grounded basis for the development of adaptation strategies for Walloon forests in the context of ongoing climate change.

2. Material and methods

2.1. Study sites and stands

The study covers five forest plots spread across three sites in Wallonia (Figure 5). Two of these are in Baileux (beech and oak plots), two others are in Louvain-la-Neuve (beech and oak plots), and the fifth is in Chimay (oak plot). The three sites belong to distinct bioclimatic zones. Baileux (50.02°N, 4.40°E, ~300 m above sea level) receives an average of 1,075 mm of annual rainfall and has an average temperature of 9.8°C. Chimay (50.06°N, 4.27°E, ~260 m) receives 940 mm/year with an average temperature of 9.7°C. Louvain-la-Neuve (50.68°N, 4.60°E, ~130 m) is the driest and warmest site with 818 mm/year and 11.0°C.

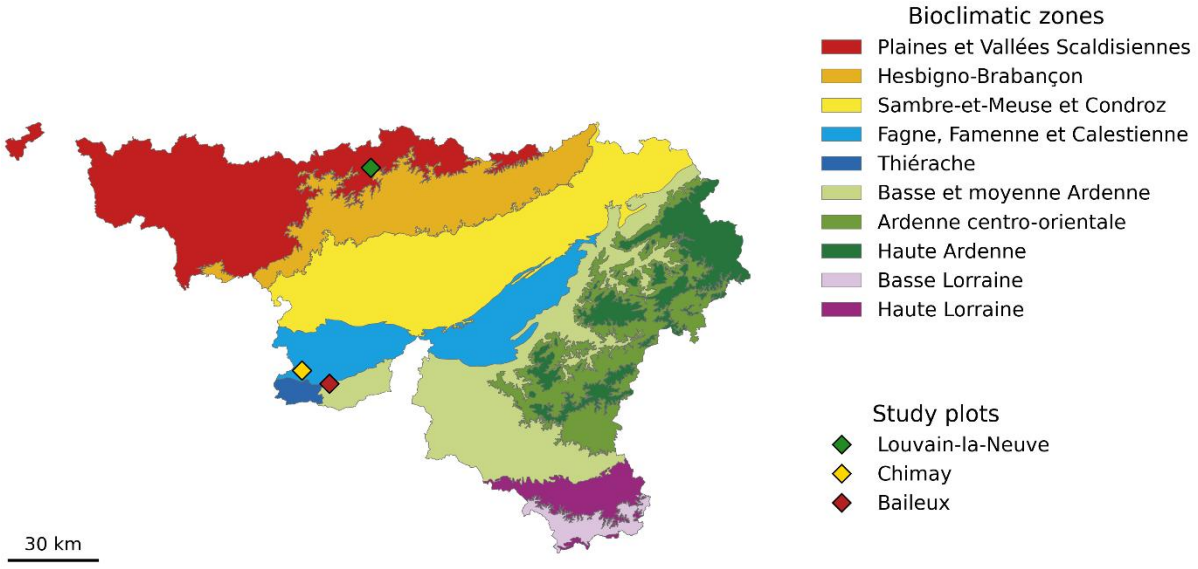

Figure 5. Location of the five study stands across three sites in Wallonia, Belgium, and their respective bioclimatic zones (Van der Perre et al., 2015)

Soil types also vary between sites. At Baileux and Chimay, the soil is a cambisol, whereas at Louvain-la-Neuve it is an abruptic luvisol characterised by a significantly higher extractable water reserve (450 mm compared with 178mm at Baileux and 205mm at Chimay). To isolate species effects from soil variability, the same soil profile was used for the two plots at each site. Thus, for Baileux and Louvain-la-Neuve, the soil from the beech forest was selected for both plots.

The stands differ markedly in their structure and management history. The Baileux stands originated from a major regeneration event around 1880. The sessile oak-dominated stand therefore presents the typical characteristics of an even-aged forest, whereas the beech-dominated stand has progressively developed towards a more uneven-aged structure with multiple diameter classes. In contrast, the Louvain-la-Neuve stands correspond to mature beech and oak-dominated forests with large trees and a more developed stand structure. The Chimay stand is an ancient coppice-with-standards dominated by mature sessile oak with a dense hornbeam understorey, resulting in a substantially higher stem density than the other stands. (Table 1) (de Wergifosse et al., 2020). Together, these sites include a broad range of climatic and edaphic conditions representative of Walloon temperate forests, making them suitable for assessing the influence of climate and site conditions on forest responses.

Table 1. Main stand characteristics at the start of the simulations (1961), based on field inventories conducted between 1999 and 2001. The same inventory file was used to initialise both the historical (1961-2024) and future (2025-2100) simulations.

Stand	**Total density (stems/ha)**	**Total basal area (m²/ha)**	**Species composition (% BA)**
Baileux beech	302	23.1	*Fagus* 73%, *Quercus* 27%
Baileux oak	480	22.1	*Quercus* 80.5%, *Fagus* 19.5%, *Carpinus* 6%
Chimay oak	717	19.5	*Quercus* 72.5%, *Carpinus* 27.3%
LLN beech	115	30.5	*Fagus* 84.8%, *Quercus* 15.2%
LLN oak	184	26.5	*Quercus* 89%, other species 11%

Each plot was initialised in HETEROFOR using a detailed inventory with, for each tree, the spatial position, circumference, total height, base height of the crown and crown radius in the four cardinal directions. It should be noted that the historical (1961-2024) and future (2025-2100) simulations are independent runs sharing the same initial inventory file. Since both simulation periods were initialised independently, from the same inventory, structural biomass was reset to identical initial conditions at the beginning of each simulation rather than being carried over from the historical to the future period. As a consequence, this design introduces discontinuities visible in certain time series at the transition point between the two periods, most notably in leaf area index dynamics.

2.2 HETEROFOR model

HETEROFOR is a spatially explicit forest growth model based on ecophysiological processes, developed within the CAPSIS (Computer-Aided Projection for Strategies in Silviculture) modelling platform (Jonard et al., 2020; de Wergifosse et al., 2020). Unlike models that treat a stand as a homogeneous entity, HETEROFOR represents each tree individually and simulates its growth based on its spatial position, structural characteristics and ability to access available resources (light, water and nutrients). This approach enables the representation of local interactions between trees and the effects of stand structure on forest dynamics, making the model particularly well-suited to mixed and uneven-aged stands.

The model operates through the interaction of several modules describing the main processes involved in tree growth and trees' response to environmental variations. The dimensional growth of trees is simulated at an annual time step, while some physiological processes, notably water exchange and photosynthesis, are calculated at a finer temporal resolution in order to represent the intra-annual variability of climatic conditions.

2.2.1 Modules

The water module simulates water flows between the atmosphere, vegetation and soil at the individual tree level. It models precipitation interception by the canopy, water infiltration into different soil layers,

root water uptake, individual transpiration and deep drainage. Water flows in the soil are calculated using Darcy's approach, which allows for the representation of water gradients between the different layers of the soil profile. Individual transpiration is estimated using the Penman-Monteith equation and depends, in particular, on stomatal conductance, which varies according to soil water availability, vapour pressure deficit and the specific characteristics of each tree. This module thus enables the onset and intensity of water stress to be modelled according to climatic conditions and stand properties (de Wergifosse et al., 2020).

The carbon module describes the processes governing carbon uptake and utilisation by trees. Photosynthesis is simulated using Farquhar's biochemical model, coupled with the approach developed by Ball et al. (1987) for stomatal regulation, via the CASTANEA library integrated into CAPSIS. The carbon fixed through photosynthesis corresponds to gross primary production (GPP). After accounting for losses due to respiration, net primary production (NPP) is calculated and then allocated amongst the tree's various compartments (leaves, fine roots, fruits and woody structures). This carbon allocation then determines the trees' dimensional growth (Jonard et al., 2020).

The phenological module simulates the main stages of the annual cycle of trees, including budburst, leaf development, leaf yellowing and leaf fall. The dates of these events are predicted for each species based on hourly weather conditions. The duration of the growing season directly influences the period during which photosynthesis and transpiration can take place. In HETEROFOR, defoliation is simulated when net carbon production becomes insufficient to sustain normal foliage development. Tree mortality is triggered when the defoliation level reaches 90 per cent (de Wergifosse et al., 2020).

The SamsaraLight module simulates radiative transfer within the forest canopy using a ray-tracing approach (André et al., 2021; Courbaud et al., 2003). Unlike simplified approaches that assume a homogeneous canopy, this module takes into account the spatial position and geometry of each tree's crown in order to estimate the amount of radiation intercepted by each individual tree. This representation makes it possible to simulate competition for light between neighbouring trees and its influence on individual growth.

Finally, by default, HETEROFOR simulates transpiration and photosynthesis in a fully reversible manner. Stomatal conductance decreases in the event of high evaporative demand or low soil water potential, but it recovers fully as soon as conditions become favourable again. This approach does not adequately represent the long-term effects of extreme events, such as heatwaves combined with droughts, on the tree's water balance. To overcome this limitation, an optional cavitation module has been implemented (André et al., 2025), based on the approach by Couvreur et al. (2018), which explicitly models hydraulic failure associated with xylem embolism. This module iteratively solves the vertical profile of water potential and xylem conductivity, based on a plausible transpiration flux and the water potential at the base of the trunk. The resulting loss of hydraulic conductivity, calculated at the tree top and at the base of the crown, is used to predict temporary defoliation and crown dieback, the latter affecting the level of defoliation in the following year. A recovery process is also incorporated: each year, the tree regains a part of its foliage proportional to its relative basal area growth. When the cavitation module is activated, total defoliation therefore results from the combination of competition-driven defoliation (described above) and hydraulic-driven defoliation. This module has been parameterised using values derived from the literature on stem hydraulic conductivity, xylem vulnerability (P50), the Huber ratio, and the relationship between loss of conductivity and defoliation and crown dieback (André et al., 2025).

2.2.2. Parametrization

The physical and hydraulic properties of the soil were provided in the form of soil horizons characterised by their texture, bulk density, stoniness, water content at field capacity and wilting point, pH, and proportion of fine roots. Hydraulic properties that had not been measured were estimated using the soil transfer functions developed by Weynants et al. (2009).

The physiological parameters for the species come from two files: the HETEROFOR parameter file (allometric relationships, height and diameter growth parameters, xylem hydraulic conductance) and the CASTANEA parameter file (biochemical parameters relating to photosynthesis, respiration and phenology). These parameters are those calibrated for the European beech (Fagus sylvatica) and the sessile oak (Quercus petraea) in the original studies by Jonard et al. (2020) and de Wergifosse et al. (2020), without further calibration.

Silvicultural interventions were applied in the same way across all plots and scenarios, in order to isolate the effect of climate from that of management. Thinning was carried out every 12 years with a maximum intensity of 25% of the basal area, following species-specific silvicultural guidelines: Vannière's production tables (1984) for beech, and Sardin's recommendations (2008) for sessile oak. This choice constitutes a simplification compared to actual forest management, which would likely be adapted in response to the projected changes. Its implications as a limitation of the study are discussed in Section 4.6.

2.3. Climate data

The historical simulations (1961-2024) were forced with interpolated daily climate data from the Royal Meteorological Institute of Belgium (IRM), downloaded from the opendata.meteo.be platform. Using observational data for the historical period ensures that the simulated forest dynamics are driven by the most realistic possible representation of actual climate conditions. Each site was assigned to its representative IRM pixel based on Wallonia's bioclimatic zone map (Walonmap) with pixel 196 (Winenne, 50.097°N, 4.869°E) for Baileux, pixel 150 (Daverdisse, 50.007°N, 5.078°E) for Chimay, and pixel 545 (Jurbise, 50.545°N, 3.881°E) for LLN. Wind data were sourced from the IRM synoptic network, with different reference stations depending on the site.

The future simulations (2025-2100) were produced using daily output from the GFDL-ESM4 global climate model, part of the ISIMIP (Inter-Sectoral Impact Model Intercomparison Project), under the SSP3-7.0 emissions scenario. The SSP3-7.0 scenario was selected as it represents an intermediate-to-high forcing pathway consistent with current global emission trajectories (IPCC, 2021), corresponding to a projected warming of approximately 3.6°C in Belgium by 2100 relative to the 1976-2014 reference period (André et al., 2025). The GFDL-ESM4 data cover the period 1850-2100, combining the model's own CMIP6 historical experiment (up to 2014) with the SSP3-7.0 scenario run (from 2015 onward) into a single continuous series. These data were bias-corrected according to the ISIMIP3 protocol (Lange, 2019), which applies a trend-preserving parametric quantile mapping, calibrated over the period 1976-2014 using gridded IRM observations at a resolution of 5 km. This correction adjusts biases across the entire distribution of the variables and not just the mean, while preserving long-term trends in each quantile. It was applied independently for each variable, each site and each month. The corrected variables are air temperature, minimum temperature, precipitation, relative humidity, solar radiation and wind speed. Although the ISIMIP3 correction adjusts the statistical distribution of climate variables, it does not alter the temporal dynamics of the warming simulated by the model. In particular, it cannot correct for a potential underestimation of the rate of recent warming by GFDL-ESM4.

To assess the magnitude of this bias propagation, a set of historical simulations was run using GFDL-ESM4 data over the 1961-2024 period and compared with the results obtained from IRM forcing (Section 3.4).

As HETEROFOR operates on an hourly time step, both IRM and GFDL-ESM4 daily data were disaggregated into hourly data using empirical coefficients calibrated as part of the REGE+ project (André et al., 2025), based on hourly reference climate time series from the IRM's automatic stations. The disaggregation covers radiation (monthly hour-by-hour coefficients), precipitation (seasonal hourly distribution), temperature (cosine formula), wind speed (separate day/night formulas) and relative humidity (via dew point temperature).

Two CO_2 scenarios were used. In the reference scenario, used for the vast majority of analyses, the CO_2 concentration is held constant at 317.8 ppm, a value corresponding to the concentration in 1961 according to the SSP3-7.0 trajectory (Meinshausen et al., 2020). This choice allows the effect of climate change alone to be isolated, without the fertilising effect of CO_2. A second scenario uses the variable trajectory of SSP3-7.0, where the concentration rises from around 318 ppm in 1961 to around 872 ppm in 2100, used only to quantify the carbon fertilisation effect

Table 2. Overview of all datasets used in this study, including their source, temporal coverage, resolution and purpose. Daily climate data were disaggregated to hourly resolution using empirical coefficients calibrated as part of the REGE+ project (André et al., 2025).

Data type	Source	Period	Resolution	Use in this study
Historical climate	IRM gridded data (opendata.meteo.be)	1961-2024	Daily to hourly	Historical simulations (all scenarios)
Future climate	GFDL-ESM4 / ISIMIP (SSP3-7.0)	2025-2100	Daily to hourly	Future simulations (all scenarios)
Additional historical climate	GFDL-ESM4 / ISIMIP (SSP3-7.0)	1961-2024	Daily to hourly	Climate model bias assessment (Section 3.4)
Atmospheric CO_2	SSP3-7.0 (Meinshausen et al., 2020)	1961-2100	Annual	Variable CO_2 scenarios
Forest inventory	Field measurements	1999-2001	Plot-level	HETEROFOR initialisation
Soil data	Field measurements	1999 - 2001	Horizon-level	HETEROFOR initialisation
Soil water content	TDR measurements	2006-2020	Hourly	Model evaluation
Circumference increment	Dendrometric surveys	2001-2019	Annual	Model evaluation

2.4. Simulation design

Eight simulation designs were designed to disentangle the effects of climate change, CO_2 fertilisation and hydraulic failure on forest indicators (Table 3).

Table 3. Overview of the eight simulation designs used in this study.

Experiment name	Period	CO_2	Cavitation module	Purpose
Historical CO_2cst	1961-2024	Constant (317.8 ppm)	No	Reference historical
Historical CO_2var	1961-2024	Variable (SSP3-7.0)	No	CO_2 fertilisation effect
Future CO_2cst	2025-2100	Constant (317.8 ppm)	No	Main scenario - climate change effect
Future CO_2var	2025-2100	Variable (SSP3-7.0)	No	CO_2 fertilisation effect
Historical CO_2cst + cavit	1961-2024	Constant (317.8 ppm)	Yes	Cavitation effect
Historical CO_2cst no cavit	1961-2024	Constant (317.8 ppm)	No	Cavitation reference
Future CO_2cst + cavit	2025-2100	Constant (317.8 ppm)	Yes	Cavitation effect
Future CO_2cst no cavit	2025-2100	Constant (317.8 ppm)	No	Cavitation reference

A first group of four experiments combines two time periods (historical 1961-2024 and future 2025-2100) with two CO_2 trajectories (constant at 317.8 ppm and variable according to SSP3-7.0), without a cavitation module. These experiments enable the quantification of the carbon fertilisation effect by comparing, over the same time period, the results obtained with constant CO_2 and variable CO_2.

A second set of four experiments, all assuming a constant CO_2 level (317.8 ppm), compares simulations with and without a cavitation module for both periods. These simulation designs enable an assessment of the extent to which explicitly accounting for hydraulic embolism alters projections of water stress, defoliation and productivity.

For the remainder of the analysis, only the experiment with constant CO_2 levels and no cavitation module is used as the main reference. This choice is justified by the fact that no single configuration consistently outperforms the other across all sites and indicators (see Section 2.5), and that the cavitation module was only recently added to the model, compared to the other modules that form its core.

For each simulation, the following indicators were extracted annually at the plot scale: net primary productivity (NPP, in $gC/m^2/year$), water stress (number of days per year with a REW below 0.32), defoliation (%), standing volume (m^3/ha) and basal area (m^2/ha). The critical REW thresholds reported in the literature vary according to species and measurement method. Granier et al. (1999) report values going from 0.3 to 0.4 , while Paligi et al. (2025) report values of up to 0.6 under different experimental conditions. The threshold of 0.32 adopted here was calculated proportionally to the reported value of 0.4 (Granier et al., 1999), scaled down to account for the fact that simulated REW values in this study

rarely exceeded 0.8 (0.4 × 0.8 = 0.32). This value thus falls at the lower end of the range reported in the literature.

Beyond the threshold itself, there is no consensus on the universal superiority of any single type of water stress indicator. Indices that account for atmospheric evaporative demand generally perform better than those based only on precipitation (Speich, 2019), but comparisons between indices carried out in different studies show considerable divergence, without it being possible to identify a single indicator that is consistently superior (Speich, 2019). In order to contextualise the choice of REW as the indicator, an assessment of its robustness is presented in section 3.1.2. It consists of a comparison with an alternative indicator based on relative transpiration deficit, which inherently reflects both soil water availability and atmospheric demand, and a validation against field observations.

2.5. Model evaluation

The evaluation of HETEROFOR was carried out with and without the cavitation module for the Chimay and Baileux sites. It focuses on two types of variables: soil water dynamics, assessed using relative extractable water (REW) measured by TDR (2006-2017 in Baileux, 2015-2020 in Chimay), and tree growth, assessed via increment in circumference (2001 and 2019 in Baileux, 1999 and 2014 in Chimay). Performance was quantified using Pearson's correlation coefficient (r), the bias and the RMSE.

It should be noted that the evaluation of tree growth is based on only two measurement dates per site, which limits the statistical robustness of the performance assessment. This limitation is discussed in Section 4.6.

2.6. Statistical analyses

Before carrying out any statistical comparisons, the normality of the distributions of each indicator was checked visually using quantile-quantile plots (QQ-plots) for each indicator and each configuration. The distributions were judged to be sufficiently close to normal to justify the use of parametric tests, with the exception of certain defoliation and water stress scenarios which showed more pronounced deviations.

The temporal independence of the residuals was verified visually by examining the autocorrelation functions (ACF) at lags of 1 to 5 years. The results show weak autocorrelation for NPP, water stress and defoliation (coefficients below 0.2 for most configurations), and more pronounced autocorrelation for basal area (coefficients between 0.35 and 0.53), which is to be expected for a structural variable that changes slowly. Comparison tests were nevertheless applied to all indicators, but the results concerning basal area should be interpreted with caution.

Comparisons between configurations were carried out using Tukey's HSD (Honestly Significant Difference) test, with a significance threshold set at $p < 0.05$. The statistical unit is the annual average value per plot, yielding approximately 320 values per historical experiment (5 plots × 64 years) and 380 values per future experiment (5 plots × 76 years).

The relationships between continuous variables, such as those between water stress and NPP, between summer temperature and NPP, and between climatic variables and forest indicators, were quantified using Spearman's correlation coefficient (ρ). This non-parametric coefficient was preferred to Pearson's correlation coefficient due to the presence of extreme values, for which it is more suitable.

To see whether the annual bias between GFDL-ESM4 simulations and IRM observations exhibits a temporal trend, a Mann-Kendall test was applied to the annual bias time series for each site. This non-parametric method has been widely used for detecting trends in hydrometeorological time series, including temperature and precipitation, and does not require assumptions about the distribution of the data (Wang et al., 2020). The test statistic tau ranges from -1 to +1, where negative values indicate a decreasing trend. The associated Sen slope, defined as the median of all pairwise slopes between data points, provides a robust estimate of the rate of change that is insensitive to outliers.

To test the water stress indicator against field observations, the agreement between the observed and simulated classification of each day as a stress day was calculated using Cohen's kappa (Landis & Koch 1977), a statistic that measures agreement beyond that expected by chance alone.

To disentangle the combined and interacting effects of temperature and water stress on NPP, a multiple linear regression model (NPP ~ Temperature + Stress + Temperature×Stress) was fitted separately for each species and period, using standardised (centred and scaled) predictors to allow comparison of coefficients.

In addition to the Mann-Kendall and Sen slope analysis applied to the entire time series, three other approaches were used to investigate the propagation of climate trend biases in HETEROFOR simulations: simple linear regression fitted in consecutive 20-year blocks to identify divergences concentrated in a sub-period rather than visible in the overall trend, and a sensitivity ratio, calculated as ratio of slopes between each indicator and summer temperature, to test whether the indicator's response to warming is proportional to the rate of warming of the forcing used. To verify the robustness of the trends obtained from the Sen slope, a supplementary method of regression on decadal averages was also used.

All statistical analyses and visualisations were carried out in Python, using the scipy, statsmodels, pandas, matplotlib and seaborn libraries.

3. Results

The results are organized into four sections. The first section (3.1) outlines forest responses to climate change and evaluates the model's performance, in order to provide the necessary context for the analyses that follow. The second section (3.2) examines the mechanisms that explain why forests respond differently depending on the site, species and time period, by analysing the relationships between climate variables, tree, water stress and productivity. The third section (3.3) focuses on the evolution of climate extremes and their impacts on forest productivity, complementing the analysis of average trends conducted in 3.2. Finally, the fourth section (3.4) addresses the question: to what extent does the underestimation of European warming by climate models, discussed in the introduction, results in biases in HETEROFOR's forest projections?

3.1 General responses to climate change

3.1.1 Model evaluation

A model evaluation was carried out with and without the cavitation module for the Chimay site and the two plots in Baileux. This evaluation focuses on the soil's hydraulic properties as well as tree growth, measured by increment in circumference. The measurements used for soil water properties cover the period 2006-2017 for Baileux and 2015-2020 for Chimay. For circumferential growth, the assessment covers the period 2001-2019 in Baileux and 1999-2014 in Chimay.

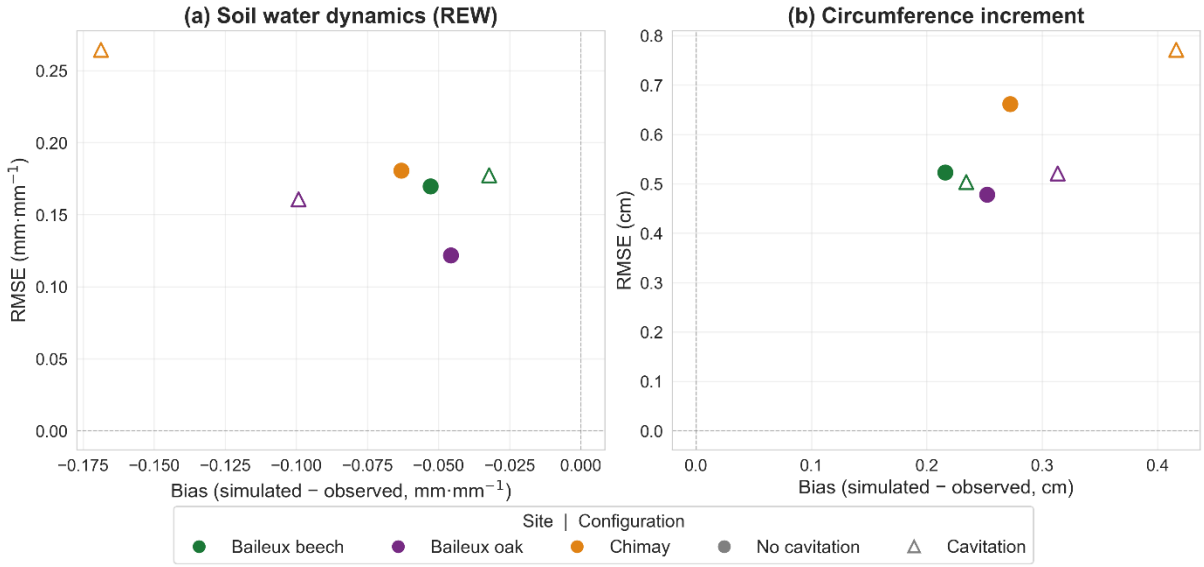

Figure 6. HETEROFOR model evaluation for (a) soil water dynamics (relative extractable water, REW) and (b) circumference increment. Each point represents one site × configuration combination (filled circles = no cavitation module, open triangles = cavitation module). Colours indicate the site (green = Baileux beech, purple = Baileux oak, orange = Chimay). The x-axis shows the mean bias (simulated − observed) and the y-axis the root mean square error (RMSE). Points closer to the origin indicate better model performance. Detailed metrics by horizon and species are provided in Appendix A .

For soil water dynamics, assessed using the relative extractable water (REW), the model performs well at all sites (Figure 6). A systematic negative bias is observed, indicating that the model underestimates REW in all configurations. This bias is more pronounced at Chimay (-0.06 to -0.17) than at Baileux (-0.03 to -0.10), and the root mean square error (RMSE) is also higher there (0.18-0.26 versus 0.12-0.18). Pearson correlations confirm that the model captures the temporal dynamics of REW well despite this systematic bias (r = 0.85-0.92, see Appendix A, table A1).

The effect of the cavitation module varies between sites: it significantly improves performance for the oak plot at Baileux, sharply reducing the bias in soil horizons from +0.10-0.16 to values close to zero while also decreasing the overall RMSE (see Appendix A, Figure A1 : REW time series). In contrast, its effect is limited or slightly negative for the beech stand at Baileux and for Chimay.

Regarding the increase in circumference, the model systematically overestimates growth, with a positive bias at all sites and for all species, with the exception of oak in the beech stand at Baileux, where a slight negative bias is observed. Performance is better at Baileux (RMSE of 0.52-0.53) than at Chimay (RMSE of 0.6-0.76). The effect of activating the cavitation module is weak and not very systematic for growth. A slight improvement is observed at Baileux beech, but no clear trend emerges across all sites. The poorer results from Chimay will be discussed in Section 4 in light of the specific characteristics of this stand.

Overall, HETEROFOR satisfactorily reproduces soil water dynamics at all sites, with the cavitation module providing an improvement for the Baileux oak forest. Performance in terms of growth is more variable, and the cavitation module does not consistently improve the results. However, no single configuration consistently outperforms the other across all sites and indicators. For the following analyses (from section 3.2 onwards), the configuration without cavitation is used as the main reference. This choice is justified by the fact that the cavitation module has been developed recently, making it subject to further development. All analyses have nevertheless been reproduced with the cavitation module activated, and instances where the two configurations produce significantly different results are noted in the text (corresponding figures are presented in Appendix B).

3.1.2 Water stress indicator robustness

The water stress indicator used throughout this study (the number of days per year with an REW below 0.32) was assessed in more detail, by comparing it with an alternative indicator and with field observations, in order to evaluate its robustness for comparisons between sites and scenarios.

The observed and simulated REW was compared on a daily basis at Baileux (beech and oak) and at Chimay, the only sites where soil moisture was monitored. Only the non-cavitation configuration was used, consistent with the reference configuration used throughout this study. For each day on which observed values were available during the growing season, the classification of the day as a stress day (REW < 0.32) was compared using Cohen's kappa (Landis & Koch, 1977), a statistic that quantifies the agreement between two classifications beyond what would be expected by chance alone, and is therefore more informative than raw accuracy when one class (here, stress days) is less frequent than the other. Agreement was strong at Baileux beech ($\kappa = 0.701$) and at Chimay ($\kappa = 0.690$), and moderate at Baileux oak ($\kappa = 0.591$). The direction of the disagreement varied by site (Table 4). The model underestimated the number of stress days at Baileux oak (sensitivity = 0.753, specificity = 0.902), while it overestimated them at Chimay (sensitivity = 0.945, specificity = 0.759). A complementary comparison of annual stress day counts, rather than daily classification, showed a consistent bias in the same direction, with simulated values exceeding observed ones by an average of 3.0 days at Baileux beech, 7.5 days at Baileux oak, and 19.0 days at Chimay. This annual comparison was significantly correlated with observed values at Baileux ($\rho = 0.907$ for beech and 0.678 for oak), but not at Chimay ($\rho = 0.657$, $p = 0.156$), where the small number of complete years available ($n = 6$) limits the conclusiveness of this specific test.

Table 4. Daily agreement between observed (TDR) and simulated relative extractable water (REW) in classifying growing-season days as water stress days (REW < 0.32), at Baileux (beech, oak) and Chimay, under the reference configuration without cavitation. Sensitivity and specificity indicate, respectively, the proportion of observed stress days correctly identified by the model and the proportion of observed non-stress days correctly identified. Cohen's kappa quantifies the agreement between the two classifications beyond what would be expected by chance alone (Landis & Koch, 1977).

Site	n (days)	Accuracy	Sensitivity	Specificity	κ (kappa)
Baileux beech	2123	0.858	0.846	0.865	0.701
Baileux oak	2095	0.878	0.753	0.902	0.591
Chimay	1072	0.843	0.945	0.759	0.690

The water stress indicator was also compared with an indicator of relative transpiration deficit (the ratio of transpiration deficit to potential transpiration, calculated from annual fluxes), under the same reference scenario. At plot level, the two indicators are strongly to moderately correlated (Spearman's ρ = 0.899 at Baileux beech, 0.830 at Baileux oak, 0.896 at Chimay, 0.588 at LLN beech and 0.600 at LLN oak). The agreement is thus consistently stronger at Baileux and Chimay than at LLN (Figure 7), a contrast examined in more detail in Section 4. Although calculated here on an annual scale, this indicator yields equally consistent results when calculated on a daily scale (ρ = 0.979 between the two approaches). This indicator captures the combined effect of soil water availability and atmospheric demand on tree transpiration, since stomatal conductance in HETEROFOR is modelled as a function of both soil water potential and vapour pressure deficit (de Wergifosse et al., 2020).

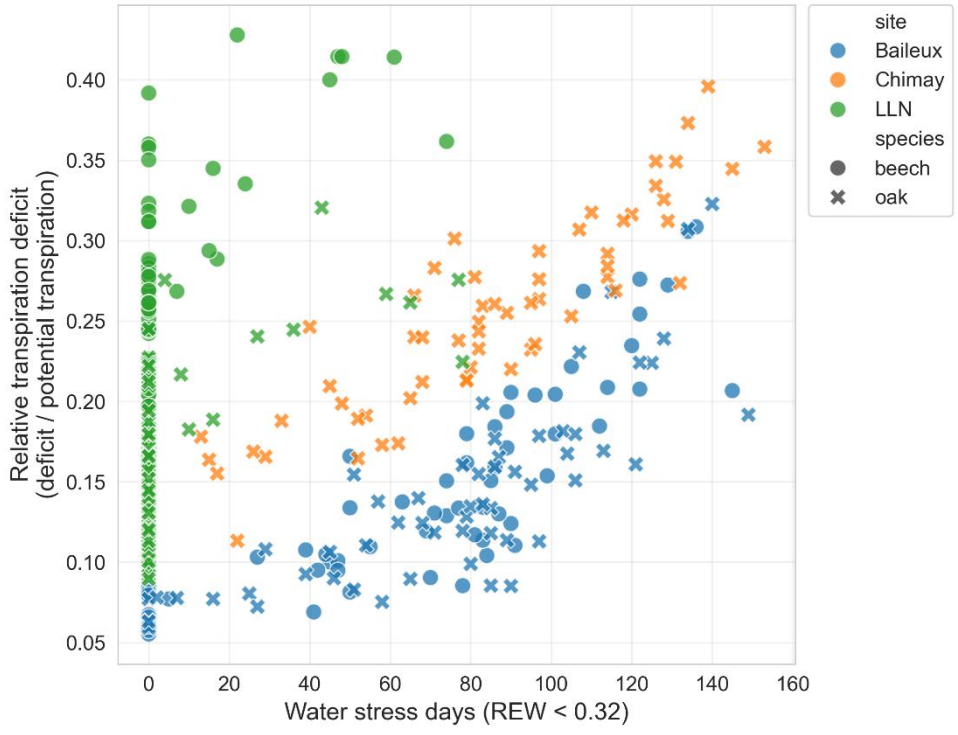

Figure 7. Relationship between water stress, expressed as the number of days per year with REW below 0.32, and the relative transpiration deficit (ratio of transpiration deficit to potential transpiration), for all plot-years under the constant-CO_2 scenarios. Colour indicates site (Baileux, Chimay, LLN); marker shape indicates species (circle = beech, cross = oak).

3.1.3 Effect of atmospheric CO_2 concentration

HETEROFOR simulations reveal contrasting responses to climate change depending on the indicator considered. Water stress and net primary productivity show the strongest responses, while structural indicators such as stand volume and basal area evolve more slowly (Figure 8).

Using a constant value for atmospheric CO_2 concentration (that of 1961, 318 ppm), net primary productivity (NPP) increases between the historical (1961-2024) and future (2025-2100) periods, with median annual values rising from 662 to 708 gC/m²/year across all stands. This difference is statistically significant. When the CO_2 concentration follows the SSP3-7.0 trajectory, future NPP reaches a median of 966 gC/m²/year, representing a 42% increase compared to the historical period under the variable CO_2 concentration. For each stand, the differences between the results obtained for the future period with variable CO_2 are significant compared with all other scenarios. In contrast, the differences between the two scenarios for the historical period are not significant, suggesting that the CO_2 fertilisation effect only becomes apparent in the future period.

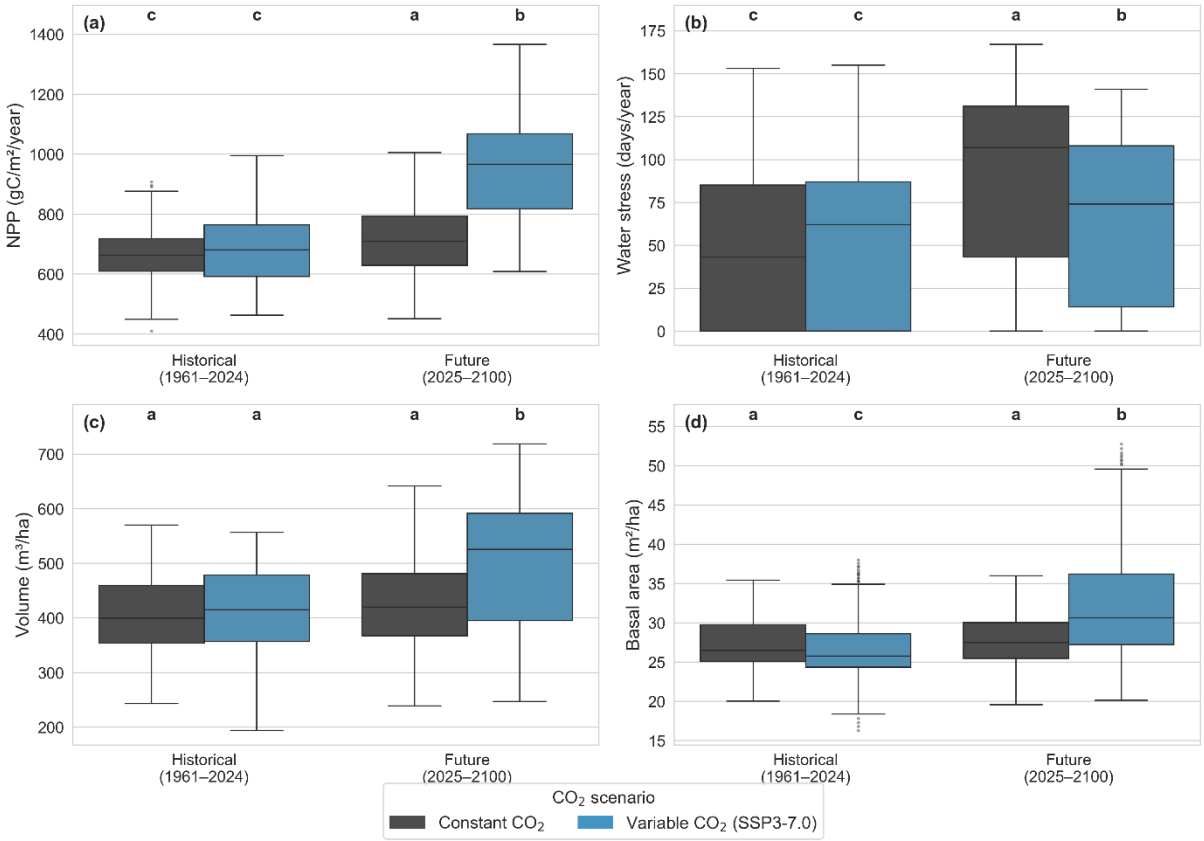

Figure 8. Distributions of NPP (a), water stress (b), stand volume (c) and basal area (d) under two CO_2 scenarios across all stands, in historical and future period. Box limits represent the 25th and 75th percentiles (interquartile range), the horizontal line indicates the median, whiskers extend to 1.5× the interquartile range, and points beyond whiskers are individual outliers. Different letters above boxplots indicate significant differences between scenarios (Tukey HSD, $p < 0.05$). Without the cavitation module.

The median volume remains relatively stable between the historical and future periods at constant CO_2 levels (rising from 399 to 420 m³/ha overall), the comparisons between these two scenarios is statistically significant. A similar pattern was observed for basal area, with median values of 27.3 m²/ha in the historical period and 27.9 m²/ha in the future period under constant CO_2. In contrast, the future scenario with variable CO_2 shows an increase in volume of 110 m³/ha (rising from 415 to 525 m³/ha)

compared to the historical period with variable CO_2 (an increase of 26.5%). However, these differences are not significant, reflecting the high inter-stand variability.

The number of water stress days increases significantly between the historical period and the future period under constant CO_2 conditions, with the median rising from 43 to 107 days of stress per year. Under variable CO_2 conditions, although the difference between the historical and future periods remains significant, it is smaller (from 43 to 74 days per year). The future scenario with variable CO_2 shows a lower median stress than the future scenario with constant CO_2 (74 vs 107 days per year), and this difference is statistically significant. This result suggests a possible effect of rising CO_2 on water use efficiency, which will be analysed in more detail in the discussion section.

Overall median defoliation shows significant differences between most scenario pairs, with two notable exceptions (Figure 9). No significant difference is observed between the two constant CO_2 scenarios (historical and future), or between the two variable CO_2 scenarios (historical and future). In particular, the future variable CO_2 scenario differs significantly from the historical constant CO_2 scenario, but not from the historical variable CO_2 scenario. Median values range from 2.6% (variable future CO_2) to 4.4% (constant historical CO_2). These patterns are difficult to interpret in isolation, as these simulations were carried out without the HETEROFOR cavitation module: in this configuration, defoliation is primarily determined by intra-stand competition dynamics rather than water stress. The results with the cavitation module will be presented in the following section.

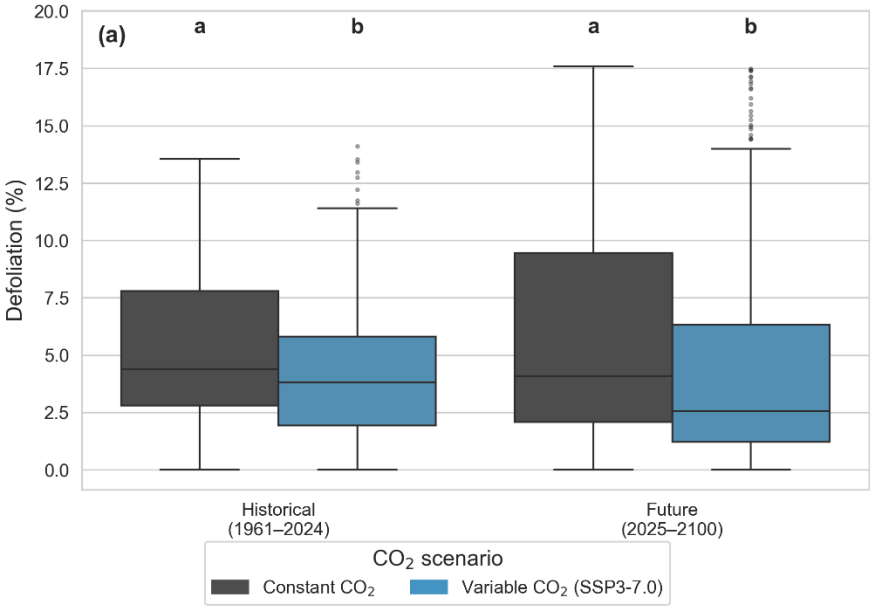

Figure 9. Defoliation distributions under the two CO_2 scenarios (constant and variable) across all stands, without the cavitation module.

3.1.4 Effect of the cavitation module

Enabling the cavitation module in HETEROFOR considerably alters certain results, particularly those relating to defoliation and water stress. Structural indicators (volume and basal area) remain largely unaffected, whereas productivity shows significant differences across the various scenarios.

Taking cavitation into account has little effect on the trends in volume and basal area, regardless of the period considered. The overall medians remain of the same order of magnitude even in the future, going

from 420 to 454 m³/ha for volume and from 27.4 to 29.4 m²/ha for basal area. On the other hand, the NPP differs significantly between all scenarios involving cavitation and those without cavitation, except for the comparison between the two historical scenarios (Figure 10). Overall, cavitation increases the median NPP from 662 to 677 gC/m²/year in the historical period, and from 708 to 768 gC/m²/year in the future period. Variability is also increased with cavitation, more especially for the future period.

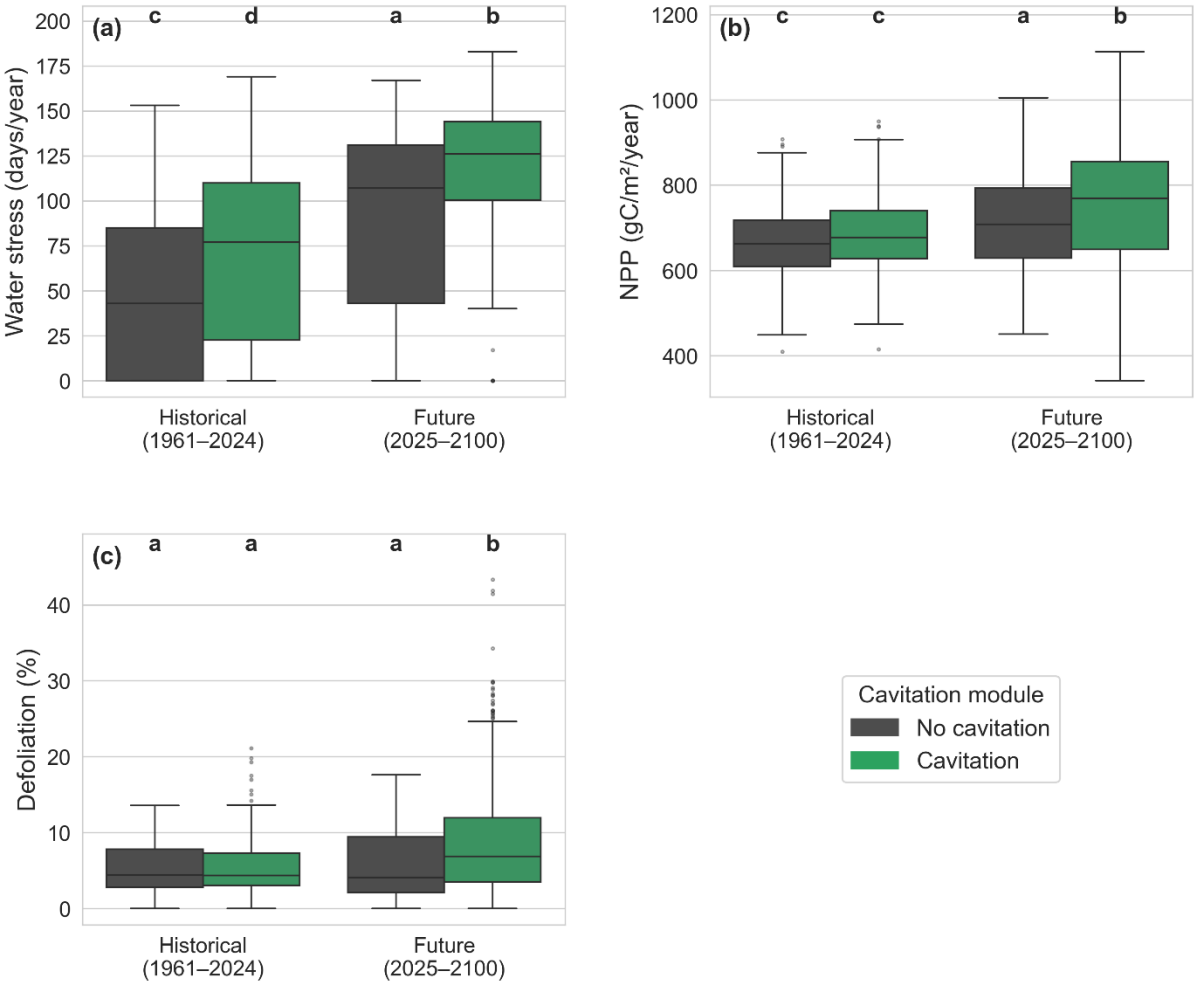

Figure 10. Effect of the cavitation module on water stress (a), NPP (b) and defoliation (c) across all stands. Scenarios with and without the cavitation module use a constant CO_2 concentration (317.8 ppm).

The cavitation module significantly increases water stress in both periods. The overall median rises from 43 to 77 days per year in the historical period (+79%) and from 107 to 126 days per year (+18%) for the future period. The effect is particularly pronounced for the stands in Louvain-la-Neuve, where there were no days of stress during the historical period but which reached 28 to 44 days per year with the cavitation module.

Overall, median defoliation rises from 4.1% (without cavitation) to 6.9% (with cavitation), but there are significant contrasts between sites and species. At the global level, only the future scenario with cavitation activated differs significantly from the other three configurations which do not differ significantly from one another. At the stand level, the contrasts are much clearer. The beech stand at Baileux shows a median defoliation for the future period rising from 1.7% to 9.5% (with cavitation), while Louvain-la-Neuve rises from 2.7% to 7.9% for the historical period. Conversely, Chimay sees its

defoliation decrease from 9.8% to 3.3% in the historical period, which is a counter-intuitive result. An analysis of the defoliation components reveals that this decrease is entirely attributable to a reduction in competition-driven defoliation (from 8.25% to 2.37%), while cavitation-driven defoliation remains zero at this site (Appendix C). This will be explored in the Discussion section. These results suggest that the effect of the cavitation module on defoliation is strongly regulated by local conditions and species traits.

Although median defoliation values remain relatively close between configurations, the cavitation module generates markedly higher extreme values, suggesting that its main effect on defoliation is to produce severe but episodic defoliation events rather than a systematic increase across all years. This can be visualised with Figure 11, that shows the cumulative defoliation distributions for the four scenarios. The distributions are similar for the two historical scenarios and the future scenario without cavitation, with 90th percentiles ranging from 9% to 14%. The future scenario with cavitation stands out clearly, with a 90th percentile of 18% and a distribution tail extending up to 43%.

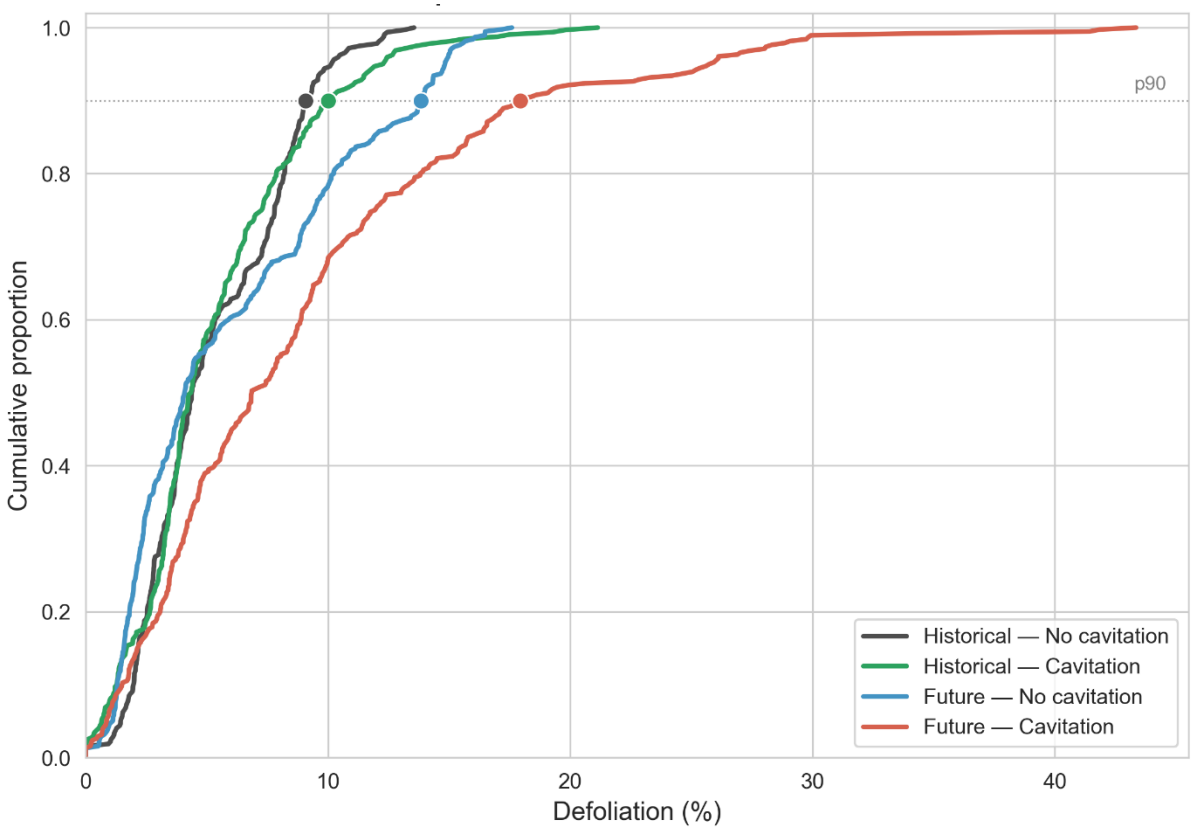

Figure 11. Empirical cumulative distribution functions (ECDF) of defoliation across all plots and years, for four scenarios combining period (historical 1961-2024 vs future 2025-2100) and cavitation module (enabled vs disabled), under constant CO_2 conditions. Filled circles indicate the 90th percentile of each distribution.

3.2 Mechanisms and drivers of forest responses to climate change

3.2.1 Site and species effects on water stress and NPP

The simulations reveal marked and significant differences in water stress between sites, mainly associated with differences in local soil characteristics. During the historical period under constant CO_2 levels, the median water stress for the beeches at Baileux reached 78 days per year, compared with just 0 days per year at LLN. This near-absence of stress at LLN is consistent with its higher soil extractable

water capacity, which is twice that of Baileux (450 mm for the abruptic luvisol at LLN compared with 178mm for the cambisol at Baileux). For oaks, Baileux and Chimay show similar historical stress levels (~80 days/year), while LLN remains, here too, very low in stress (Figure 12).

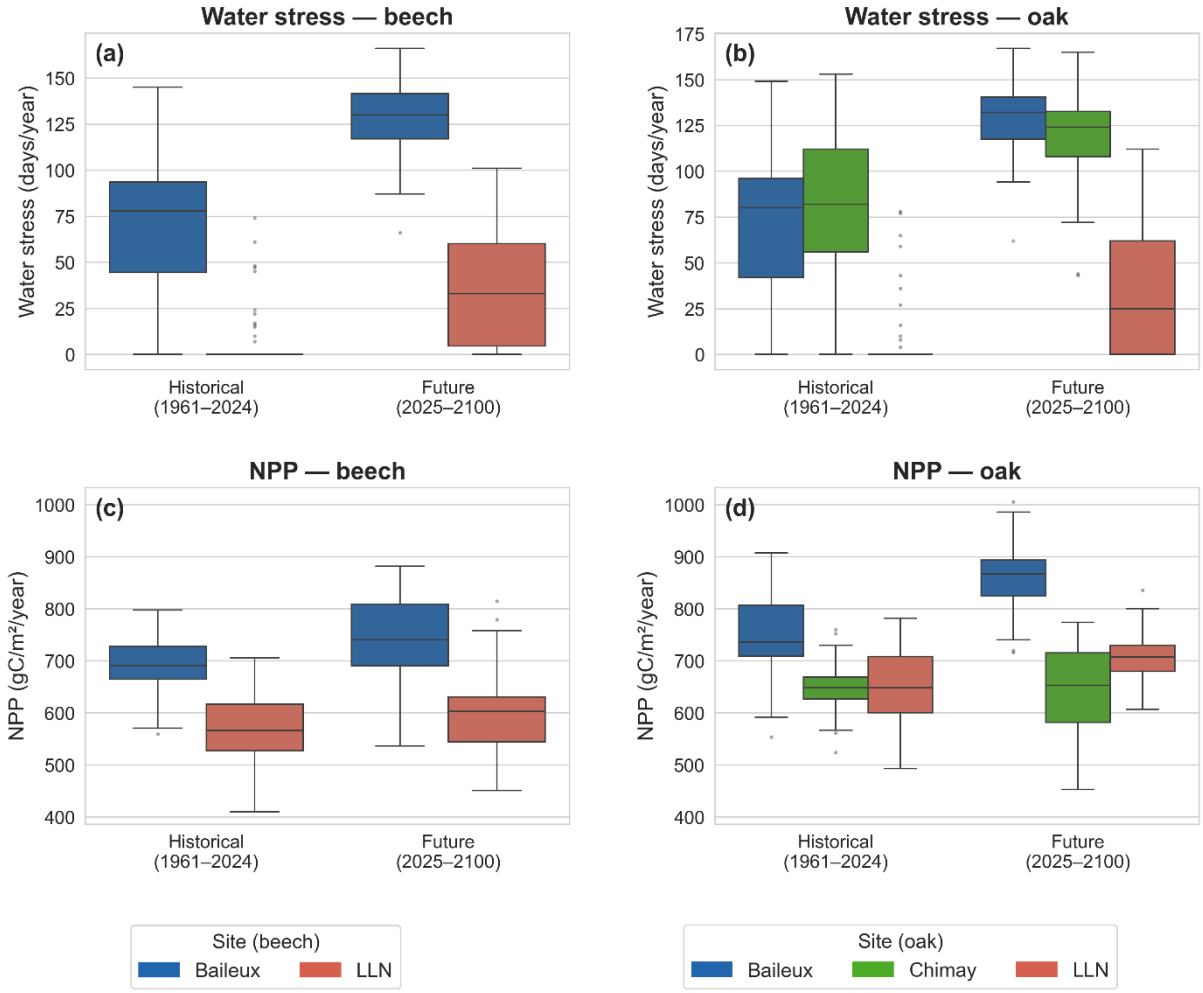

Figure 12. Site and species effects on water stress (a-b) and NPP (c-d) under historical and future CO_2 constant scenarios, without cavitation.

In a future period under constant CO_2, stress increases sharply at all sites. Sites that were historically more stressed remain so, but the LLN site, which was previously largely unaffected, is no longer spared. At Baileux, beech reaches a median of 130 days/year, representing a 67% increase, and at LLN, beech rises from 0 to 33 days/year. This difference illustrates how the buffering capacity of the soil at LLN mitigates stress in historical periods but does not prevent a sharp increase in stress in the future period. For oaks, the pattern is similar: Baileux and Chimay converge towards approximatively 130 days/year in the future, while LLN remains significantly less stressed (25 days/year).

However, no significant differences in water stress were observed between species at the same site (even if differences can visually be seen in Figure 10), suggesting that water stress (or at least the indicator used in this study) is primarily determined by local soil and climate conditions rather than by the functional traits of the species.

Differences in NPP are also marked and significant between the sites. During the historical period under constant CO_2 levels, Baileux recorded the highest NPP for beech and oak, both of which were significantly higher than at Chimay and the two stands at Louvain-la-Neuve. These differences reflect a

combination of local climatic conditions, notably higher rainfall for Baileux (1075 mm compared with 940 mm at Chimay and 818 mm at LLN), as well as the initial characteristics of the stands (structure, density, biomass, and development stage). The Baileux plots are notably younger than those at LLN and Chimay, and productivity tends to decline with age beyond a certain threshold (Ryan et al., 1997).

There are also clear and significant differences of productivity between species. Oak has a significantly higher NPP than beech at sites where both stands are studied. At Baileux, the difference is 56 gC/m²/year in the historical scenario and increases to 120 gC/m²/year in the future constant CO_2 scenario. At LLN, the pattern is similar, with a difference of 87 gC/m²/year in the historical scenario and 108 gC/m²/year in the future scenario. This superior productivity is consistent with the physiological parameters assigned to oak in HETEROFOR, which shows a more favourable NPP/GPP ratio as well as better hydraulic efficiency, with a xylem hydraulic conductivity of 25 compared to 15 for beech.

Activating the cavitation module significantly alters water stress and defoliation levels in most plots, while leaving the overall ranking across sites and species unchanged (Appendix B, figure B1). For water stress, the differences between simulations with and without the cavitation module are significant for all plots except Baileux beech. The most marked changes concern LLN, where the median historical stress increases from 0 to 29 and 45 days/year depending on the species. At Baileux oak and Chimay oak, the module also significantly increases historical stress (from 80 to 104 days/year and from 82 to 116 days/year respectively).

For the NPP, the cavitation module leads to significant increases at Baileux oak, LLN oak and LLN beech (future period), while Baileux beech remains unaffected in both periods. These results are consistent with those documented in section 3.1.4.

The differences in defoliation between the two scenarios are the most varied. The cavitation module significantly increases defoliation at Baileux beech (from 2.5% to 6.9% in the historical scenario, and from 1.7% to 9.7% in the future scenario) and at LLN beech (future scenario), from 2.8% to 8.4%. In contrast, it reduces it considerably in Chimay oak (from 8.2% to 2.3% in the historical scenario, from 9.8% to 3.1% in the future scenario). It is a counter-intuitive result already identified in section 3.1.4 and that will be discussed in section 4. Despite these quantitative differences, the rankings between sites, differences between species and the direction of future changes remain consistent between the two configurations for stress and NPP.

3.2.2. Climatic drivers of forest indicators

After characterizing these responses by site, species and the presence of the cavitation module, this section examines in greater detail the climatic factors underlying these variations. An analysis of Spearman's correlations between climatic variables and forest indicators reveals a clear hierarchy of climatic drivers, which stays true across all sites and species.

Water stress is primarily governed by summer rainfall and humidity, with strong and significant negative correlations across all plots (Figure 13). Historically, summer rainfall shows the strongest correlations for Baileux beech (ρ=-0.69) and Baileux oak (ρ=-0.75), while summer humidity dominates at LLN beech (ρ=-0.57) and LLN oak (ρ=-0.57). Temperature, both annual and summer, exerts a positive influence on stress in all cases, but to a smaller intensity than precipitation.

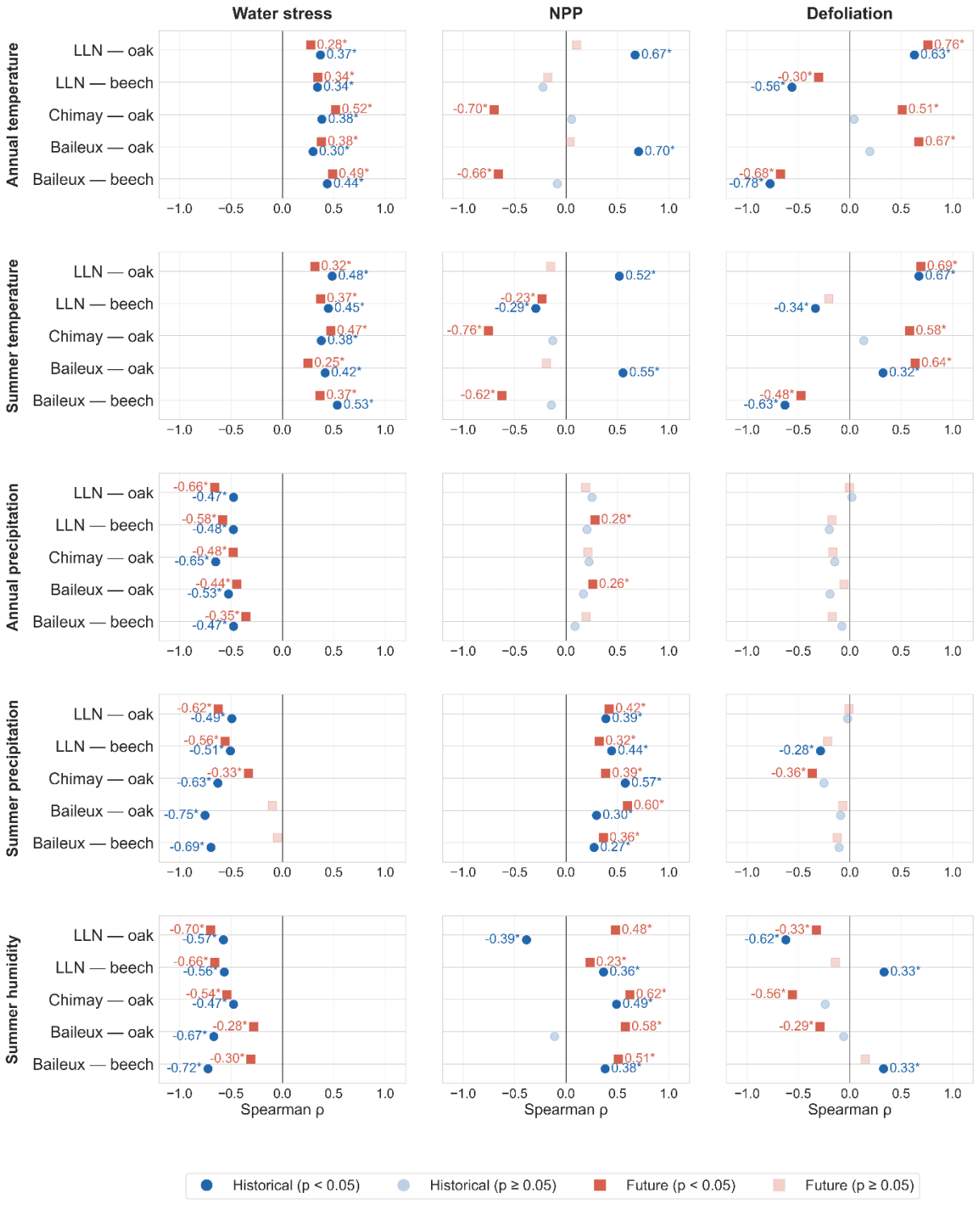

Figure 13. Spearman correlations between climatic variables and forest indicators across all stands, without cavitation. Filled symbols indicate significant correlations ($p < 0.05$).

In the future, this pattern changes slightly. The correlations with summer rainfall decrease for both plots in Baileux and become insignificant, while the correlations with temperature remain stable or increase slightly. This result suggests that in the future, when stress is high, its interannual variability is driven more by temperature than by summer rainfall.

The correlation analysis further reveals that water availability is becoming an increasingly important determinant of productivity in the future. Historically, summer rainfall and summer humidity show moderate positive correlations with NPP on most plots (ρ between +0.27 and +0.57), but their role remains secondary to that of temperature for oaks in the historical period.

In the future, this role becomes more pronounced. The correlations with summer rainfall and humidity become positive and significant across all plots (ρ between +0.32 and +0.62), reflecting the growing role of water availability as a limiting factor on productivity in a warmer climate. At the same time, annual precipitation becomes significantly correlated with NPP for certain plots (Baileux oak ρ=+0.26, LLN beech ρ=+0.28), whereas this signal was absent in the historical period. These results suggest that, in the future, forest productivity is jointly constrained by summer temperature and water availability. This reveals a shift from the historical period where temperature was the dominant driver of NPP and water availability played a more secondary role.

The results also depend heavily on the species when it comes to defoliation. For the Baileux beech, defoliation is strongly negatively correlated with annual temperature in the historical period (ρ=-0.63) and even more so in the future (ρ=-0.68). This confirms the anomaly already identified. The warmer is the summer, the lower is the defoliation of Baileux beech, regardless of water stress. In contrast, the oak trees at Baileux and LLN show strong positive correlations between temperature and defoliation in the future ($\rho = +0.67$ and $\rho = +0.76$). An analysis of defoliation by species within the Baileux beech plot reveals that this negative relationship is not attributable to Fagus sylvatica itself, which represents 74% of the stand and shows no significant correlation with temperature ($\rho = +0.08$, $p > 0.05$). Rather, it is driven primarily by Quercus (24% of the stand, $\rho = -0.58$, $p < 0.001$). This suggests that the negative temperature-defoliation relationship observed is primarily driven by the oak component of this mixed stand, rather than by beech itself. This point will be discussed further in Section 4.

The climatic drivers of water stress remain generally stable when the cavitation module is activated (Appendix B, Figure B3). Summer rainfall and humidity remain the main negative determinants of stress across all plots, and temperature maintains its positive influence. The hierarchy of climatic drivers of stress is consistent between the two configurations.

In contrast, the climatic controls of NPP and defoliation change more markedly. At LLN, the activation of cavitation introduces strong correlations between temperature and NPP in the historical period (ρ=+0.75 for LLN oak) as well as between temperature and defoliation in the future (ρ=+0.79 for LLN oak), which are absent without cavitation.

3.2.3. Interacting effects of temperature and water stress on NPP

This growing overlap between temperature and water as drivers of NPP is examined more formally in this section, which explicitly models their combined and interacting effects.

The analysis of the relationship between water stress and net primary productivity cannot be interpreted separately of the role of temperature. Indeed, these two variables are not independent. Part of the observed correlation between stress and NPP therefore already incorporates an indirect effect of temperature. To disentangle these effects, this section first examines the relationship between stress and NPP alone, then analyses how the relationship between temperature and NPP varies according to the level of water stress, and finally quantifies the respective contributions of these two factors and their interaction to NPP variability using a multiple regression model.

During the historical period, no significant correlation was observed between water stress and NPP across all plots (Figure 14). The Spearman coefficients were low and not significant, suggesting that historical stress levels generally remained below a critical threshold beyond which productivity would be affected (at year's scale). It should be noted that for LLN during the historical period, the near absence of stress (most years at 0 days) does not allow for a reliable interpretation of the relationship at this site.

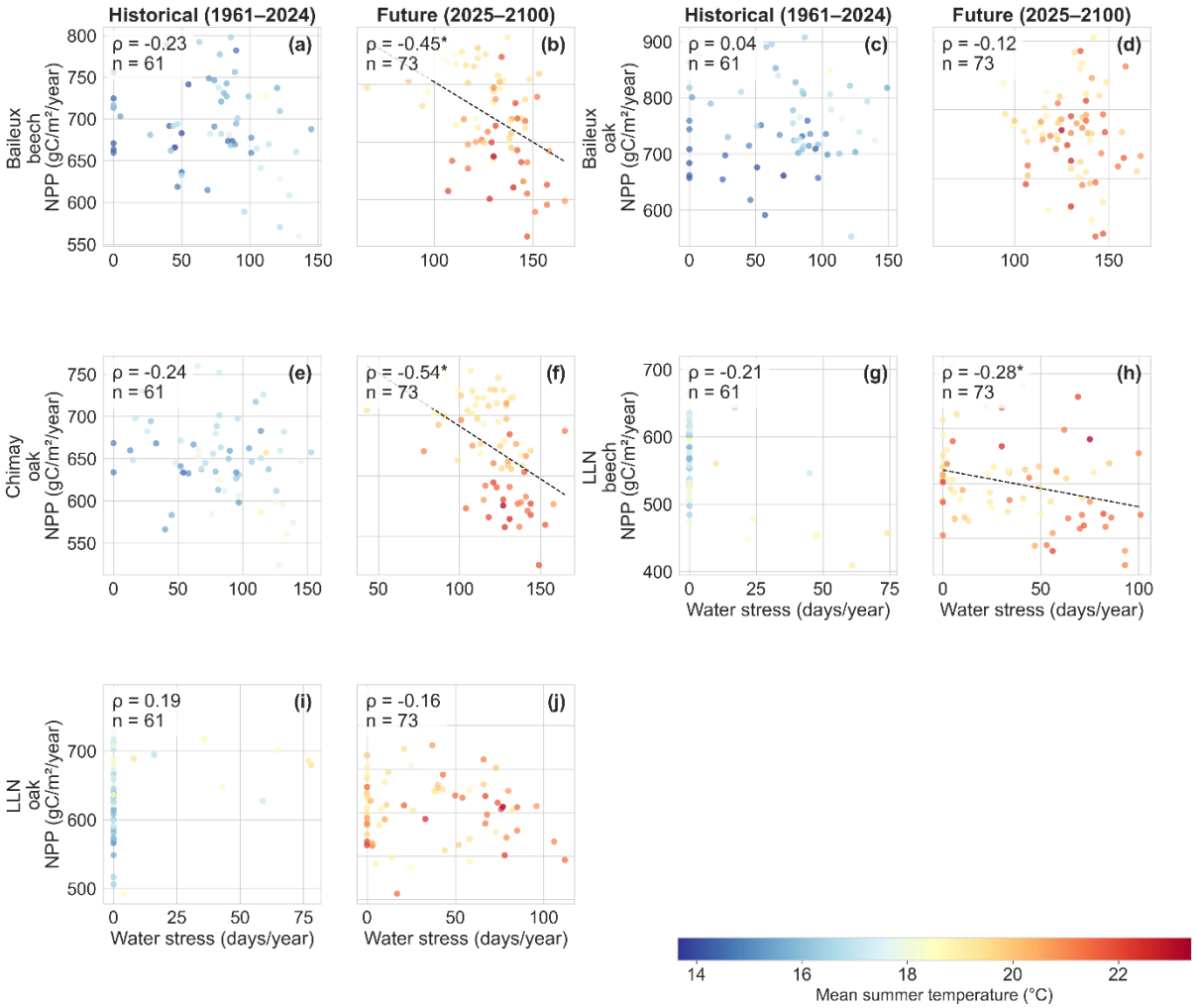

*Figure 14. NPP vs water stress for all stands under CO_2 constant scenarios, without cavitation. Colour indicates mean summer temperature. Dashed line = linear regression, drawn when the correlation is statistically significant. * $p < 0.05$.*

In the future, the relationship becomes significantly negative for several plots. The beech at Baileux shows a correlation of ρ = -0.45, the oak at Chimay the strongest (ρ = -0.54), and the beech at LLN a moderate but significant relationship (ρ = -0.28). These results indicate that, beyond a certain level of stress only reached in the future, water deficit becomes a limiting factor for forest productivity. The oaks at Baileux and LLN are exceptions, with non-significant future correlations, which is consistent with what has already been observed previously for oak at these sites.

As seen in 3.2.2, during the historical period, the relationship between summer temperature and NPP was positive or neutral for the majority of plots. The Baileux oak and the LLN oak show the strongest positive correlations (ρ = +0.55 and ρ = +0.52 respectively), indicating that warmer summers were associated with higher productivity under past climatic conditions. In the future, this relationship reverses or disappears for the majority of plots, with the strongest negative correlations observed for the Chimay oak (ρ = -0.76) and the Baileux beech (ρ = -0.63).

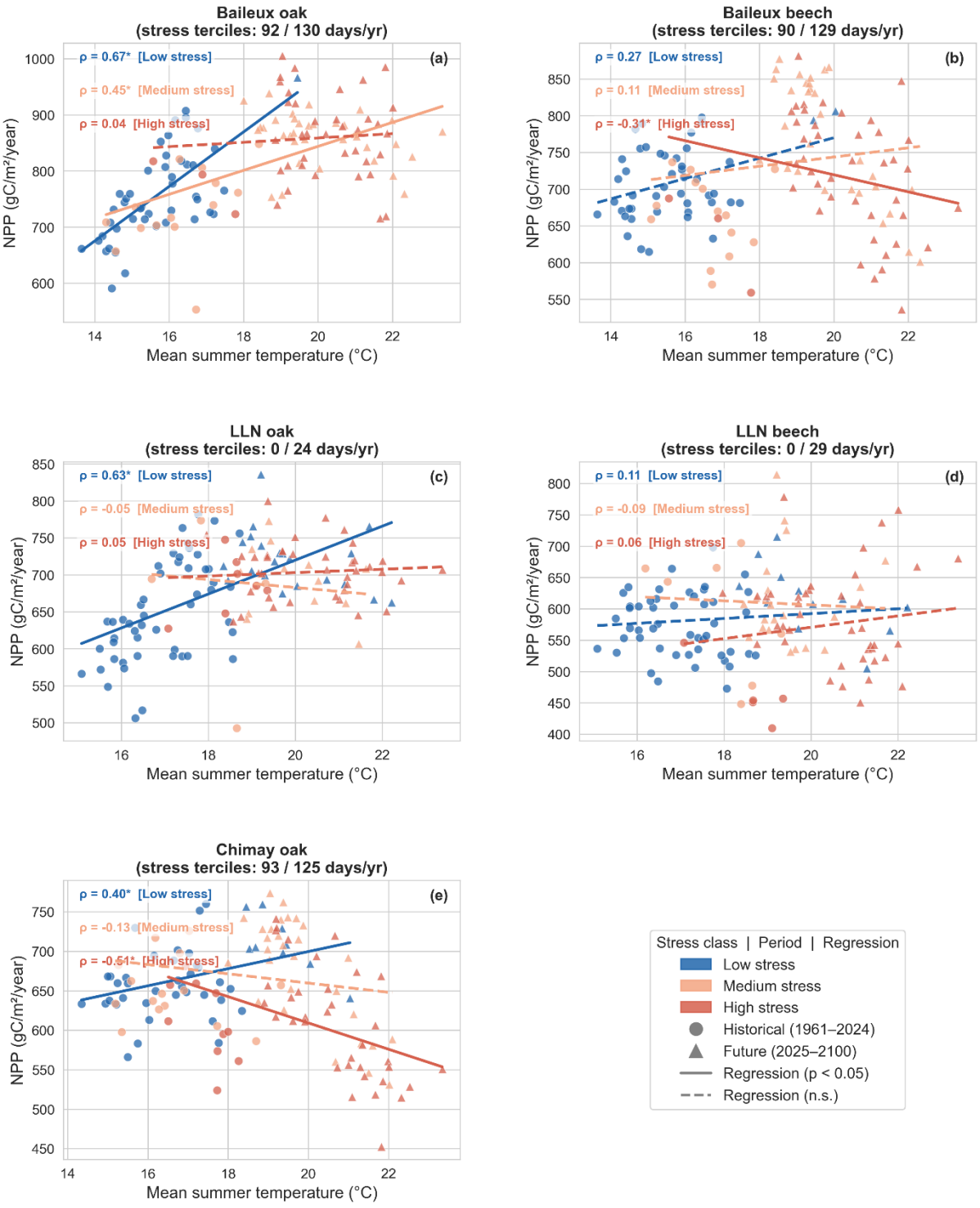

Figure 15. Relationship between net primary productivity (NPP) and mean summer temperature for each plot, distinguished by water stress class (defined by tertiles). Blue = low stress, orange = medium stress, red = high stress. Circles = historical period (1961-2024), triangles = future period (2025-2100). Solid lines indicate statistically significant regressions ($p < 0.05$), dashed lines indicate non-significant regressions. Stress tercile thresholds (in days/year) are indicated in the panel titles. All simulations use a constant CO_2 concentration.

A combined analysis of temperature and water stress reveals patterns that are more complex than those captured by the stress-NPP and temperature-NPP relationships alone. Figure 15 shows the relationship between NPP and mean summer temperature for each plot, distinguishing between three classes of water stress defined by tertiles. This separation allows us to visualise how the relationship between temperature and NPP changes depending on the level of stress.

Under low stress, the temperature-NPP relationship is positive for the majority of plots, which is consistent with the positive correlations observed historically. This positive relationship weakens progressively as stress increases, until it disappears or reverses under high stress. The clearest pattern is observed for the Chimay oak ($\rho = -0.51$ under high stress) and the Baileux beech ($\rho = -0.31$ under high stress), suggesting that beyond a certain stress threshold, higher summer temperatures no longer stimulate photosynthesis but, on the contrary, increase water deficit, forcing stomatal closure and reducing productivity.

In contrast, plots that have historically experienced little stress (particularly LLN) show weaker and less consistent relationships between stress classes, which is consistent with the absence of sufficient stress to modify the response to temperature. The beech stand at LLN remains the most atypical plot, with weak and non-significant correlations regardless of the stress class. The stress tertile thresholds, indicated in the title of each panel, differ between plots and illustrate the site effect already documented in section 3.2.1.

In order to quantify the respective contributions of temperature, water stress and their interaction to NPP variability, a multiple regression model was fitted separately for each species and each period, controlling for the effect of site. The model takes the form NPP ~ Temperature + Stress + Temperature×Stress, with standardised (centred and scaled) predictors to allow comparison of coefficients both with each other and across periods. The adjusted R^2 values are satisfactory, ranging from 0.41 for beech to 0.75 for oak in the future, indicating that the model captures the interannual variability in NPP well. The corresponding figure is presented in Appendix D.

The results confirm and quantify the patterns observed visually. During the historical period, temperature had a significant positive effect on the NPP of oak (+39 gC/m²/year per standard deviation, $p<0.001$), while its effect was negative for beech (-31 gC/m²/year, $p<0.05$). This can be explained by the fact that the beech in Baileux has historically been under stress (~78 days/year), so even in the past, the warmest years were already unfavourable for it. In the future, this effect becomes negative for both species (beech: -34 gC/m²/year; oak: -35 gC/m²/year), reflecting the regime shift already identified. Water stress has a significant negative effect during the historical period for both species, but loses its significance in the future. This result can be explained by the fact that stress becomes chronically high in the future, reducing its interannual variability and thus its explanatory power. It is then the temperature that becomes the main differentiating factor from one year to another.

The temperature×stress interaction term is negative and significant in both periods and for both species. This confirms that the combined effect of heat and stress is consistently unfavorable to productivity, regardless of the period. This term increases slightly in the future for beech (-30 for historical, -37 for future) and decreases for oak (-36 for historical, -21 for future), suggesting a different sensitivity between species to climate intensification.

These results show that temperature and water stress act together to influence forest productivity, with a consistently negative interaction regardless of the period or species considered. Under future climate conditions, summer heat ceases to be a stimulating factor and becomes a limiting factor, particularly when combined with high water stress. This transition has already begun for beech in the past and will extend to oak in the future, demonstrating the increasing vulnerability of both species to projected climate intensification.

The results presented before are generally consistent with those obtained with the cavitation module enabled, which reinforces their robustness. The temperature×stress interaction term remains negative and significant in both configurations for the majority of cases. However, two notable differences are

worth mentioning. Firstly, for the beech in the future, the interaction loses its significance with cavitation ($p = 0.092$ whereas $p < 0.01$ without cavitation), suggesting that cavitation alters the stress-temperature dynamics for this species under future conditions. Secondly, for the oak in the future, the water stress coefficient reverses to become strongly positive with cavitation (+53 gC/m²/year, $p<0.001$). This result is specific to the cavitation configuration. While LLN experiences little or no water stress under the standard configuration (as documented in section 3.2.1), the cavitation module generates hydraulic stress even during historical years at this site, complicating the relationship between annual stress days and productivity (this point will be further discussed in section 4). These results suggest that the main conclusions are robust, but that the interpretation of the role of water stress alone depends on the HETEROFOR configuration. The corresponding figures with the cavitation module are presented in the Appendix D.

3.2.4. Relationship between water stress and defoliation

The relationship between water stress and defoliation varies markedly across plots. At the overall level, the correlations are almost zero and not statistically significant, with $\rho = +0.06$ for the historical period and $\rho = +0.08$ for the future, confirming the absence of a consistent signal across Wallonia without the cavitation module activated.

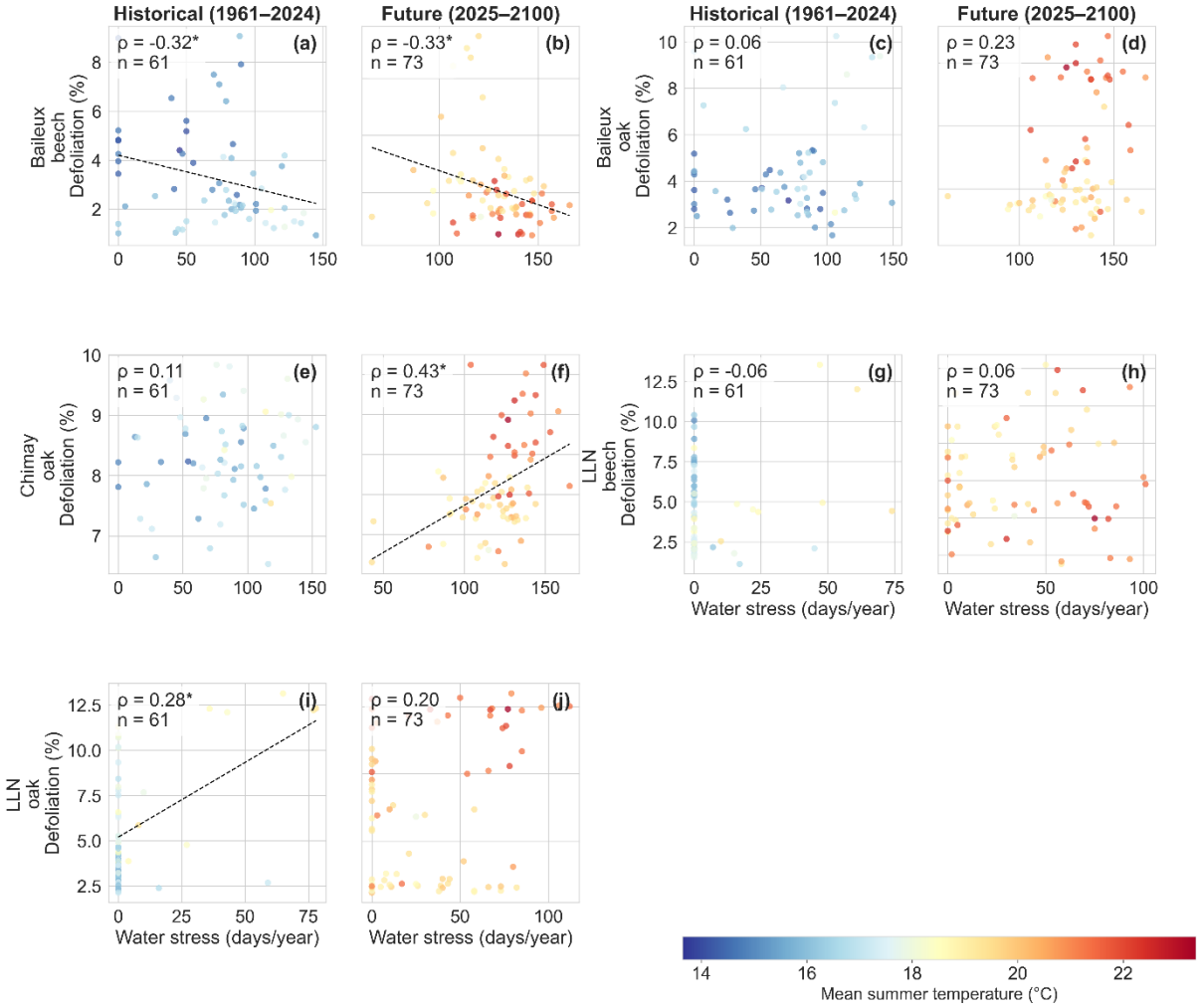

*Figure 16. Defoliation vs water stress for all stands under CO_2 constant scenarios, without cavitation. Colour indicates mean summer temperature. Dashed line = linear regression, drawn when the correlation is statistically significant. * $p < 0.05$.*

At the plot level, two opposing patterns coexist (Figure 16). The Baileux oaks' plot and the Chimay oaks' plot show positive relationships between stress and defoliation, the intensity of which increases in the future. For Chimay, the correlation shifts from non-significant in the historical period (ρ=+0.11, $p>0.05$) to significantly positive in the future (ρ=+0.43, $p<0.05$). Baileux shows a similar trend but does not reach the significance threshold in the future.

On the other hand, the Baileux beech plot shows a significantly negative relationship between stress and defoliation, both in the historical period (ρ = -0.32) and in the future period (ρ = -0.33). This counter-intuitive result, which persists across both periods, cannot be directly explained by the model parameters and will be discussed in section 4.

The LLN plots show weak and non-significant correlations in both periods (ρ ranging from -0.06 to +0.28), which is consistent with the low historical stress levels at this site. In the future period, despite the increase in stress at LLN, no significant relationship emerges, suggesting that factors other than water stress continue to dominate defoliation dynamics at this site. LLN oak is an exception, showing a weakly significant positive correlation in the historical period (ρ=+0.28, $p<0.05$) that diminish in the future, without being significant anymore (ρ=+0.20, $p>0.05$).

These results indicate that, in the absence of the cavitation module, when defoliation is only due to competition, a detectable stress-defoliation relationship only emerges for oaks at the most stressed sites.

Activating the cavitation module radically alters the relationship between water stress and defoliation (Appendix B, Figure B4). Without cavitation, clear patterns emerge for several plots, with a persistent negative correlation for Baileux beech and a significant positive correlation for Chimay oak in the future. With cavitation, almost all of these correlations disappear or become insignificant. Only LLN oak shows significant correlations with cavitation, and in a positive direction (ρ=+0.38 historically, ρ=+0.46 in the future). This justifies the use of the results obtained without the cavitation module as the principal reference for this section.

When considering only the cavitation-driven defoliation component, the relationship with water stress becomes consistently positive across nearly all plots (ρ ranging from -0.13 to +0.36), with significant correlations observed for Baileux oak (ρ=+0.27 historically, ρ=+0.36 in the future), LLN oak (ρ=+0.27 and ρ=+0.31) and LLN beech in the future (ρ=+0.27) (Table 5). This confirms that the cavitation module generates hydraulic defoliation in a mechanistically consistent manner with respect to water stress, even though the signal is partially masked at the total defoliation level by the competition component.

*Table 5. Spearman correlations between water stress (days/year) and cavitation-driven defoliation across all plots, for the historical (1961-2024) and future (2025-2100) periods, with the cavitation module activated. * indicates significant correlation ($p < 0.05$); n.s. = non-significative.*

Plot	**Historical**	**Future**
Baileux beech	ρ = +0.18 n.s.	ρ = +0.09 n.s.
Baileux oak	ρ = +0.27*	ρ = +0.36*
Chimay oak	ρ = -0.13 n.s.	ρ = +0.18 n.s.
LLN beech	ρ = -0.01 n.s.	ρ = +0.27*
LLN oak	ρ = +0.27*	ρ = +0.31*

3.3 Evolution of climate extremes

3.3.1 Changes in distributions

Climate change not only shifts the central tendency of distributions but also alters their shape and variability. The most pronounced change is in water stress (Figure 17). For sites that were initially under little stress, the distribution undergoes a radical change (Appendix F). For LLN beech, the historical distribution is concentrated at zero (p_{50}=0, p_{75}=0, p_{90}=22 days), whereas the future distribution spans the entire range from zero to 100 days (p_{50}=33, p_{90}=81 days). This shift from a highly concentrated distribution to a more spread distribution means that years with no stress, which historically were the majority, becomes the exception in the future. The same pattern is observed for LLN oak (p_{50} going from 0 to 25 days, p_{90} from 27 to 79 days). For sites that have historically been under stress, the pattern is different. In the future period, the distribution is concentrated around high values. At Baileux beech, the interquartile range decreases from 51 to 25 days, and at Baileux oak from 52 to 23 days. The interannual variability of stress is reduced by half, indicating that stress is becoming chronic and relatively stable between years rather than episodic and intense.

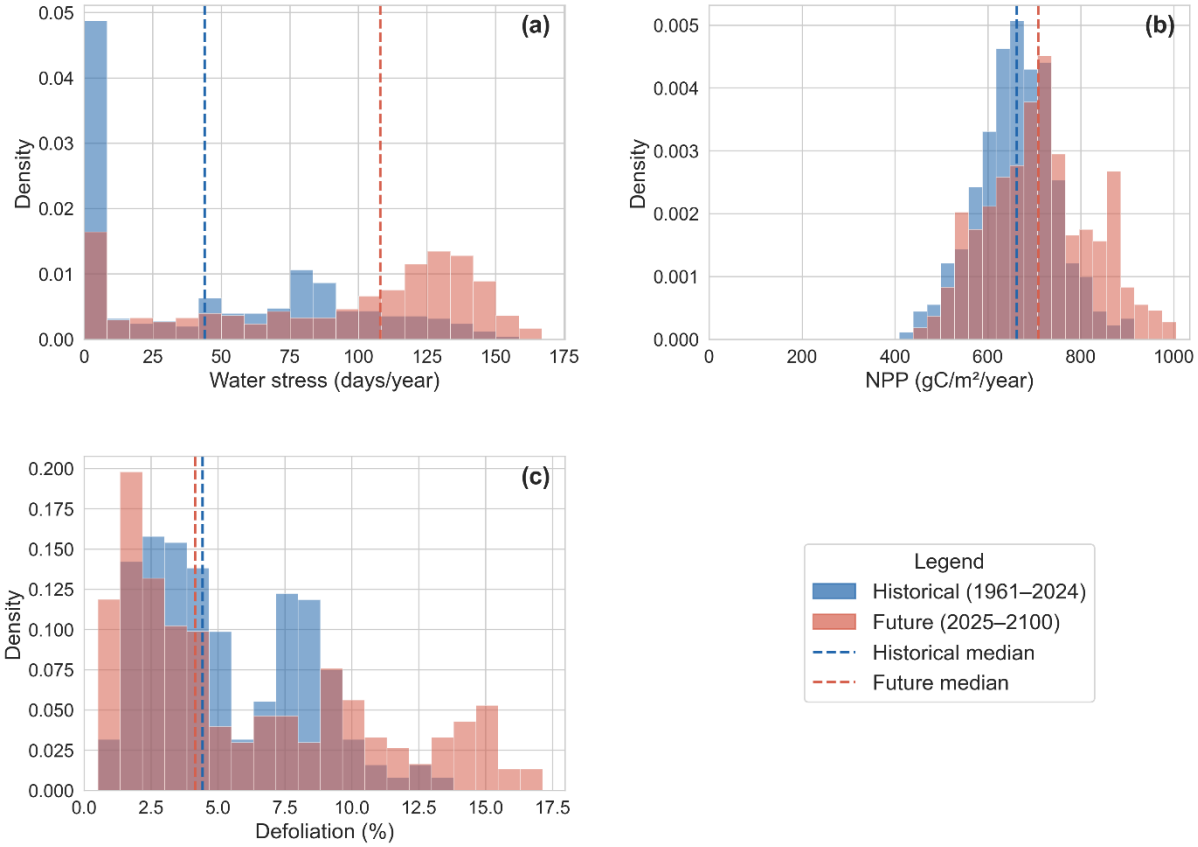

Figure 17. Historical vs future distributions of water stress (a), NPP (b) and defoliation (c) across all stands, without cavitation, at constant CO2. Dashed lines indicate medians.

NPP distributions vary markedly across sites (*Appendix F*). At Baileux oak, the distribution has shifted toward higher values, reflecting an overall increase in future productivity. For Chimay oak, the median remains generally stable, but the distribution is widening toward lower values, with a marked decline in the p_{10}. This suggests that, even though average productivity has changed little, unfavorable years are becoming more severe. For LLN beech and LLN oak, future distributions also show a slight shift toward

higher values, without a notable increase in variability, which is consistent with relatively limited water stress at these sites.

The defoliation distributions show the most heterogeneous patterns across plots (*Appendix F*). Baileux beech exhibits a decrease in median defoliation (from 2.5% to 1.7%) with a narrowing of the distribution (interquartile range from 2.4% to 1.2%), while Baileux oak shows an increase accompanied by a very sharp widening toward high values (p_{90} from 7.4% to 14.3%). LLN oak presents the most extreme case with a p_{90} reaching 14.8% and an interquartile range increasing from 4.6 to 11.6%. These heterogeneous patterns across plots reflect the contrasting responses between species and sites identified in the previous section and will be further interpreted in the discussion.

The activation of the cavitation module significantly alters the distributions for the majority of plots, but does not change the key findings documented in this section. For water stress, the differences are most pronounced at LLN, where the historical median ranges from 0 to 29 and 45 days/year depending on the species, and where the future median increases sharply (from 33 to 93 days/year for LLN beech, from 25 to 104 days/year for LLN oak). The shift from a distribution concentrated around zero to a more spread distribution, documented without cavitation, is therefore even more pronounced with the cavitation module. At Baileux, the distributions remain concentrated around high values in both configurations, and the reduction in interannual variability in the future is confirmed (IQR decreasing from 51 to 25 days for Baileux beech without cavitation, and from 71 to 27 days with cavitation).

For the NPP, the differences between configurations are significant for Baileux oak, LLN oak and LLN beech (future), but the patterns of change from the historical to the future remain consistent across the two configurations. For defoliation, the differences are most pronounced (notably at Chimay oak), where the median decreases from 8.2% to 2.3% with cavitation, and at Baileux beech, where it increases from 2.5% to 6.9%. These differences, already documented in section 3.2.1, confirm that defoliation is the indicator most sensitive to the model configuration, logically. The histogram distributions obtained with the cavitation module are presented in Appendix B.

3.3.2 Impact of extreme dry years on productivity

To quantify the impact of the most severe drought events, years exceeding the 90th percentile of water stress were defined as “extreme dry years” for each plot and each period separately. This approach allows for a comparison of the relative impact of extremes across periods, independently of the overall increase in stress.

Historically, the impact of extreme dry years on NPP varies greatly by site (Figure 18). LLN beech shows the highest relative loss (-20.3%), even though it is the site with the lowest threshold (22 days/year). In contrast, Baileux oak is unaffected by dry years (-1.9%), confirming the oak’s resilience at this site. LLN oak even shows slightly higher productivity during dry years (+5.6%), consistent with the historically observed positive relationship between stress and NPP at this plot.

In the future, extreme thresholds rise at all sites, reflecting the general intensification of stress documented previously. Chimay oak experiences the biggest decline, with a loss in NPP during dry years increasing from -3.9% to -15.2%. Furthermore, the NPP observed during these future dry years falls below the NPP of historical normal years, indicating that the increase in average water stress is accompanied by extreme years that are particularly unfavourable for productivity. In contrast, LLN beech shows a reduction in relative loss (-20.3% to -10.1%). This does not reflect improved conditions, but rather a convergence between normal and extreme years. As stress becomes more frequent in the

future, the threshold defining extreme years rises from 22 to 81 days/year, and normal years themselves become increasingly stressful, reducing the relative contrast between the two categories.

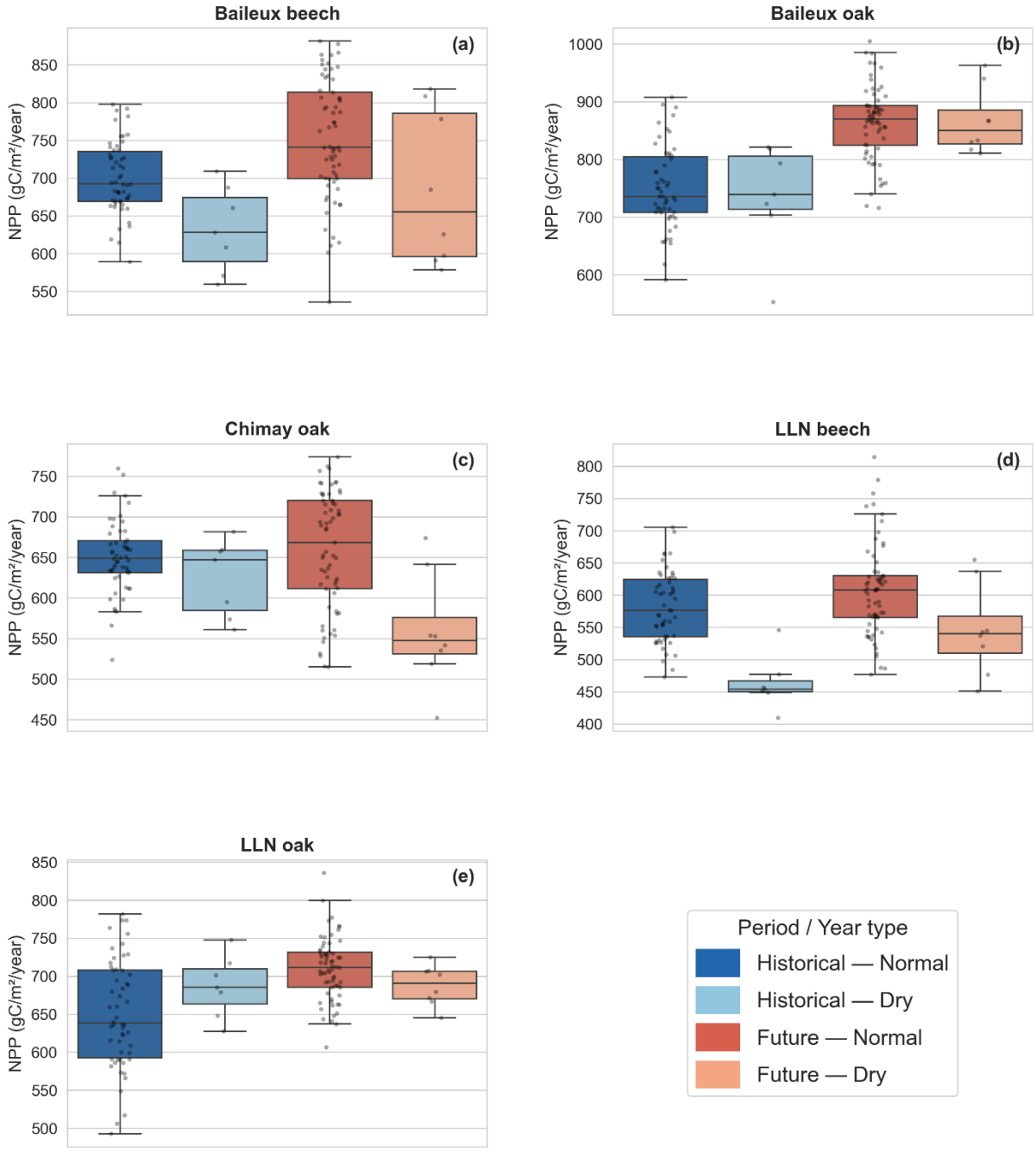

Figure 18. NPP in dry vs normal years for all stands, without cavitation and with constant CO2. Dry years defined as years exceeding the 90th percentile of water stress, computed separately for each period.

With the cavitation module, the overall patterns remain broadly consistent, but with notable differences for certain plots. Chimay oak shows an even more pronounced decline in the future (-17.2% with cavitation versus -15.2% without), confirming this plot's increasing vulnerability to extreme years. LLN beech also shows greater losses in both periods (-16.1% in the historical scenario and -22.9% in the future scenario, compared with -20.3% and -10.1% without cavitation). Contrary to what was observed without cavitation at LLN, the loss associated with dry years is therefore intensifying in the future rather than decreasing.

The exceptions identified in the absence of cavitation persist in the presence of cavitation. Baileux oak remains virtually unaffected by future dry years (-1.3% with cavitation versus -1.9% without), and LLN oak continues to show slightly higher productivity during historical dry years (+12.5% with cavitation versus +5.6% without). These results confirm the consistency of these patterns between the two model configurations. The figures in this section obtained with the cavitation module enabled are presented in Appendix B.

3.3.3 Temporal dynamics and underlying mechanisms of NPP decline

While years of extreme drought allow us to quantify the impact of the most severe episodes, they do not provide information on the temporal dynamics of productivity or the physiological mechanisms that govern it. The time series presented in this section (Figure 19) enable us to examine the joint evolution of NPP, gross primary productivity (GPP), leaf area index (LAI) and transpiration deficit over the entire simulated period, in order to identify the processes underlying the decline in productivity observed in the second half of the 21st century.

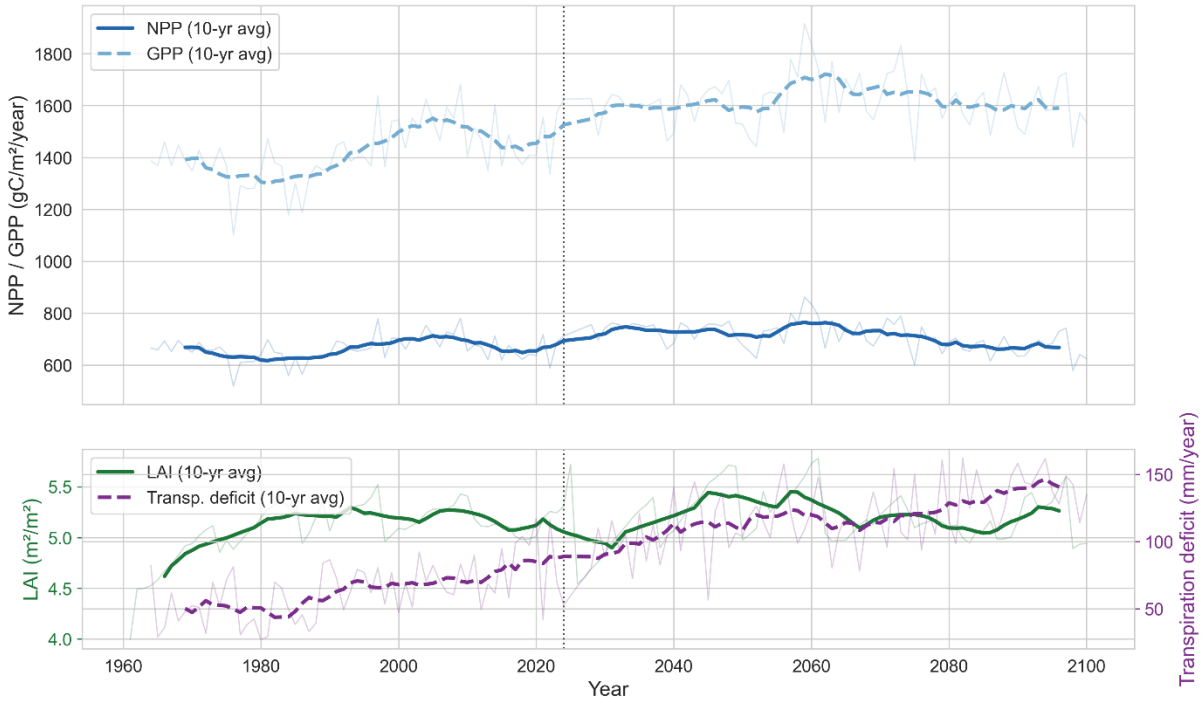

Figure 19. Mean time series of net primary productivity (NPP, dark blue) and gross primary productivity (GPP, light blue dashed), leaf area index (LAI, green) and transpiration deficit (purple dashed) averaged across all five plots, under constant CO_2 scenarios (1961-2100). Thin lines show annual values; thick lines show 10-year moving averages. The vertical dotted line indicates the transition between the historical period (1961-2024, IRM observed climate data) and the future period (2025-2100, GFDL-ESM4 climate simulations).

Firstly, discontinuities might be visible in the figures between 2024 and 2025 and require a methodological explanation. Structural biomass is reset at the start of each simulation using the same field inventory. This means that the historical simulation starting in 1961 and the future simulation starting in 2025 both have the same initial conditions. This explains the sudden drops in LAI visible in 2024 for certain plots. Secondly, a jump in productivity is sometimes visible at this same date, reflecting the change in climate forcing. The historical period uses interpolated observational data from the IRM, while the future period uses simulations from the GFDL-ESM4 climate model, which exhibits a positive temperature bias relative to observations and that will be analysed in Section 3.4.

Across all plots, the average NPP exhibits three distinct phases during the simulated period. During the historical period, it increases moderately from ~630 to ~710 gC/m²/year between 1960 and 2020, reflecting climatic conditions that were generally favourable to forest growth. In the future, it rises initially, peaking around 2055-2060 (~760 gC/m²/year), before declining gradually to return by the end of the century to a level comparable to that of the 1960s (~665 gC/m²/year). This result suggests that the productivity gains accumulated during the 20th century could be entirely wiped out by 2100 under the SSP3-7.0 climate scenario with constant CO_2 levels. However, this overall pattern masks significant contrasts between plots, which will be detailed in a following paragraph (figures separated by plots are presented in Appendix E). This three-phase pattern is also more pronounced for beech than for oak when species are considered separately (Appendix E).

A joint analysis of GPP and NPP reveals an unexpected pattern. While NPP declines from the 2060s onwards, GPP continues to increase throughout the entire future period, rising from around 1,450 to over 1,600 gC/m²/year on average. The gap between the two indicators therefore increases gradually in the second half of the 21st century, indicating an increase in the proportion of GPP consumed by autotrophic respiration. This result suggests that the decline in NPP is not primarily due to a reduction in gross photosynthesis. The implications of this divergence will be discussed in Section 4.

Changes in LAI and transpiration deficit provide further information on the mechanisms at play. LAI remains remarkably stable throughout the simulated period, fluctuating between 5.0 and 5.4 m²/m² without any marked trend. This result indicates that the decline in NPP is not associated with a generalised loss of leaf area. In contrast, the transpiration deficit increases continuously and sharply in the future, rising from around 75-80 mm/year historically to approximatively 150 mm/year by the end of the century. This divergence between a stable LAI and a growing transpiration deficit suggests that the constraint is primarily stomatal and hydraulic in nature. The leaves are present, but their functioning is increasingly limited by water deficit.

This overall pattern masks significant contrasts between individual plots. Chimay oak shows the most marked decline in NPP, with a moving average falling from ~720 to ~550 gC/m²/year between 2060 and 2100. It is the only plot where GPP also begins to decline by the end of the century, indicating a stress intense enough to affect gross photosynthesis itself. Baileux beech shows a similar but earlier decline, beginning as early as the 2050s. For these two plots, LAI shows a marked decline in the second half of the 21st century, coinciding precisely with the most pronounced NPP declines.

On the other hand, Baileux oak and LLN oak show remarkably stable NPP throughout the entire future period despite increasing GPP, confirming the resilience of these plots already documented in the previous sections. The LAI of Baileux oak increases gradually until the 2060s before stabilising, while the transpiration deficit there remains moderate. LLN beech exhibits the most atypical pattern, with very high interannual variability and an unclear trend, consistent with the results of section 3.2.3.

The results obtained using the cavitation module are presented in the Appendix B. Across all plots, the transpiration deficit is significantly higher with cavitation (~150 mm/year historically compared to ~75 mm/year without cavitation), and the divergence between GPP and NPP is more pronounced by the end of the century, with GPP declining more sharply after 2070. For the majority of individual plots, however, the patterns are similar to those described above. Two exceptions are worth mentioning. For Chimay oak, the decline in NPP and GPP is earlier and more pronounced with cavitation, with GPP beginning to decline as early as the 2060s rather than after 2080. For LLN beech, cavitation produces a significant qualitative change. While this plot exhibited relatively stable NPP without cavitation, it shows a marked decline in NPP, GPP and LAI in the latter part of the 21st century with cavitation. These

differences are consistent with the effect of the module on the water stress regime at these sites, as documented in section 3.1.4.

3.3.4 Seasonality and duration of drought episodes

The changes in NPP documented in the previous sections are the result not only of an increase in total annual water stress, but also of changes in the temporal pattern of drought episodes during the growing season. To test this, the maximum duration and the number of drought episodes per year were correlated with annual NPP for each plot and each period.

The temporal pattern of water stress remains consistent between the historical and future periods, with peaks still concentrated in August and September, but its intensity and seasonal extent are changing. In the historical period, stress begins in May and peaks in September. In the future period, it intensifies throughout the growing season, appearing as early as April and continuing until October. This extension reduces the window for soil water recovery between consecutive episodes, increasing the risk of cumulative stress over the entire season.

Analysis of consecutive drought episodes reveals contrasting patterns across sites. In Baileux, the change is mainly reflected in longer episodes. The median duration increases from 41 to 117 days for beech and from 40 to 119 days for oak, while the number of episodes remains stable. In Chimay, the median duration increases more moderately (from 22 to 42 days), but the number of episodes increases strongly. LLN shows the most marked contrast in terms of frequency. Historically, episodes there were very rare (16 for beech and 17 for oak over 63 years), but their number is rising strongly in the future to 88 and 81 respectively, while maintaining moderate median durations (17-22 days).

These structural differences in drought episodes have measurable consequences for annual NPP. The maximum duration of episodes shows significant negative correlations with NPP at Baileux beech (ρ=-0.44, future only), Chimay oak (ρ=-0.33 historical, ρ=-0.47 future) and LLN beech (ρ=-0.72 historical, ρ=-0.26 future). The strengthening of this relationship between the historical and future periods at Baileux beech and Chimay oak is consistent with the hypothesis that the duration of episodes only becomes a limiting factor for productivity when episodes exceed a critical length (more frequently reached in the future period). In contrast, Baileux oak and LLN oak show no significant correlation in either period (ρ between -0.06 and -0.23), which is again consistent with the better hydraulic resilience of oak documented in section 3.2.2.

At LLN, where the predominant change is an increase in the frequency rather than the duration of episodes, the number of episodes does not show a significant negative correlation with NPP (ρ between -0.14 and -0.48, not significant), suggesting that the increase in the number of short episodes at this site does not, on its own, reduce annual productivity. At Chimay, the number of episodes becomes weakly but significantly correlated with NPP in the future (ρ=+0.24), with a counter-intuitive positive sign. One possible explanation is that a high number of short episodes reflects a pattern of alternation between wet and dry periods, which is less damaging to productivity than a single prolonged episode. However, this result should be interpreted with caution given the weak correlation.

With the cavitation module, the relationship between episode duration and NPP is modified for some of the plots. Baileux future beech remains significant (ρ=-0.38 compared with ρ=-0.44 without cavitation), confirming the robustness of this result. LLN future beech shows an increased correlation (ρ=-0.54 compared to ρ=-0.26 without cavitation), which is consistent with the increase in chronic stress at this site when the module is activated. In contrast, Chimay oak loses its significant correlations in both

periods, showing that the duration-NPP relationship at Chimay is sensitive to the model configuration. Baileux oak and LLN oak remain non-significant in both configurations, confirming the hydraulic resilience of oak documented in section 3.2.2.

3.4 Climate model biases and their propagation into HETEROFOR

The results presented in sections 3.1 to 3.3 are based on two distinct climate sources: IRM observations for the historical period (1961-2024), and GFDL-ESM4 data (corrected in accordance with the ISIMIP3 protocol) for the future period (2025-2100). However, as discussed in the review of the current state of the art, climate models tend to underestimate recent warming in Europe. The following section assesses the extent to which this climate bias propagates into the HETEROFOR outputs and affects the forest projections.

3.4.1 Climatic bias between GFDL-ESM4 and IRM interpolation

Before analysing the propagation of climate biases in HETEROFOR outputs, it is necessary to document the climate biases themselves. The comparison covers the common historical period 1961-2024, focusing on summer temperatures (June-August), for which the CMIP6 models show the largest discrepancies compared with observations in Western Europe. The GFDL-ESM4 data used in this comparison are the data corrected in accordance with the ISIMIP3 protocol (see Methodology). In other words, these are the data that are actually used as climate forcing in HETEROFOR, and the comparison therefore reflects the residual bias that actually affects the simulations.

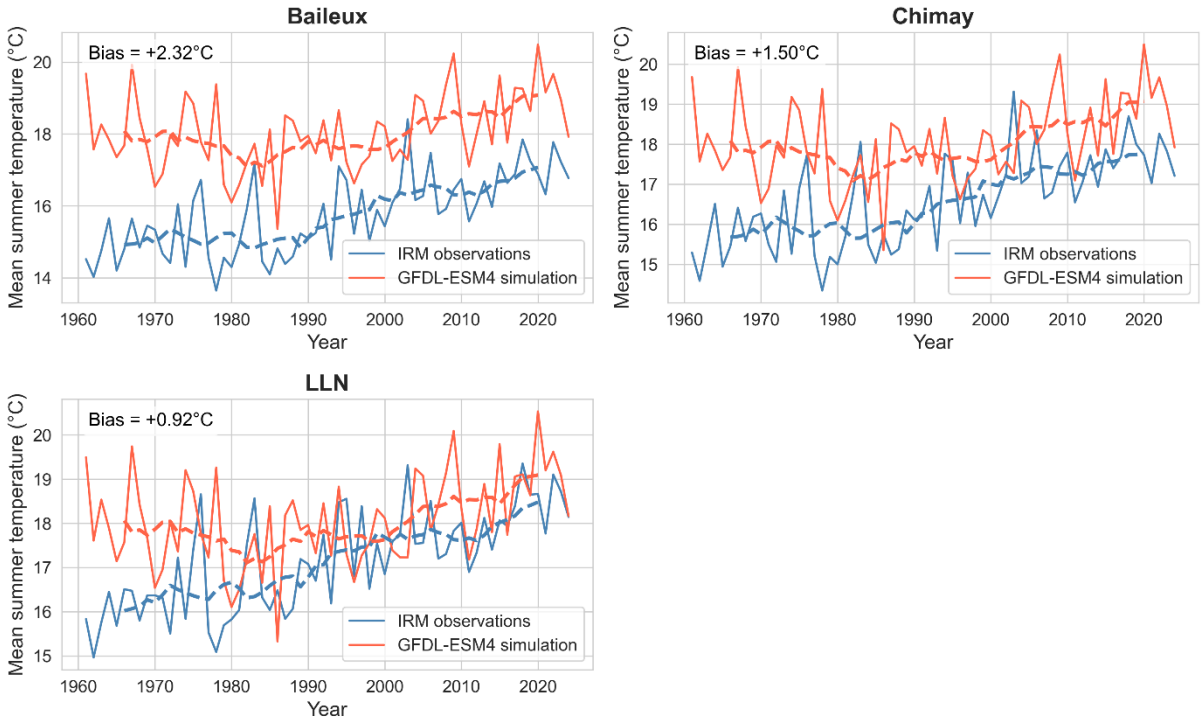

Figure 20. Temporal evolution of mean summer temperature (June-August) as simulated by GFDL-ESM4 and interpolated from IRM observations for the three study sites (1961-2024). Solid lines show annual values, dashed lines show 10-year moving averages.

Figure 20 shows the temporal evolution of the average summer temperature as simulated by GFDL-ESM4 (after correction), and interpolated using the IRM's observations for the three sites. GFDL-ESM4,

even after correction, systematically overestimates summer temperatures throughout the period, with an average bias of +2.32°C at Baileux, +1.50°C at Chimay and +0.92°C at LLN.

It is important to note that these biases exist despite the ISIMIP3 correction described in the Methodology section. This correction, applied using trend-preserving quantile mapping, is calibrated over the period 1976-2014 (Lange, 2019). The comparison presented here therefore extends 15 years before and 10 years after this window. It adjusts the distribution of the simulated variables so that it matches the observed distribution while preserving the model's trends. It therefore corrects for mean and distribution biases, but does not alter the temporal dynamics of the warming simulated by the model. When comparing the bias actually observed outside the calibration window with that predicted by a simple extrapolation of the calibrated trend, a systematic positive bias is observed at all three sites (between +0.6 to +1.0°C before 1976 and +0.2 to +0.5°C after 2014) indicating that the residual bias over the entire period is also explained in part by the limitations of extrapolation beyond the calibration window.

A Mann-Kendall test (explained in the Methodology section) was applied to the annual bias series and revealed a significantly decreasing trend at all three sites (tau = -0.21 to -0.23, $p < 0.05$). The Sen slope is approximately -0.02°C/year for the three sites, corresponding to a reduction in bias of approximately 1.3°C over the 1961-2024 period. This result indicates that the bias is not constant, but that GFDL-ESM4 warms less rapidly than IRM observations over the historical period. Simulated temperatures gradually converge towards the observations, implying that the simulation underestimates the rate of recent warming, although it overestimates summer temperatures.

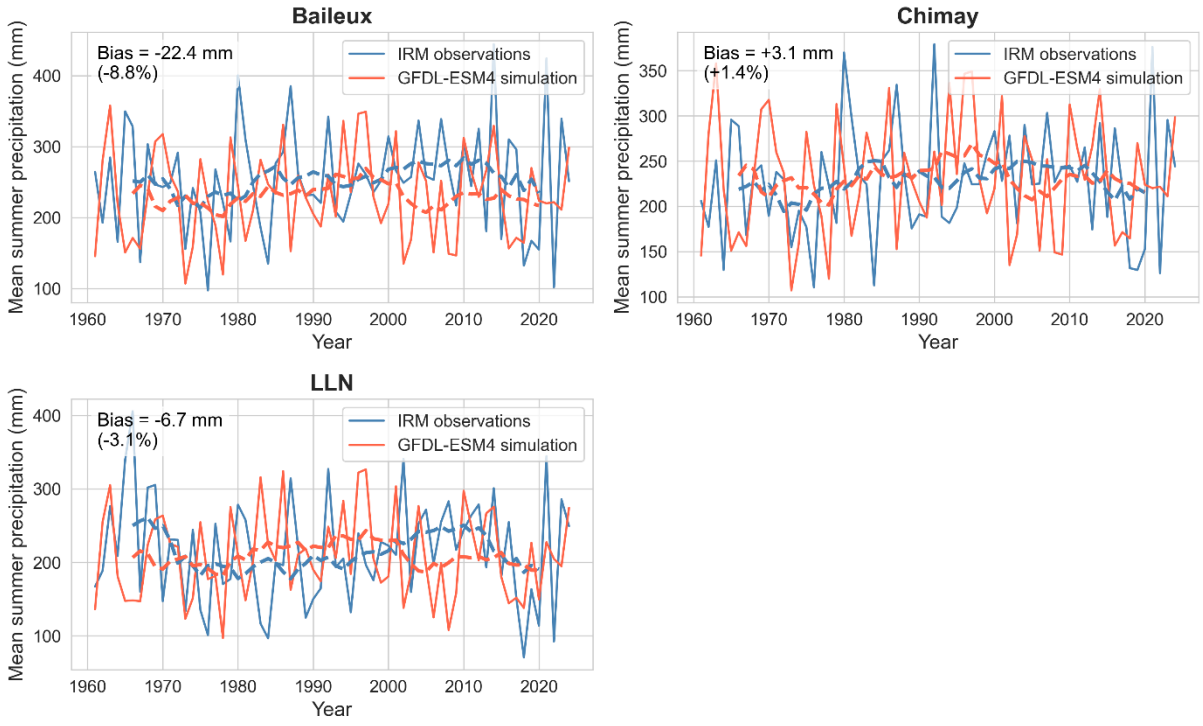

Figure 21. Temporal evolution of total summer precipitation (June-August) as simulated by GFDL-ESM4 and interpolated from IRM observations for the three study sites (1961-2024). The annotated bias corresponds to the mean difference over the full period, expressed in mm and as a percentage of the observed mean.

Unlike temperature, summer precipitation biases are small and do not show any significant temporal trend (Figure 21). GFDL-ESM4 slightly underestimates precipitation on average at Baileux (-22.4 mm, or -8.8%) and at LLN (-6.7 mm, or -3.1%), while the bias is virtually zero at Chimay (+3.1 mm, or

+1.4%). The Mann-Kendall test detects no significant trend in the time series of biases for any of the three sites.

These results indicate that the precipitation bias is of small magnitude and does not show a clear trend across sites. This contrasts with the temperature bias, which is both larger in magnitude and decreases significantly over the period.

The ISIMIP3 correction also shows limitations in reproducing the amplitude of the interannual variability. The interannual variance of simulated summer temperature accounts for approximately 84-89% of the observed variance depending on the site, indicating that exceptionally hot or cold years are attenuated in the simulations after correction.

3.4.2 Propagation of climate trend biases into HETEROFOR simulations

The results presented in section 3.4.1 show that GFDL-ESM4 (corrected), while overestimating the average summer temperature, is warming significantly more slowly than observed in the IRM data for the period 1961-2024, with a difference in rate of approximately a factor of two. This underestimation of the rate of warming raises a question distinct from that of the level bias already documented: beyond a shift in mean values, does this divergence in climate trends propagate into the trends simulated by HETEROFOR for water stress, NPP and defoliation? And if so, does this propagation follow a relationship proportional to the warming discrepancy, or does it reveal disproportionate responses that may indicate non-linearities specific to certain ecophysiological processes?

Three complementary approaches are employed to examine this question, each addressing a distinct aspect of the issue. The first applies a Mann-Kendall test and calculates Sen's slope across the full 1961-2024 time series, separately for the IRM- and GFDL-ESM4-forced simulations. This approach provides a robust estimate of the overall trend across the entire period. The second divides the period into 20-year blocks, starting in 2024 and moving backwards in time in order to not leave out the most recent years, and calculates a simple linear regression within each block. This approach makes it possible to determine where and when a divergence between the two climate forcings occurs, which is an information that the global trend may mask when the signal is concentrated within a sub-period. The third method calculates, for each indicator, the ratio of its slope to that of the corresponding summer temperature, separately for IRM and GFDL-ESM4. This sensitivity ratio makes it possible to test whether the indicator's response to warming is proportional to the rate of warming of the forcing used, or whether it deviates from it. The Sen slope over the entire period is used as the primary reference rather than a regression against decadal averages, as it uses all 64 available annual values and is consistent with the method used to characterise the climate bias in 3.4.1. A regression on decadal averages is nevertheless used as a supplementary method to verify the robustness of the trends obtained, with its convergence noted where relevant.

When considered over the entire period from 1961 to 2024, a comparison of trend slopes between the IRM- and GFDL-ESM4-forced simulations reveals contrasting patterns depending on the indicator (Figure 22).

For water stress, only one case (Baileux beech) shows significant slopes in both scenarios, with a reduction under GFDL-ESM4. Under LLN, both slopes are zero throughout the entire period, which rules out any detectable trend using this method. Elsewhere (Chimay oak, Baileux oak), the IRM slope reaches higher values (0.45 and 0.23 days/year respectively) without, however, reaching the significance threshold, probably due to interannual variability over the series. These cases cannot therefore be considered at this stage as either confirming or ruling out a real trend.

For the NPP, the majority of cases in which both slopes are statistically significant (Baileux beech, Baileux oak, LLN oak) show an amplification of the trend under GFDL-ESM4 compared with IRM. Two cases show a significant slope on only one side. At Chimay oak, only the GFDL slope is significant (decreasing), while IRM shows no trend. At LLN beech, the IRM shows a significant decreasing trend that GFDL does not replicate. These qualitative differences should be interpreted with caution at this stage, as they are statistically significant on one side only but not on the other.

For defoliation, four cases show significant slopes on both sides (Baileux beech, Baileux oak, LLN oak, LLN beech). In each, the GFDL slope keeps the same sign as the IRM slope (attenuation for the first, amplification for the other two), with no reversal of trend. The remaining case (Chimay oak) is not conclusive over the entire period and is re-examined in the following sections, taking into account time-series analysis and the effect of cavitation.

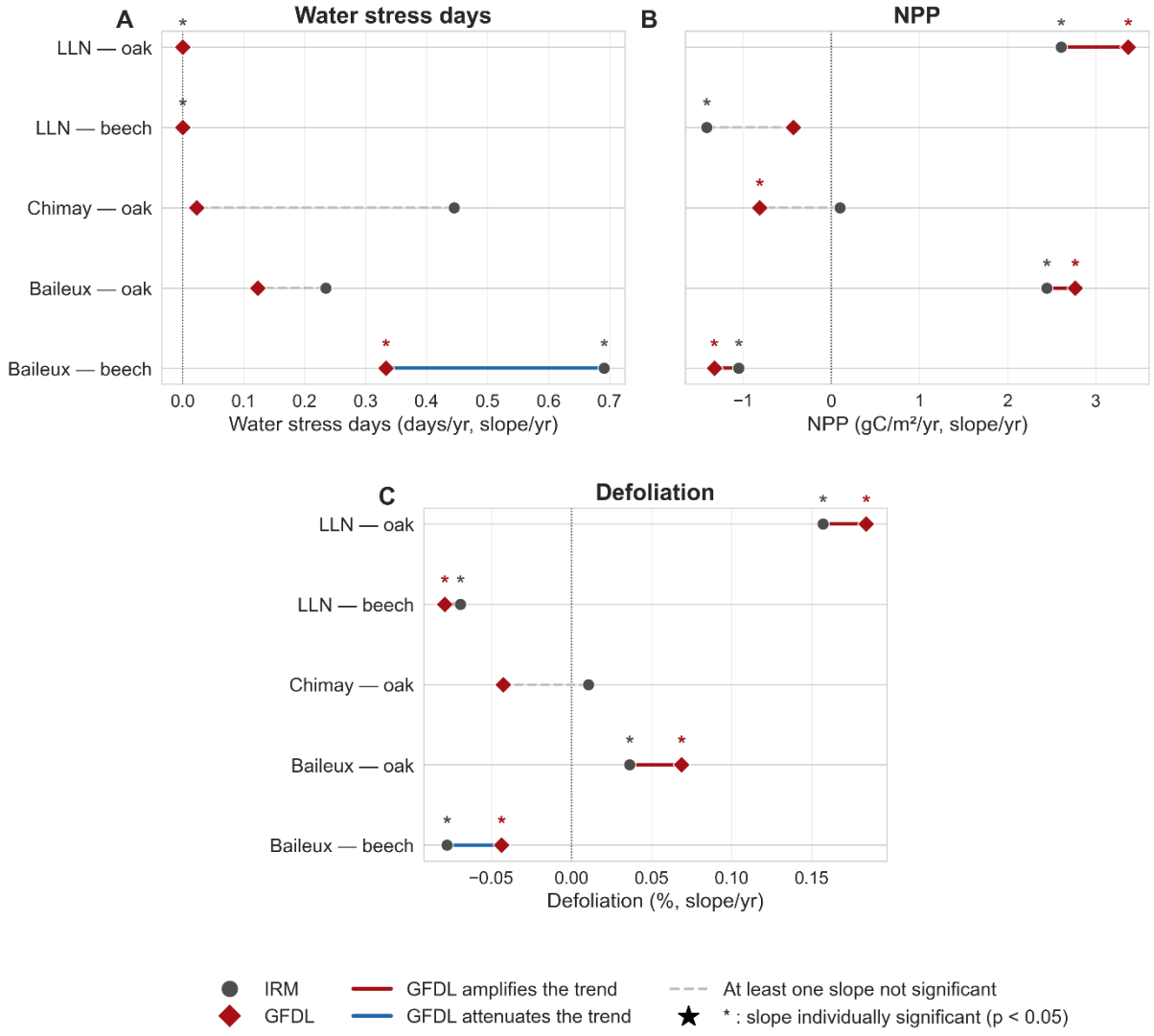

Figure 22. Comparison of trend slopes (1961-2024) between IRM- and GFDL-ESM4-forced simulations, without cavitation, for water stress days (A), NPP (B), and total defoliation (C). For each site × species, the grey point represents the IRM slope and the red diamond the GFDL-ESM4 slope, connected by a segment whose colour indicates whether GFDL-ESM4 amplifies (red) or attenuates (blue) the trend observed under IRM; a dashed grey segment indicates that at least one of the two slopes is not statistically significant ($p \geq 0.05$). An asterisk above a point indicates that the corresponding slope is individually significant ($p < 0.05$), regardless of the other.

While the trend over the entire 1961-2024 period reveals no clear, significant signal of water stress at LLN, splitting the data into 20-year blocks highlights a marked divergence, concentrated in the most

recent block (2005-2024) (Figure 23). As the number of days of stress is a count variable, sensitive to the crossing of a fixed threshold, even a modest variation in water dynamics around this threshold can produce an amplified or misleading signal, without any real underlying change. To verify that the divergence observed above does indeed reflect a genuine hydrological change rather than such an artefact, the same comparison was carried out on the REW itself, on a continuous basis. This analysis confirms the same contrast: a significant decline in the REW under the IRM scenario, which is absent under the GFDL-ESM4 scenario, therefore ruling out the hypothesis of a simple threshold artefact (Appendix G, Table G1). It should be noted, however, that GFDL-ESM4 represents a single run of a single climate model. Over a 20-year period, its internal variability alone could explain the absence of a corresponding trend, and another model or another run of the same model could very well find different results. For the NPP, the analysis by year groups confirms the results obtained over the entire period. A similar analysis by blocks reveals a notable reversal in the sign for defoliation in Chimay oak, subject to the same caveat. All slope and significance values for all sites and indicators are provided in Appendix H.

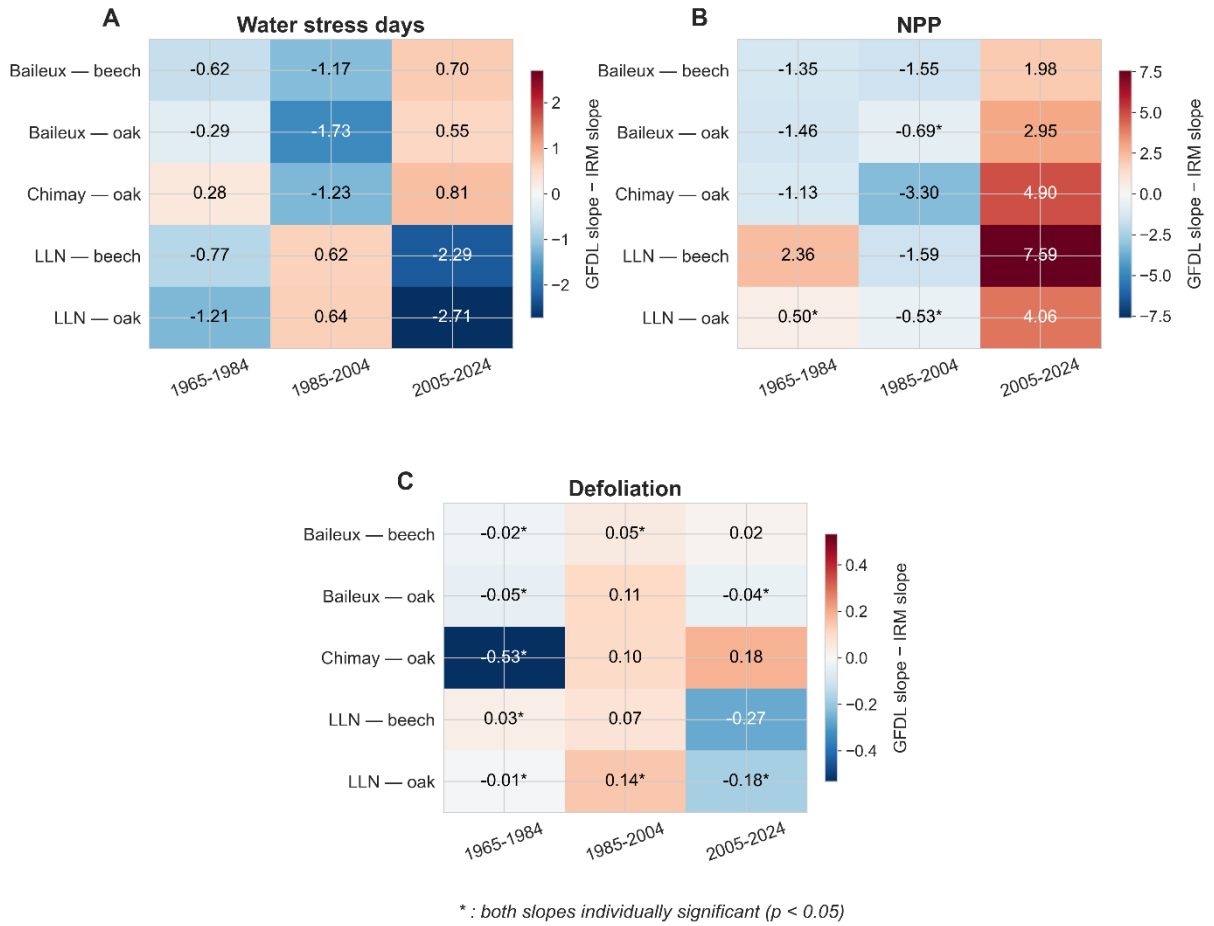

Figure 23 : Slope difference (GFDL-ESM4 − IRM) by 20-year block, without cavitation, for water stress days (A), NPP (B), and total defoliation (C). Blocks are anchored from 2024 backwards in time so as not to truncate the most recent years. Red shades indicate a stronger slope under GFDL-ESM4 than under IRM, blue shades the reverse. An asterisk next to a value indicates that both the IRM and GFDL-ESM4 slopes are statistically significant (p < 0.05) for that block.

For the NPP, the analysis by year groups confirms the results obtained over the entire period.

The most marked discrepancy revealed by this approach concerns defoliation at Chimay oak. In the first block (1965-1984), IRM shows a weak but highly significant upward trend (0.073 %/year, p=0.0001),

while GFDL-ESM4 shows a significant downward trend of a much greater magnitude (-0.460 %/year, p<0.0001). This reversal in sign was not detected by the full-period trend.

In addition to determining whether trends diverge between the two climate forcings, a more nuanced question arises: is this divergence proportional to the rate of warming specific to each forcing, or do certain indicators respond disproportionately? To answer this, the slope of each indicator is plotted against the corresponding summer temperature slope, separately for IRM and GFDL-ESM4 (Figure 24).

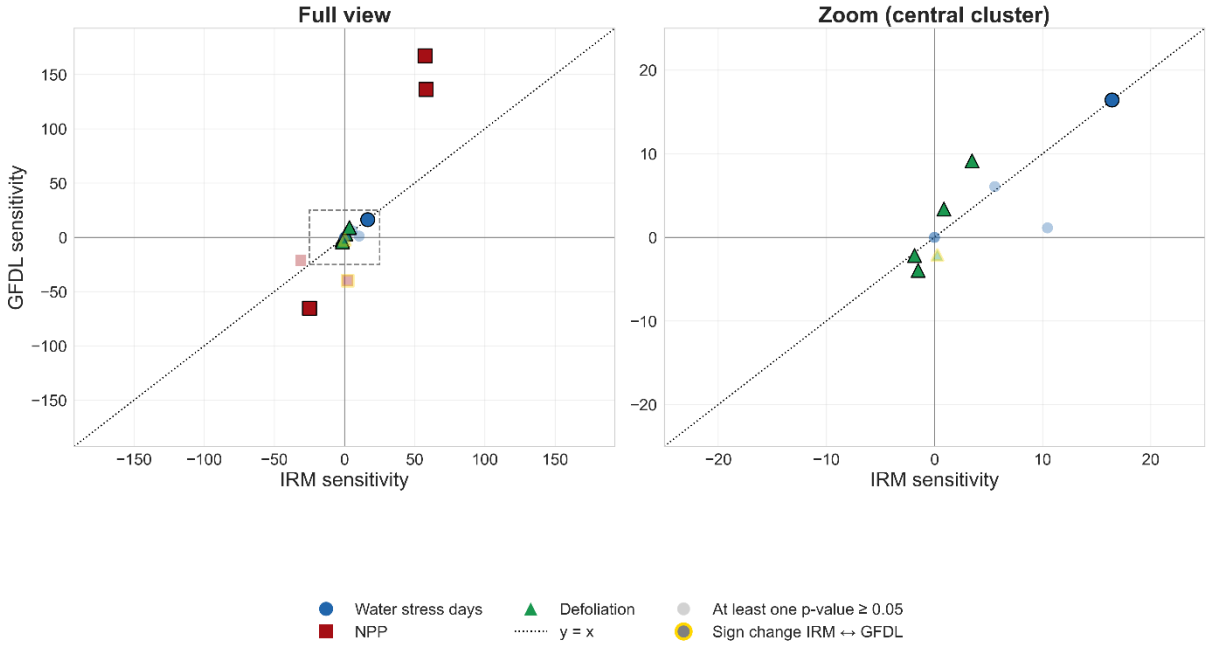

Figure 24 : Sensitivity of each indicator to warming (ratio of the indicator's slope to the corresponding summer temperature slope), compared between IRM and GFDL-ESM4, without cavitation. Each point represents a site × species × indicator combination (circle: water stress days; square: NPP; triangle: total defoliation). The left panel shows the full range of values, the right panel a zoom on the cluster of values near zero (delimited by the dashed box in the left panel). The diagonal (y = x) represents a response perfectly proportional to the rate of warming, identical under both forcings. Filled, black-outlined points correspond to cases where all four quantities involved (slope of the indicator and slope of temperature, for IRM and for GFDL-ESM4) are statistically significant; pale, not outlined points indicate that at least one of these four values is not. A gold outline indicates a sign change in sensitivity between IRM and GFDL-ESM4.

For water stress, the only case in which the four parameters involved (slope of the indicator and slope of temperature, IRM and GFDL) are statistically significant is Baileux beech, where the two sensitivities are virtually identical. The response is therefore proportional to the rate of warming, regardless of the forcing used. An independent verification using regression on decadal averages yields a higher IRM/GFDL sensitivity ratio (19.2 versus 13.0, a factor of ~1.5). However, the GFDL slope no longer reaches the significance threshold (p=0.22), which is an expected consequence of the reduced number of data points (n=6 decades) rather than a disproof of the result obtained with the Mann-Kendall method.

For NPP, the three reliable cases (Baileux beech, Baileux oak, LLN oak) all show a consistently higher sensitivity under GFDL-ESM4 than under IRM, by a consistent factor of 2.3 to 2.9. The response is therefore clearly disproportionate to the rate of warming, with GFDL-ESM4 amplifying the effect.

For defoliation, the four reliable cases show an amplification by a factor of 1.2 to 3.9 depending on the site, placing this indicator between water stress and NPP.

The previous results were obtained with the cavitation module deactivated. These analyses are repeated with the module activated, comparing simulations driven by IRM and GFDL-ESM4 in both cases. All graphs obtained with the cavitation module activated are presented in Appendix I. The general pattern

established above persists: water stress continues to respond in a manner close to proportionality, while NPP and defoliation remain consistently amplified under GFDL-ESM4. The activation of cavitation, however, significantly alters certain individual results in both directions.

At LLN, the comparison with cavitation clearly confirms and reinforces the result already highlighted by the time-series analysis. Results obtained with IRM data shows a strong, significant upward trend in water stress at both plots, which GFDL-ESM4 does not reproduce, driven by the same cluster of severe stress years (2017-2022) already identified above. This result, independently confirmed by the continuous REW analysis (Appendix G, Table G2), validates the robustness of this result at LLN, which has been verified using three different methods. The full comparison across all sites and indicators is shown in Appendix I.

The most pronounced discrepancy identified in the absence of cavitation concerned defoliation at Chimay oak, where the 1965-1984 period showed a change in sign between the IRM (slightly increasing) and the GFDL-ESM4 (markedly decreasing). With cavitation activated on both sides, this divergence disappears almost entirely over the entire period. Both simulations show an almost identical decreasing trend (-0.062% per year for both IRM and GFDL-ESM4, both statistically significant). A decomposition of defoliation into its components directly associated with cavitation and the one associated with competition shows that, at this site, the proportion attributable to cavitation itself is zero, with the entire effect arising from competition.

Conversely, a new discrepancy emerges with cavitation at Baileux beech, where the two simulations had previously agreed (without cavitation) on a decreasing trend in defoliation. With cavitation, the IRM trend becomes zero, while GFDL-ESM4 retains a significant increasing trend. At this site, approximately 55 per cent of total defoliation is directly attributable to cavitation, compared with zero at Chimay oak, suggesting a different mechanism: a direct effect at Baileux beech, rather than an indirect effect via competition.

Cavitation also alters the magnitude of certain discrepancies that were already present without cavitation, without changing their nature. At Baileux beech, the discrepancy in slope between IRM and GFDL-ESM4 for NPP (already significant in both scenarios) increases markedly with cavitation (going from -0.28 to -1.43 $gC/m^2/year$).

Overall, the activation of cavitation does not contradict the contrast observed between indicators, but it does alter several individual results in both directions, exacerbating some discrepancies and resolving others, depending on the site. These variations appear to be linked to the proportion of defoliation directly attributable to cavitation at each site, which itself varies considerably.

3.4.3. Disentangling the effect of temperature level from trend

The previous analysis established that the climate trend bias propagates heterogeneously depending on the indicator, without making it possible to determine whether this propagation results from the level of warming, its rate, or both. To address this issue, a synthetic climate forcing was constructed from the IRM data, to which a constant temperature offset was applied so as to reach the mean level of GFDL-ESM4, while preserving the trend and interannual variability specific to IRM (Appendix J). The two-stage comparison (IRM against IRM+bias, then IRM+bias against GFDL-ESM4) makes it possible to isolate these two effects in turn (Figure 25). The first stage isolates the effect of the temperature level alone, and the second isolates a residual effect that includes the trend among other possible contributing factors (the interannual variance for example).

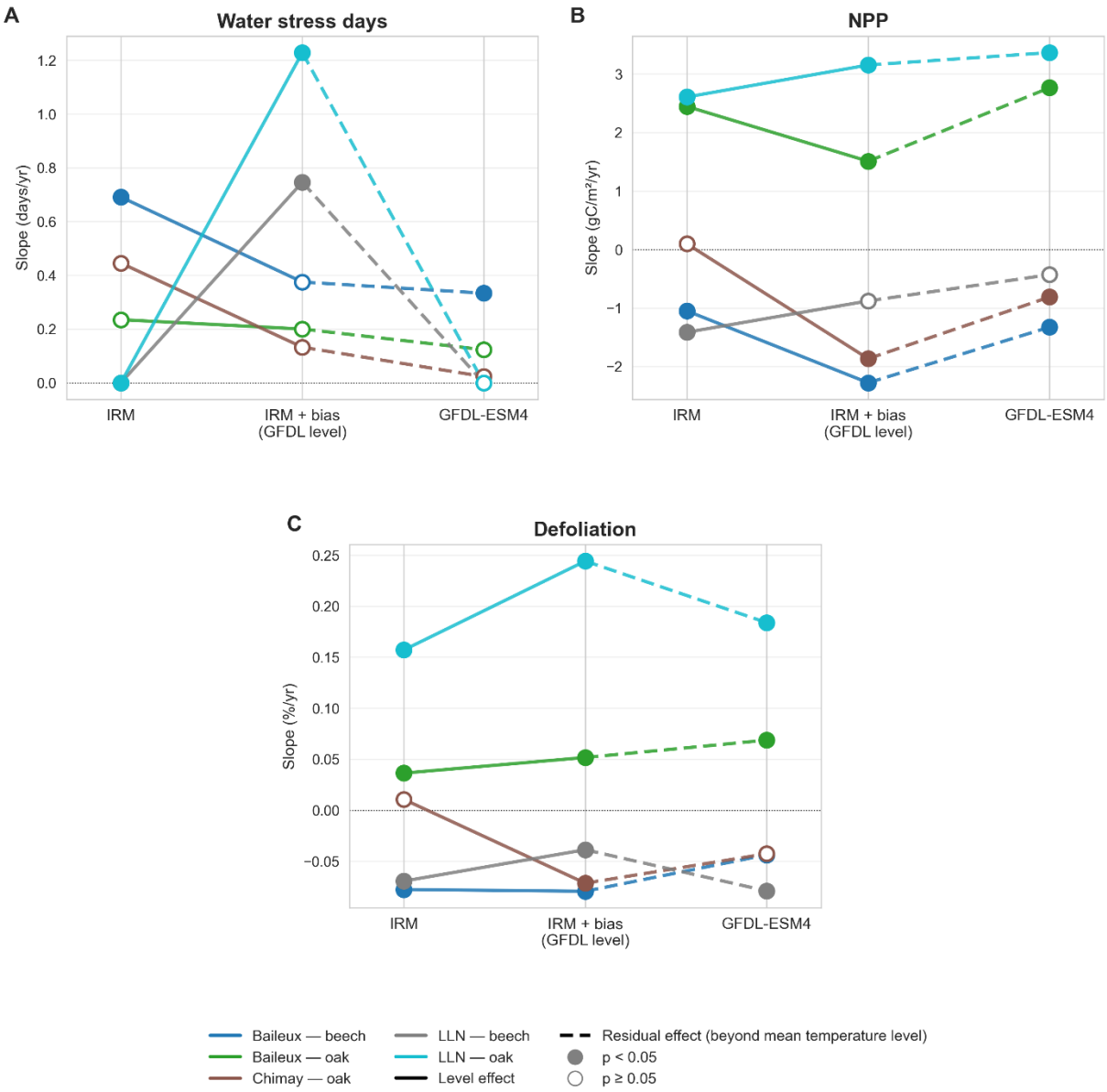

Figure 25 : Trend slope (1961-2024) under three successive climate configurations, without cavitation: IRM (observed climate), IRM+bias (IRM's trend and interannual variability, with mean temperature level adjusted to that of GFDL-ESM4), and GFDL-ESM4, for water stress days (A), NPP (B), and total defoliation (C). The first segment (solid line) isolates the effect of temperature level alone; the second segment (dashed line) isolates a residual effect once this level is equalised, including in particular the climate trend. Each colour represents a site × species combination (see legend). Filled markers indicate a statistically significant slope ($p < 0.05$), open markers a non-significant slope.

In LLN, it is the residual trend, rather than the level, that explains the discrepancy between IRM and GFDL-ESM4 for water stress. The shift in level alone is sufficient to reveal a strong and highly significant trend (IRM+bias: 1.23 days/year for oak, p<0.0001; 0.75 days/year for beech, p=0.0001), whereas it had remained undetectable in the raw IRM time series. GFDL-ESM4, although it now has a comparable temperature level, shows a trend close to zero (0 days/year for both species) and does not reach significance (oak: p=0.455 and beech: p=0.758). As a result, the net difference between IRM and GFDL-ESM4 in raw magnitude is small, since the level and residual effects largely offset one another. The key distinction lies in statistical reliability, with IRM significant at both stages and GFDL-ESM4 never reaching significanceA verification using the continuous relative extractable water reserve (without taking the 0.32 threshold into account) confirms a greater decline under IRM+bias than under IRM, consistent with a hydraulic effect rather than a simple threshold artefact. But the minimum REW

for beech approaches a floor value under IRM+bias, limiting further detectable decline in that specific case (Appendix G, Table G3, Figure G1). However, the resulting increase in stress days appears disproportionately large compared to the underlying hydraulic change. REW itself declines by a factor of roughly two to three under IRM+bias, while the stress-day trend, already significant but of nearly zero magnitude under IRM alone, becomes both large in magnitude and clearly significant under IRM+bias. This is consistent with the sensitivity of threshold-based count variables to changes concentrated near the 0.32 threshold.

In Chimay, by contrast, it is the level that dominates for the NPP. The actual IRM trend is not significant ($p=0.760$), but simply shifting to the GFDL-ESM4 mean level reveals a strong and highly significant downward trend (-1.87 gC/m²/year, $p<0.0001$). This result is indicative of a threshold effect rather than a gradual response to warming, although GFDL-ESM4's own trend (-0.81 gC/m²/year, $p=0.021$) remains somewhat less pronounced than the level-shift alone would predict. Unlike at LLN, however, this compensation is only partial, as GFDL-ESM4's trend stays significant and still differs substantially from IRM's near-zero, non-significant trend. A similar pattern is observed for defoliation at the same site: the IRM trend is not significant ($p=0.085$), while shifting to the GFDL-ESM4 level reveals a significant decreasing trend ($p=0.004$), which GFDL-ESM4 itself does not fully reproduce ($p=0.121$).

In Baileux, this test does not allow a dominant mechanism to be clearly isolated for NPP. The level shift moves the IRM+bias trend away from the one of GFDL-ESM4 at the oak plot, while at the beech plot both stages produce shifts without converging toward GFDL-ESM4's trend either. This indicates that the response at this site cannot be cleanly decomposed into an additive level effect and a separate residual effect, as it could at LLN and Chimay. Level and trend (or interannual variability) likely interact in a more complex way here, although climate forcing remains the only variable differing across the three configurations in this experimental design.

Overall, this test confirms that there is no single mechanism for the propagation of climate bias in the HETEROFOR simulations: depending on the sites and indicators, the divergence in forcings observed in the previous section results sometimes from a threshold effect linked to temperature level, and sometimes from a more direct response to the rate of warming.

This test was also repeated with cavitation enabled (Appendix I). The conclusion for LLN remains unchanged, but the mechanism differs. The trend in water stress is already highly significant under IRM alone (0.91 to 1.06 days/year, $p<0.001$), without requiring the level shift, while GFDL-ESM4 remains flat ($p>0.3$). This result confirms that cavitation amplifies the sensitivity to an already present climatic signal, without being able to compensate for its absence in the GFDL-ESM4 trajectory itself, which does not reproduce the cluster of severe dry years characterising the recent observed period. At Chimay, however, the activation of cavitation complicates the interpretation of the NPP. Unlike the actual, non-significant IRM trend, the IRM trend with cavitation becomes significant, and both the level shift and the residual term contribute significantly, without a single mechanism being clearly identifiable. Overall, the activation of cavitation does not challenge the already established heterogeneity of the mechanisms. Its effect itself varies by site, amplifying an already present climatic signal in some cases (LLN) while altering the nature of the response in others (Chimay).

4. Discussion

The results presented in this study describe the response of five Walloon forest stands to climate change over the period 1961-2100, as simulated by the HETEROFOR model. The following sections discuss these results in four successive stages. First, the model performance (4.1), then the general responses in terms of water stress, productivity and stand structure are compared with the existing literature and the model's performance is assessed (4.1 and 4.2). Second, the mechanisms underlying the projected decline in productivity are examined, with a particular focus on the temperature-NPP regime shift identified in the second half of the 21st century (4.4) and the transformation of the drought regime (4.5). Finally, the biases specific to the climate model used are analysed and their implications for the interpretation of the projections are discussed (4.6), before the main limitations of the study and perspectives for future research are presented (4.7).

4.1 Model performance

The evaluation of HETEROFOR shows contrasted performances depending on the variable under consideration. For soil water dynamics, the correlations between simulated and observed REW are strong across all sites (r = 0.85-0.92), which validates the model's reliability for water stress. These results are consistent with previously published evaluations of the model, which had already demonstrated good performance in terms of water balance, phenology and drainage (Jonard et al., 2020; de Wergifosse et al., 2020). The evaluation conducted here therefore confirms that the simulated hydrological dynamics provide a solid basis for interpreting stress results.

As for growth, the results are more variable. The correlations between simulated and observed circumference increment are reasonable for beech at Baileux (r = 0.64-0.79), but remain very weak for oak at Chimay (r = 0.04-0.24), regardless of the model configuration. The weak correlations observed for oak at Chimay are likely due to a combination of several factors specific to this site. On the one hand, the Chimay oak forest is an old coppice-with-standards, which gives the trees an atypical structure. Its highly developed crowns and thick trunks may mean that the plot is poorly represented by the average allometric relationships used in HETEROFOR for oak. Furthermore, the soil of the Fagnes-Famenne region presents specific pedological constraints that may not be fully captured by a generic parameterisation. Finally, the stand is regularly subjected to attacks by defoliating caterpillars, a biotic disturbance not included in the model which can have significant effects on the trees' radial growth. Furthermore, a systematic positive bias is observed across all plots. Several hypotheses can be put forward, like an underestimation of intra-stand competition, sub-optimal carbon allocation parameters for these sites, the lack of modelling of nutrient limitations, or the biotic disturbances (at least for Chimay's site). This bias must be kept in mind when interpreting future projections, as the absolute values of projected NPP may be affected in the same way.

The validation test against field observations reveals an interesting asymmetry between sites (section 3.1.2). The model under-detects stress days at Baileux oak (sensitivity = 0.753) but over-detects them at Chimay (specificity = 0.759). This latter trend is consistent with the negative bias in the simulated REW, which is more pronounced at Chimay (-0.06 to -0.17) than at Baileux (-0.03 to -0.10). A greater underestimation of soil moisture leads to the stress threshold being crossed more often than observed. This same bias, however, does not explain the under-detection observed at the Baileux oak site, which shows a REW bias of the same order of magnitude as the Baileux beech site (-0.03 to -0.10 in both cases) without the latter showing any comparable asymmetry. The origin of this species difference at Baileux remains unexplained by the data available in this study.

These general responses mask, however, significant contrasts between sites and species, which are examined in section 4.3.

4.2 General responses to climate change: water stress, CO_2 fertilisation and structural inertia

HETEROFOR simulations project a doubling of the number of water-stress days between the historical period and the future period under constant CO_2 levels, with the median increasing from 43 to 107 days per year across all plots. This increase is part of a well-documented trend at the European scale. Using a set of CMIP6 models, Cook et al. (2020) identify Europe and the Mediterranean as among the regions most likely to experience aridification by the end of the 21st century, with a particularly pronounced response in terms of soil moisture. At the Western European scale, Spinoni et al. (2017) demonstrate, based on a set of 11 EURO-CORDEX simulations, a significant increase in the frequency and severity of summer droughts in Belgium and neighboring regions during the 21st century. At the Walloon regional level, projections from the REGE+ project confirm this trend, with an expected decrease in summer precipitation and longer drought episodes (Marchi et al., 2024), consistent with the summer stress simulated here.

While the direction of change is therefore consistent with the literature, the absolute stress values simulated for the future are based on a single climate model and should be interpreted with caution. Part of the projected stress is in fact attributable to biases specific to this model, which will be analysed in section 4.6. The rankings between sites and species nevertheless remain consistent across the two model configurations, which reinforces the reliability of the relative trends regardless of the absolute values.

The simulated increase in NPP under a variable CO_2 regime is considerably high. According to the SSP3-7.0 scenario, in which atmospheric concentration rises from 318 ppm in 1961 to nearly 872 ppm in 2100, the median NPP projected for the future would be 966 gC/m^2/year. This represents a 46% increase compared to the future scenario with a constant CO_2 concentration. This result is consistent with the carbon fertilisation effect documented in temperate forests. Norby (2025), based on a synthesis of four FACE (Free-Air CO_2 Enrichment) experiments in temperate forest stands, report a conserved stimulation of forest NPP of approximately 23% at 550 ppm. This concentration is expected by the middle of the century under SSP3-7.0. The higher response observed here, for a concentration of around 872 ppm in 2100, is therefore not surprising given the non-linear relationship between CO_2 concentration and photosynthetic stimulation.

Beyond productivity, the variable CO_2 scenario also shows a reduction in median water stress compared with the constant CO_2 future (74 vs 107 days/year), consistent with the well-documented effect of high CO_2 on water use efficiency (WUE). When atmospheric CO_2 concentrations rise, trees can maintain the same rate of carbon fixation with their stomata partially closed, as the diffusion gradient of CO_2 towards the carboxylation sites is more favourable. This partial stomatal closure reduces water loss through transpiration without proportionally reducing photosynthesis, thereby improving water-use efficiency (Norby & Zak, 2011). However, this mitigation remains partial. Even under variable CO_2 levels, future stress remains significantly higher than the historical baseline (74 vs 43 days/year), indicating that the WUE effect does not compensate for the intensification of climatic drying documented in this section.

However, these results should be interpreted with caution, as HETEROFOR does not model nutrient co-limitations on the effect of carbon fertilisation. Terrer et al. (2019), based on a meta-analysis of 138 high CO_2 experiments, showed that nitrogen and phosphorus availability is the main factor modulating

biomass response to high CO_2, reducing the overall effect to just 12 ± 3% for a 250 ppm increase. As explicitly acknowledged in the REGE+ project simulations using HETEROFOR (André et al., 2025), the effect of carbon fertilisation is likely to be overestimated in the absence of nutrient cycle modelling. The 46% increase in NPP simulated here should therefore be regarded as an upper bound rather than a realistic estimate, and the variable CO_2 scenario should be interpreted primarily as a sensitivity analysis isolating the potential maximum effect of CO_2 rather than as a projection.

The lack of significant change in volume (from 399 to 420 m^3/ha) and basal area (from 27.3 to 27.9 m^2/ha) between the historical and future periods under constant CO_2 levels is not surprising and is primarily due to the structural inertia of forests. These indicators incorporate decades of accumulated growth and respond to timescales much longer than flux indicators such as NPP. The pronounced autocorrelation of basal area observed in the simulations (coefficients ranging from 0.35 to 0.53) precisely illustrates this slow dynamic. Furthermore, the methodological choice to apply identical silvicultural practices across all scenarios (justified to isolate the climatic effect) also helps to reduce the variance of these indicators between scenarios, by keeping stand densities in comparable ranges. It should also be noted that even when the NPP is affected, as is the case with the cavitation module, basal area and standing volume tend to remain relatively stable, as part of the variation in production is absorbed by timber harvesting. In a scenario where silviculture is kept constant, silvicultural removals partially compensate for productivity fluctuations, limiting their impact on the standing stock. This compensation is confirmed by the volumes harvested. Under constant CO2, the total volume withdrawn over the entire period increases between history and future, from +42% to +96% depending on the plot (+72% on average over the five plots). This marked increase is well above the small change in volume and standing basal area and indicates that most of the productivity gain related to climate change is exported by thinning rather than accumulated in the stand.

However, this result should not be interpreted as an absence of vulnerability. NPP and water stress are, in fact, very significantly affected, and are early signals that precede structural changes. The literature on forest dieback shows that trees can experience prolonged declines in vitality before these translate into measurable losses in volume or basal area (Allen et al., 2010).

4.3 Site and species variability: the role of soil buffering capacity and hydraulic strategies

The simulations reveal marked differences in water stress between sites, mainly associated with local soil properties. Bréda et al. (2006) show that the soil's extractable water reserve acts as a buffer against summer rainfall deficits. The higher it is, the better the soil can maintain a water content above the critical threshold before photosynthesis and transpiration are affected. In Louvain-la-Neuve, the extractable water reserve of the abruptic luvisol (450 mm) is more than twice that of the cambisol in Baileux (178mm), resulting in zero historical stress in LLN (0 days/year for beech) compared with 78 days/year in Baileux. However, this soil buffering capacity is declining in the future. Despite an unchanged water reserve, stress at LLN rises from 0 to 33 days/year for beech, which illustrates the limits of edaphic protection against sufficiently severe climate intensification.

This same useful reserve also limits the ability of the REW-based indicator to detect the physiological deficit that actually occurs at LLN. The correlation between the number of days of stress and the relative transpiration deficit, while being strong at Baileux and Chimay (ρ = 0.83-0.90), is significantly weaker at LLN (ρ = 0.588-0.600). This suggests that part of the physiological deficit at this site is not captured by the REW threshold, which is rarely exceeded. This phenomenon has been documented by Walthert

et al. (2021) with beech, who show that deep soil water reserves in soils with high water-holding capacity prevent the appearance of detectable water stress even during severe droughts. A similar decoupling between soil moisture and the actual stress experienced by vegetation, in a temperate humid forest context, has also been documented on a larger scale (Ahady et al., 2026). The contrast between LLN and the other two sites in terms of days of stress is therefore likely to be both real and partially amplified by a limitation inherent to the REW indicator.

Differences in NPP between sites also reflect the developmental stage of the stands. The stands at Baileux are significantly younger than those at Louvain-la-Neuve and Chimay, which contributes to their higher productivity. Net above-ground primary production generally peaks in young stands and declines with age (Gower et al., 1996). This difference in stage of development therefore adds to climatic and soil factors in explaining the variations in NPP observed between sites.

The simulations also show that oak has significantly higher productivity than beech, with a difference of 56 gC/m²/year at Baileux in the historical scenario, which increases to 120 gC/m²/year in the future. This difference is accompanied by greater water resilience in oak. While the stress-NPP correlations become significantly negative for beech in Baileux (ρ = -0.45) and beech in LLN (ρ = -0.28) in the future, they remain non-significant for oak in Baileux (ρ = -0.12) and in LLN (ρ = -0.16). This result is consistent with the hydraulic parameters assigned to oak in HETEROFOR, which shows higher xylem hydraulic conductivity (25 for oak and 15 for beech). This greater vulnerability of beech to drought is well documented in the literature. Zimmermann et al. (2015), in a dendrochronological analysis comparing Fagus sylvatica with Quercus petraea and three other deciduous species in temperate mixed forests of Central Europe, show that beech is the only species to exhibit an increase in the number of negative pointer years (years of abrupt growth reduction relative to the reference chronology) across all stands, together with a decline in radial increment in the driest stand, since about 1980, in response to increasing summer temperatures and drought intensity, while the other four species show no such response.

One counterintuitive result warrants discussion. The beech plot at Baileux shows a persistent negative correlation between water stress and defoliation, both in the historical period (ρ = -0.32) and the future period (ρ = -0.33), indicating that defoliation decreases as stress increases. It should be noted that this pattern is specific to the configuration without the cavitation module. With the module activated, these correlations disappear or weaken significantly, which would suggest that the module is effective in representing defoliation dynamics. Without the cavitation module, HETEROFOR calculates defoliation only from competition dynamics. Water stress does not directly influence defoliation in this configuration. The hot and more stressful years are also years when solar radiation is more intense and the growing season longer, which can improve the carbon balance of the trees and reduce their defoliation by competition. It is this indirect mechanism that produces the negative correlation observed between stress and defoliation. At the species level, Fagus sylvatica itself shows no significant correlation between temperature and defoliation (ρ = +0.08, $p > 0.05$), while the negative signal at stand level is mainly carried by the oak and spruce present in this mixed stand. With the cavitation module activated, hydraulic defoliation becomes the dominant component (median = 4.97%) and restores the expected positive relationship between water stress and defoliation, which suggests that this module more realistically represents defoliation dynamics under high water stress.

This mechanism also underlies the counterintuitive result observed at Chimay oak, where the cavitation module produces the opposite effect. The decrease in defoliation at Chimay oak when the cavitation module is activated (from 9.8% to 3.3%) is explained by a reduction in competition-driven defoliation, which decreases from 8.25% to 2.37%. Cavitation-driven defoliation remains zero at this site, indicating

that the module does not generate hydraulic stress intense enough to cause direct leaf loss. The activation of the cavitation module appears to improve the carbon balance of the stand. This is possibly through higher stomatal conductance and increased NPP, thereby reducing the competition-induced defoliation. This effect is primarily observed in Carpinus betulus (from 9.09% to 2.73%), while Quercus petraea is only marginally affected (-0.42%).

4.4 Temperature-NPP regime shift

The simulations reveal a marked shift in the relationship between summer temperature and NPP between the historical and future periods. During the historical period, temperature has a positive and significant effect on oak NPP (+39 gC/m²/year per standard deviation, $p<0.001$), reflecting conditions in which higher temperatures stimulate photosynthesis and extend the growing season. In contrast, its effect is already negative for beech during this same period (-31 gC/m²/year, $p<0.05$). This is consistent with the already high historical stress level at Baileux (~78 days/year), which makes the hottest years already unfavourable. In the future, this effect becomes negative for both species (beech: -34 gC/m²/year; oak: -35 gC/m²/year), reflecting a regime shift in which temperature stops to be a stimulating factor and becomes a limiting factor. This finding is consistent with the empirical observations of Tijerín-Triviño et al. (2025), who, using forest inventories from Spain and Sweden, show that the effect of temperature anomalies on forest productivity was positive or zero during an initial period (their study period begins in 1980), before becoming significantly negative in recent years. This gradual shift is attributed to intensifying warming and associated water stress. This convergence, however, concerns the direction of the phenomenon, but the timing differs. Their transition is already observed in the last decades, whereas the shift identified here is only complete for both species in the simulated future period. For beech, however, the negative effect is already present from the historical period, where stress is already high (Baileux). The divergence in overall timing can come from the geographical area, because their study focuses on Spain and Sweden. Finally, an underestimation of the warming by GFDL-ESM4 could also contribute to the remaining lag.

The analysis by stress class provides a mechanistic explanation for this shift. When the years are grouped into three classes according to their level of water stress, the temperature-NPP relationship is positive and often significant under low stress for the majority of plots, notably for the Baileux oak ($\rho = +0.67$), the LLN oak ($\rho = +0.63$) and the Chimay oak ($\rho = +0.40$). This relationship gradually weakens with increasing stress, eventually reversing under high stress for the Chimay oak ($\rho = -0.51$) and the Baileux beech ($\rho = -0.31$). This pattern suggests that it is the interaction between temperature and water stress that governs the shift, and not temperature alone. Multiple regression confirms this finding. The temperature × stress interaction term is negative and significant for both species and both periods, and constitutes the most consistent result of this analysis. This indicates that the combined effect of heat and stress is consistently negative for productivity, regardless of the period considered. The mechanistic interpretation is that under low stress, higher temperatures favour photosynthesis and extend the growing season. But beyond a certain threshold of water deficit, these same temperatures intensify atmospheric evapotranspiration, force stomatal closure and reduce net photosynthetic capacity, cancelling out or even reversing their beneficial effect.

Time-series analysis enables us to identify the physiological mechanism underlying the decline in NPP observed in the second half of the 21st century. While NPP peaks around 2055-2060 before gradually declining, gross primary productivity (GPP) continues to increase throughout the simulated period. At the same time, the leaf area index (LAI) remains stable (~5.0-5.4 m²/m²), indicating that the decline in NPP is not associated with a generalised loss of leaf area. These findings suggest that the decline in NPP

is not driven by a reduction in gross photosynthesis, which continues to increase throughout the century, but rather by an increase in autotrophic maintenance respiration, which would absorb an increasing proportion of the fixed carbon as temperatures rise. This hypothesis is consistent with the thermal sensitivity of plant respiration (Atkin & Tjoelker, 2003). The respiration rate increases almost exponentially with temperature, with a Q10 (the factor by which respiration increases for every 10°C rise) generally estimated at around 2 under moderate temperatures. In the context of continued warming up to 2100, this increasing respiratory cost could gradually counterbalance the additional photosynthetic gains and reduce the proportion of gross carbon actually allocated to biomass.

This temporal evolution reveals a trend structured into three distinct phases. During the historical period, NPP increases gradually, rising from around 630 to 710 gC/m²/year, reflecting a positive trend consistent with the beneficial effects of moderate warming on photosynthesis and the lengthening of the growing season. This trend continues until reaching a peak (~760 gC/m²/year), before giving way to a gradual decline that brings the NPP down to 665 gC/m²/year by the end of the century, eliminating most of the gains accumulated during the 20th century. This trajectory reflects the constant-CO_2 configuration under the SSP3-7.0 scenario used in this study. The exclusion of CO_2 fertilisation and the choice of emission pathway both influence this timing, and a scenario including CO_2 fertilisation or a less severe emission pathway would likely shift or attenuate this tipping point.

This three-phase trajectory is consistent with projections from independent forest models. In their study by Sperlich et al. (2020) on beech and fir in Germany, they tested both a configuration with activated carbon fertilization and a configuration with constant CO_2, directly comparable to the one used here. With carbon fertilization, the tipping point is different in each emission scenario: 2040 for RCP2.6, 2045 for RCP4.5, and 2060 for RCP8.5. Under constant CO_2, however, the compensatory mechanism of CO_2 disappears and the tipping point occurs as early as 2035, almost independently of the climate scenario, followed by a much more marked decline (-30 to -104% compared to a scenario without climate change). This discrepancy highlights that while the three-phase structure (initial gain, shift, decline) seems to be a robust response of temperate forests to climate change, the precise timing of the shift remains highly dependent on the model, site and assumption used for CO_2. This discrepancy probably reflects both a site difference and a methodological difference between the two studies. The maximum soil water holding capacity at the site studied by Sperlich et al. (119 mm for beech, 115 mm for fir) is significantly lower than in any of the plots studied here (178 to 450 mm). Their site is therefore more likely to reach the critical threshold of water stress under the effect of warming.

Similarly, Tumajer et al. (2025), using 2013 tree-ring chronologies from Central and South-Eastern Europe, project stable or slightly increased growth until the 2040s-2050s, followed by a significant decline under high-emission scenarios in the second half of the century. The convergence of these three independent approaches, which include this process-based simulation at sites in Wallonia, a biogeochemical model for a German forest, and a large-scale European wood formation model, reinforces the robustness of this temporal trajectory as a characteristic response of temperate forests to climate change under a high-emission scenario.

The temporal trends reveal marked contrasts between species and between sites. The Baileux oak and the LLN oak are distinguished by a remarkably stable NPP throughout the entire future period, despite ongoing warming, which is consistent with the greater hydraulic resilience of the oak documented in section 4.2. In contrast, the Chimay oak shows the most pronounced decline, with NPP falling from around 720 to 550 gC/m²/year between 2060 and 2100, and is the only plot where GPP itself declines by the end of the century. As discussed earlier, Chimay is a site with particularly challenging soil conditions. This makes the site more vulnerable beyond a certain climatic threshold, to the extent that

future conditions there will exceed not only the net carbon allocation capacity but also the gross photosynthetic capacity.

The beech at LLN exhibits an atypical profile. Its NPP shows high interannual variability and a weak temporal trend, with a slightly negative historical correlation between temperature and NPP ($\rho = -0.30$), whereas the oaks at the same site show positive historical correlations. This unexpected behaviour for a site that has historically experienced little stress cannot be easily explained by the model parameters and needs further analysis. The atypical profile of this plot is likely related to its historically very low stress levels. With no water deficit during the historical period, neither temperature nor water availability acts as a clear limiting factor for productivity at this site. Under these conditions, interannual NPP variability is probably driven by other factors such as radiation or intra-stand competition dynamics. This would explain both the weak correlations across all stress classes and the absence of a clear temporal trend for this stand

These results have direct implications for the anticipation of climate risks on Walloon forests. The projected peak of NPP around 2055-2060, followed by a gradual decline, suggests that a few decades' window still separates the current conditions from the regime shift documented here. The exact timing of this changeover remains uncertain, however, notably due to the biases specific to the climate model used, whose effects on the timing of projections will be discussed in section 4.5.

The temporal dynamics of NPP documented here are inseparable from changes in the structure of drought episodes, which are examined in detail in the following section.

4.5 From episodic to chronic drought: implications for forest vulnerability

The simulations reveal not only an increase in the total number of days of water stress, but also a shift in the temporal pattern of this stress during the growing season. Historically, stress has been concentrated between May and September, with peaks in August and September. In the future, it will extend from April to October, thereby reducing the recovery window between consecutive episodes and increasing the risk of cumulative stress over the entire season. This seasonal extension is consistent with the projections of Spinoni et al. (2017), who anticipate an increase in the frequency of spring and summer droughts in Western Europe during the 21st century. However, the most significant consequence of this transformation is not so much the intensification of individual episodes than the shift from a pattern of episodic stress to one of chronic stress. In Baileux, interannual stress variability is halved in the future. The interquartile range, falling from 51 to 25 days for beech and from 52 to 23 days for oak, indicates that stress is no longer an exceptional event but is becoming a more permanent condition during the growing season.

The analysis of drought episodes reveals three contrasting patterns across sites, reflecting distinct trajectories of vulnerability. In Baileux, the change is mainly manifested by a lengthening of episodes: the median duration increases from 41 to 117 days for beech and from 40 to 119 days for oak, while the number of episodes remains stable. This shift towards very long episodes illustrates a transition to a regime of chronic stress, in which summer drought is no longer interrupted by sufficient recovery periods. In Chimay, the change is intermediate: duration increases moderately (from 22 to 42 days), but the number of episodes rises sharply, reflecting an intensification in frequency rather than duration. LLN shows the most marked contrast in terms of frequency. Episodes, which have historically been very rare (16 for beech and 17 for oak over 63 years), are set to increase dramatically in the future (88 and 81 respectively), while remaining of moderate duration (17-22 days). Although individual episodes remain short, their increasing frequency progressively reduces the forest's ability to recover between events.

These structural differences in the pattern of drought episodes have a measurable impact on annual productivity. The annual maximum duration of episodes shows significant negative correlations with NPP at Baileux beech (ρ = -0.44, future only), Chimay oak (ρ = -0.33 historical, -0.47 future) and LLN beech (ρ = -0.72 historical). The strengthening of this relationship between historical and future periods at Baileux beech and Chimay oak is consistent with the hypothesis that a critical duration threshold will be exceeded more frequently in the future, beyond which the duration of the episode becomes a limiting factor for productivity.

Beyond changes in the pattern of extreme events, climate change is also modifying the impact of extreme years. Despite the overall increase in NPP under future conditions, a dry year in the future still remains less productive than a normal year from the historical period. The loss in NPP associated with dry years also intensifies over time. The Chimay oak shows the most severe change, with the relative loss in NPP during dry years increasing from -3.9% to -15.2% between the historical and future periods.

One particularly revealing finding concerns the beech at LLN, which shows an apparent reduction in the relative loss of NPP during extreme years, falling from -20.3% to -10.1%. At first sight, this might suggest an improvement in the resilience of this site. In reality, this result is explained by the way in which extreme years are defined. What constituted an extremely dry year in the past has become an ordinary year in the future. Future normal years are themselves much more stressful than historically, which reduces the contrast between the 'normal' and 'extreme' categories. It is therefore not that LLN is becoming more resilient to extreme droughts, but that the baseline has shifted upwards, making all years more challenging.

The extent to which these projections reflect real future conditions depends, however, on the quality of the climate model used to force the simulations, which is the subject of the following section.

4.6 Climate model biases and their implications for projections

4.6.1. Separating climate change from climate source

All comparisons between the historical period and the future period presented in sections 3.1 to 3.3 of this thesis contrast a simulation forced by observed IRM data (1961-2024) with a simulation forced by the GFDL-ESM4 climate model, corrected using the ISIMIP3 method (2025-2100). This choice was based on the following reasoning: to use data as close as possible to reality for the historical period, and to assume that a properly calibrated climate model would provide a sufficiently reliable approximation of that same reality for the future period, for which no observations exist. Section 3.4 shows that this implicit assumption does not hold true.

This design effectively combines two sources of difference into a single signal: the actual climate change between the two periods, and the systematic difference between the two climate sources themselves, which is independent of any climate change. This second source of difference would exist even in the absence of any actual climate change, simply because the GFDL-ESM4 differs structurally from the IRM.

Section 3.4 does not correct this design issue retrospectively, but it does provide a direct estimate of it. By comparing IRM and GFDL-ESM4 over the same historical period, it eliminates the primary source of difference. Any observed discrepancy therefore reflects solely the difference between the two climate sources themselves, site by site and indicator by indicator. This approach is consistent with the approach used by Jourdan et al. (2021): comparing the outputs of an impact model driven by modelled climate

data with those obtained using observed data over a common historical period, before attributing credibility to predictions for a future period.

This estimate remains, however, incomplete. The bias quantified in 3.4.1 itself changes over time, and its extrapolation to 2100 is based on an assumption of stationarity that could only be verified over a much shorter time window than the horizon of the future projections.

This limitation is not unique to this thesis. The performance assessment presented in the REGE+ report (2025), from which the climate data used here are derived, indicates that correcting for temperature bias using quantile mapping, an additive method or scaling reduces the average bias by only around 62-63 per cent, leaving a significant residual after correction. The residual observed here (+0.92 to +2.32°C depending on the site) remains, nevertheless, of considerable magnitude.

A second limitation, distinct from the previous one, concerns the temporal extrapolation of the correction. The ISIMIP3 correction is calibrated over the period 1976-2014. Section 3.4.1 has already shown that outside this window, a residual systematic bias emerges (+0.6 to +1.0°C prior to 1976, +0.2 to +0.5°C after 2014). This is consistent with the fact that bias correction methods implicitly assume the stability of the correction function over time, an assumption that does not always hold, particularly for summer temperature (Maraun, 2012). The future projections used in this thesis extend to 2100, which is 86 years beyond the end of the calibration window. The bias estimate presented in 3.4.1 and its propagation documented in 3.4.2 and 3.4.3 therefore provide a solid basis for the period tested, but their extrapolation to the year 2100 relies on an assumption of stationarity that could not be verified.

4.6.2. The structural limits of trend correction in ISIMIP3

The level bias documented in 3.4.1 is not an anomaly in the ISIMIP3 correction, but a direct consequence of the way it is designed. Quantile mapping does not guarantee that the climate trend of the raw model will be preserved, as the correction depends on the position of each value within the distribution rather than its temporal position (Cannon et al., 2015). To overcome this limitation regarding temperature, ISIMIP3 removes the trend from the time series before applying the quantile correction, then restores the trend specific to the raw climate model once the correction has been applied (André et al., 2025; Lange, 2019). This design has a direct implication for this thesis: the correction deliberately preserves the warming trend specific to GFDL-ESM4, regardless of its accuracy relative to the actually observed trend. The under-warming documented in 3.4.1 (approximately half the rate observed by the IRM) is therefore not corrected by design, as this is not the purpose of the correction.

4.6.3. Heterogeneous propagation mechanisms across sites and indicators

The level and trend test presented in 3.4.3 confirms that no single mechanism dominates the divergence between IRM and GFDL-ESM4. At LLN, the difference remaining once mean levels have been equalised between the two forcing scenarios, which notably includes the trend, accounts for most of the divergence in water stress. The simple shift in mean level is sufficient to reveal a strong and highly significant trend, which is absent in the IRM data, while GFDL-ESM4, despite now having a comparable mean level, does not reproduce this trend. At Chimay, by contrast, it is the level that dominates for NPP and defoliation. The trend under IRM is not significant, but the shift towards the mean level of GFDL-ESM4 alone is sufficient to reveal a significant trend, which GFDL-ESM4 itself reproduces only partially. This signature is indicative of a threshold effect rather than a gradual response to warming. Finally, at Baileux, the test does not allow a dominant mechanism for NPP to be identified. The shift in

level does not systematically bring the obtained trend closer to that of GFDL-ESM4, suggesting that level and trend (or interannual variability) interact here in a more complex manner than a simple additive decomposition, with climate forcing nevertheless remaining the only variable distinguishing the three tested configurations.

This heterogeneity may be related to the nature of the processes involved in each indicator, although this has not been directly tested in this study. Water stress depends on a relatively direct soil water balance, while NPP results from a cascade of physiological processes (radiation interception, photosynthesis, respiration, carbon allocation) which may amplify an initial climate error as it propagates through these successive stages (Jourdan et al., 2021). Defoliation, on the other hand, is not calculated independently of the climate. In HETEROFOR, it is initiated when the NPP, which has already been calculated, becomes insufficient to sustain the foliage. It therefore inherits any error already present in that NPP. However, this hypothesis remains to be confirmed. It is consistent with the non-proportional amplification observed for NPP, but this study does not establish the precise mechanism.

This lack of a single mechanism has a direct implication : no single correction factor can be applied to all sites and indicators to adjust future projections retrospectively. Correcting for the level alone would work for LLN but would leave Chimay largely unexplained, and the reverse would not work either. The appropriate correction depends on the site and the indicator in question, which limits the possibility of a simple, overall correction to the results presented in sections 3.1 to 3.3.

The discrepancy between the IRM and GFDL-ESM4 models at LLN, identified by the block analysis (3.4.2) and confirmed by the level and trend test (3.4.3), is driven by a cluster of particularly dry years concentrated between 2017 and 2022. This period corresponds to a well-documented multi-year drought episode at the European scale. Rakovec et al. (2022) show that the 2018-2020 drought sequence in Europe reached an intensity unprecedented over the last 250 years, with a peak temperature anomaly of +2.8 degrees. The fact that GFDL-ESM4, even after its mean level has been adjusted to match that of IRM, does not reproduce the upward trend in stress observed under IRM at LLN over this period is consistent with the finding already established in 3.4.2. Over a 20-year window, the internal variability of a single climate run alone may be sufficient to explain the absence of a trend that another run, or another model, might have reproduced.

4.6.4. Implications for the interpretation of future projections

The biases documented in this section do not affect the projections presented in the results uniformly, and their probable direction can be estimated on a site-by-site basis, provided that the mechanisms identified over the historical period continue in the same proportions until 2100. It should be noted that the level biases summarised below (+2.32°C at Baileux, +1.50°C at Chimay, +0.92°C at LLN) are averages over the entire 1961-2024 period. The decreasing trend in the bias documented in 3.4.1 implies that it is lower in the most recent decade than over the entire period, although it has not been completely eliminated. At Baileux beech, where stress responds proportionally to warming, the simulated future water stress is likely to be overestimated in absolute terms if this mechanism persists. At Chimay, where the level offset (+1.50°C) accounts for a significant, but not the entire, portion of the observed downward trend under GFDL-ESM4 for NPP and defoliation, the same reasoning suggests a partial rather than a total overestimation of this decline. At LLN, by contrast, where the level bias is the lowest of the three sites (+0.92°C) and where the trend difference dominates rather than the level, GFDL-ESM4 does not reproduce the acceleration in stress shown by IRM over the recent period. Future stress is therefore more likely to be underestimated there. The under-warming documented in 3.4.1 also introduces uncertainty

regarding the timing of the temperature-NPP regime shift identified in 4.3. The trend bias, if it persists, would tend to delay this shift in the simulation compared with reality, while the level bias would, conversely, tend to bring it forward, as the simulation starts from a temperature that is already over-estimated. These two effects act in opposite directions, and it is not possible to determine which one dominates on the basis of this study.

These findings remain qualitative. This study does not allow for a precise quantification of the extent of these over- or underestimations, and no single correction factor can be applied to all sites and indicators. Comparisons between species within the same site, which are based on a strictly identical climatic forcing, are probably more robust to this bias than comparisons between sites themselves, where the difference might be partially confounded with differences in bias between sites.

4.7 Limitations and research perspectives

Several limitations of the HETEROFOR model are worth noting. Firstly, HETEROFOR does not model the effect of water stress on phenology, notably on bud break and leaf senescence, whereas empirical studies show that drought can change these dates and in turn affect the length of the growing season and the productivity (de Wergifosse et al., 2020). Secondly, the nutrient cycling module remains incomplete. Nitrogen and phosphorus are not dynamically simulated, leading to a likely overestimation of the carbon fertilization effect, as discussed in section 4.2. Thirdly, the cavitation module, although promising, has only recently been added to the model and has not yet been formally evaluated, which justified the use of the model without this module as a reference configuration in this study.

Furthermore, the assessment of the water stress indicator presented in section 3.1.2 has two specific limitations. Firstly, the relative transpiration deficit indicator, unlike the count of stress days based on the REW, could not be validated against independent field observations, due to the lack of available sap flow or transpiration measurements at the study sites. Its agreement with the reference indicator therefore reflects only internal consistency within the model, not external validation. Secondly, the choice of threshold and of the REW indicator was made a priori, based on the calibration described in section in the methodology, and was then confirmed a posteriori by the comparisons presented in section 3.1.2, rather than through an a priori selection from among several candidate indicators.

Beyond the model itself, several methodological choices limit the scope of the conclusions. The main limitation is the use of a single climate model (GFDL-ESM4) and emission scenario (SSP3-7.0). The inter-model uncertainty in the CMIP6 projections is considerable for Europe, and the results obtained here, notably the timing of the NPP-temperature changeover documented in section 4.3, could vary significantly depending on the climate model used. The exploration of other scenarios would also help to assess how far an ambitious mitigation path could avoid or delay this shift. Moreover, the study is limited to five hardwood plots spread over three Walloon sites. Although these sites represent the main bioclimatic zones of Wallonia, coniferous stands, which occupy a significant part of the Walloon forest territory, are not represented, which limits the generalization of the conclusions to all Walloon forests. It should also be noted that to isolate the effect of the species from that of the soil, the same pedological profile was used for both plots of the same site, which constitutes a simplification compared to the reality on the ground. Finally, forestry has been kept constant between scenarios in order to isolate the climate effect, which does not reflect the silvicultural adaptations that could be implemented in response to the projections documented here.

A main limitation of this thesis concerns the combination of two distinct climate data sources for the historical and future periods, with IRM observations and bias-corrected GFDL-ESM4 simulations. As

discussed in section 4.6, this design introduces a residual bias between the two periods that is independent of any actual climate change, which complicates the interpretation of the comparisons between past and future.

Furthermore, most comparisons presented in this study contrast the historical and future periods as two aggregated blocks rather than describing the continuous trajectory between them. Except where time-series or sub-period analyses were specifically conducted (sections 3.3.3 and 3.4.2), this approach does not capture how and when indicators evolve within each period, and could mask non-linear dynamics such as the temperature-NPP regime shift itself.

These limitations lead to several research perspectives. A multi-model and multi-scenario approach would better constrain the uncertainty around the timing and magnitude of the productivity shift documented here. It is also important to extend the simulations to Walloon coniferous stands, in particular for species such as Norway spruce or Douglas fir whose vulnerability to water stress is documented but not quantified in this framework. From the forest management point of view, the results of this study have practical implications for the adaptation of the Walloon forests. The higher hydraulic resilience of oak to increasing water stress, reported in section 4.3, indicates that promoting this species in future silviculture, particularly on poorly buffered soils, is a relevant adaptation pathway. This recommendation is embedded in a broader framework. Recent studies reveal that intrinsic species resistance is the dominant factor of drought-induced mortality risk (Decarsin et al., 2024), and that species diversification significantly reduces the variability of survival under stress conditions, with mixed stands suffering on average 20% less damage than monocultures (Blondeel et al., 2024). These projections therefore suggest a progressive diversification of species in Walloon forests, combining species with contrasting hydraulic strategies, and an adaptation of silvicultural practices before the regime shift documented in section 4.4 is reached.

Conclusion

Temperate European forests are facing an acceleration of climate change whose trajectory exceeds what current climate models are able to reproduce faithfully. In this context, the quantification of impacts at the plot scale, taking into account the diversity of soils, species and forest structures of Wallonia, is an essential foundation for any forest adaptation strategy. This work attempted to address this need by simulating, using the HETEROFOR model, the response of five Walloon stands dominated by common beech and sessile oak to a climate change scenario covering the period 1961-2100.

Before interpreting the simulations' results, the validity of the model was established on two types of variables. Water dynamics are well reproduced at all sites, which provides a solid basis for the results related to water stress. The growth performance is more variable, especially at Chimay, where the atypical structure of the stand and the absence of biotic disturbances in the model limit the representativeness of the simulations. A systematic positive bias in simulated growth suggests that the absolute values of NPP should be interpreted with caution, without questioning the consistency of trends and relative comparisons between sites and species. Moreover, the analysis of the biases of the GFDL-ESM4 climate model reveals a paradoxical situation. This model overestimates absolute temperatures while underestimating the rate of recent warming. These two biases act in opposite directions on forest projections, one tends to overestimate future stress, the other to delay it. It is therefore not possible to conclude that the projections presented are systematically pessimistic or optimistic, but only that they are affected by an uncertainty that depends on the indicator and the time horizon considered.

The simulations reveal a profound transformation of the climatic conditions to which the Walloon forests will face by 2100. The median water stress doubles between the historical period and the future, and its episodic nature gradually gives way to chronic stress that reduces the recovery window of trees between episodes. This transition manifests itself differently depending on the site. In Baileux, it is the lengthening of the episodes that dominates, while in Louvain-la-Neuve, whose soil historically had a large buffer capacity, it is the multiplication of their frequency. In both cases, the result is an increasing and more permanent pressure on trees, whose consequences for productivity increase with time.

One of the most striking results of this work is that productivity’s response to these new conditions follows a three-phase trajectory. After a moderate increase during the historical period, the average NPP peaks around 2055-2060 before gradually declining, to the point of erasing, by 2100, almost all the gains accumulated during the 20th century. This switch reflects a reversal of the role of temperature: a stimulating factor under past conditions, it becomes a limiting factor as soon as it is combined with a water deficit intense enough to force stomatal closure and amplify respiratory costs. This trajectory, consistent with independent projections from other European forest models, highlights that the window of opportunity to act on forest composition and structure is limited in time.

The contrasts between species directly shed light on the available levers for adaptation. Sessile oak, with superior xylem hydraulic conductivity and greater stress tolerance, maintains remarkably stable productivity throughout the future period in most sites, whereas the common beech sees its relationship to temperature reverse as early as the historical period on the most stressed sites. This difference in hydraulic strategy between the two species, consistent with the ecophysiological literature, results in a growing productivity gap by 2100. It suggests that promoting sessile oak, especially on soils with low water reserves, represents a relevant adaptation path for Walloon forest managers, if this forestry transition is initiated before the chronic stress regime documented here is fully installed.

This work has several limitations that define its scope and open research perspectives. The use of a single climate model and a single emission scenario does not make it possible to constrain the uncertainty about the precise moment of the productivity shift, which could be advanced or delayed depending on the actual trajectory of warming. The absence of other species like coniferous stands, which represent a significant fraction of the Walloon forests, limits the generalization of the conclusions. The integration of adaptive silvicultural scenarios in future work would be a decisive step towards translating the results of this study into operational recommendations for Walloon forest managers.

References

Ahady, A. B., Wolf, S., & Klopries, E.-M. (2026). Identifying soil moisture thresholds for agricultural drought sensitivity through coupling modeled and satellite data in a humid temperate catchment. *Ecological Indicators*, *186*, 114875. https://doi.org/10.1016/j.ecolind.2026.114875

Allen, C. D., Macalady, A. K., Chenchouni, H., Bachelet, D., McDowell, N., Vennetier, M., Kitzberger, T., Rigling, A., Breshears, D. D., Hogg, E. H. (Ted), Gonzalez, P., Fensham, R., Zhang, Z., Castro, J., Demidova, N., Lim, J.-H., Allard, G., Running, S. W., Semerci, A., & Cobb, N. (2010). A global overview of drought and heat-induced tree mortality reveals emerging climate change risks for forests. *Forest Ecology and Management, Adaptation of Forests and Forest Management to Changing Climate*, *259*(4), 660–684. https://doi.org/10.1016/j.foreco.2009.09.001

André, F., Candaele, R., Pau, M., Marchi, S., & Hosseinzadehtalaei, P. (2025). *Forest regeneration under climate and environmental changes—REGE +*.

André, F., de Wergifosse, L., de Coligny, F., Beudez, N., Ligot, G., Gauthray-Guyénet, V., Courbaud, B., & Jonard, M. (2021). Radiative transfer modeling in structurally complex stands: Towards a better understanding of parametrization. *Annals of Forest Science*, *78*(4), 92. https://doi.org/10.1007/s13595-021-01106-8

Aranda, I., Gil, L., & Pardos, J. A. (2005). Seasonal changes in apparent hydraulic conductance and their implications for water use of European beech (Fagus sylvatica L.) and sessile oak [Quercus petraea (Matt.) Liebl] in South Europe. *Plant Ecology*, *179*(2), 155–167. https://doi.org/10.1007/s11258-004-7007-1

Atkin, O. K., & Tjoelker, M. G. (2003). Thermal acclimation and the dynamic response of plant respiration to temperature. *Trends in Plant Science*, *8*(7), 343–351. https://doi.org/10.1016/S1360-1385(03)00136-5

Blondeel, H., Guillemot, J., Martin-StPaul, N., Druel, A., Bilodeau-Gauthier, S., Bauhus, J., Grossiord, C., Hector, A., Jactel, H., Jensen, J., Messier, C., Muys, B., Serrano-León, H., Auge, H., Barsoum, N., Birhane, E., Bruelheide, H., Cavender-Bares, J., Chu, C., … Baeten, L. (2024). Tree diversity reduces variability in sapling survival under drought. *Journal of Ecology*, *112*(5), 1164–1180. https://doi.org/10.1111/1365-2745.14294

Bosela, M., Merganičová, K., Torresan, C., Cherubini, P., Fabrika, M., Heinze, B., Höhn, M., Kašanin-Grubin, M., Klopčič, M., Mészáros, I., Pach, M., Střelcová, K., Temperli, C., Tonon, G., Pretzsch, H., & Tognetti, R. (2022). Modelling Future Growth of Mountain Forests Under Changing Environments. In R. Tognetti, M. Smith, & P. Panzacchi (Eds), *Climate-Smart Forestry in Mountain Regions* (pp. 223–262). Springer International Publishing. https://doi.org/10.1007/978-3-030-80767-2_7

Bréda, N., Huc, R., Granier, A., & Dreyer, E. (2006). Temperate forest trees and stands under severe drought: A review of ecophysiological responses, adaptation processes and long-term consequences. *Annals of Forest Science*, *63*(6), 625–644. https://doi.org/10.1051/forest:2006042

Bugmann, H., & Seidl, R. (2022). The evolution, complexity and diversity of models of long-term forest dynamics. *Journal of Ecology*, *110*. https://doi.org/10.1111/1365-2745.13989

C3S/ECMWF & WMO. (2026). *C3S-WMO European State of the Climate 2025*. https://doi.org/10.24381/zy93-sb27

Caloiero, T., Caloiero, P., & Frustaci, F. (2018). Long-term precipitation trend analysis in Europe and in the Mediterranean basin. *Water and Environment Journal*, *32*(3), 433–445. https://doi.org/10.1111/wej.12346

Campioli, M., Vincke, C., Jonard, M., Kint, V., Demarée, G., & Ponette, Q. (2017). Current status and predicted impact of climate change on forest production and biogeochemistry in the temperate oceanic European zone: Review and prospects for Belgium as a case study. *Journal of Forest Research*, *17*, 1–18. https://doi.org/10.1007/s10310-011-0255-8

Cannon, A. J., Sobie, S. R., & Murdock, T. Q. (2015). Bias Correction of GCM Precipitation by Quantile Mapping: How Well Do Methods Preserve Changes in Quantiles and Extremes? *Journal of Climate*, *28*(17), 6938–6959. https://doi.org/10.1175/JCLI-D-14-00754.1

Cardell, M. F., Amengual, A., Romero, R., & Ramis, C. (2020). Future extremes of temperature and precipitation in Europe derived from a combination of dynamical and statistical approaches. *International Journal of Climatology*, *40*(11), 4800–4827. https://doi.org/10.1002/joc.6490

Carvalho-Oliveira, J., Spuler, F. R., & Kretschmer, M. (2026). Targeted weather regimes identify circulation patterns behind Western European summer heat extremes and trends. *Environmental Research Letters*, *21*(5), 054014. https://doi.org/10.1088/1748-9326/ae499b

Cook, B. I., Mankin, J. S., Marvel, K., Williams, A. P., Smerdon, J. E., & Anchukaitis, K. J. (2020). Twenty-First Century Drought Projections in the CMIP6 Forcing Scenarios. *Earth's Future*, *8*(6), e2019EF001461. https://doi.org/10.1029/2019EF001461

Courbaud, B., de Coligny, F., & Cordonnier, T. (2003). Simulating radiation distribution in a heterogeneous Norway spruce forest on a slope. *Agricultural and Forest Meteorology*, *116*(1), 1–18. https://doi.org/10.1016/S0168-1923(02)00254-X

de Wergifosse, L., André, F., Beudez, N., de Coligny, F., Goosse, H., Jonard, F., Ponette, Q., Titeux, H., Vincke, C., & Jonard, M. (2020). HETEROFOR 1.0: A spatially explicit model for exploring the response of structurally complex forests to uncertain future conditions – Part 2: Phenology and water cycle. *Geoscientific Model Development*, *13*(3), 1459–1498. https://doi.org/10.5194/gmd-13-1459-2020

Decarsin, R., Guillemot, J., le Maire, G., Blondeel, H., Meredieu, C., Achard, E., Bonal, D., Cochard, H., Corso, D., Delzon, S., Doucet, Z., Druel, A., Grossiord, C., Torres-Ruiz, J. M., Bauhus, J., Godbold, D. L., Hajek, P., Jactel, H., Jensen, J., … Martin-StPaul, N. (2024). Tree drought–mortality risk depends more on intrinsic species resistance than on stand species diversity. *Global Change Biology*, *30*(9), e17503. https://doi.org/10.1111/gcb.17503

Deser, C., & Phillips, A. S. (2023). A range of outcomes: The combined effects of internal variability and anthropogenic forcing on regional climate trends over Europe. *Nonlinear Processes in Geophysics*, *30*(1), 63–84. https://doi.org/10.5194/npg-30-63-2023

Dong, B., & Sutton, R. T. (2025). Drivers and mechanisms contributing to excess warming in Europe during recent decades. *Npj Climate and Atmospheric Science*, *8*(1), 41. https://doi.org/10.1038/s41612-025-00930-3

Dong, B., Sutton, R. T., Shaffrey, L., & Harvey, B. (2022). Recent decadal weakening of the summer Eurasian westerly jet attributable to anthropogenic aerosol emissions. *Nature Communications*, *13*(1), 1148. https://doi.org/10.1038/s41467-022-28816-5

Douville, H., Roehrig, R., & Nabat, P. (2025). Contribution of large-scale atmospheric circulation and anthropogenic aerosols to recent summer warming over western Europe. *Climate Dynamics*, *63*(5), 208. https://doi.org/10.1007/s00382-025-07689-6

Farooqi, T., Li, X., Yu, Z., Liu, S., & Sun, O. (2020). Reconciliation of research on forest carbon sequestration and water conservation. *Journal of Forestry Research*, *32*. https://doi.org/10.1007/s11676-020-01138-2

Gilson, L. W., Eskelson, B. N. I., & Sattler, D. F. (2025). What makes a forest growth model climate-sensitive? An examination of statistical and silvicultural model needs under climate change. *Forestry: An International Journal of Forest Research*, *98*(5), 649–660. https://doi.org/10.1093/forestry/cpaf020

Glantz, P., Fawole, O. G., Ström, J., Wild, M., & Noone, K. J. (2022). Unmasking the Effects of Aerosols on Greenhouse Warming Over Europe. *Journal of Geophysical Research: Atmospheres*, *127*(22), e2021JD035889. https://doi.org/10.1029/2021JD035889

Gower, S. T., McMurtrie, R. E., & Murty, D. (1996). Aboveground net primary production decline with stand age: Potential causes. *Trends in Ecology & Evolution*, *11*(9), 378–382. https://doi.org/10.1016/0169-5347(96)10042-2

Granier, A., Bréda, N., Biron, P., & Villette, S. (1999). A lumped water balance model to evaluate duration and intensity of drought constraints in forest stands. *Ecological Modelling*, *116*(2), 269–283. https://doi.org/10.1016/S0304-3800(98)00205-1

Hanel, M., Rakovec, O., Markonis, Y., Máca, P., Samaniego, L., Kyselý, J., & Kumar, R. (2018). Revisiting the recent European droughts from a long-term perspective. *Scientific Reports*, *8*(1), 9499. https://doi.org/10.1038/s41598-018-27464-4

Hansen, J. E., Sato, M., Simons, L., Nazarenko, L. S., Sangha, I., Kharecha, P., Zachos, J. C., Von Schuckmann, K., Loeb, N. G., Osman, M. B., Jin, Q., Tselioudis, G., Jeong, E., Lacis, A., Ruedy, R., Russell, G., Cao, J., & Li, J. (2023). Global warming in the pipeline. *Oxford Open Climate Change*, *3*(1), kgad008. https://doi.org/10.1093/oxfclm/kgad008

Harrison, P. A., Berry, P. M., Simpson, G., Haslett, J. R., Blicharska, M., Bucur, M., Dunford, R., Egoh, B., Garcia-Llorente, M., Geamănă, N., Geertsema, W., Lommelen, E., Meiresonne, L., & Turkelboom, F. (2014). Linkages between biodiversity attributes and ecosystem services: A systematic review. *Ecosystem Services*, *9*, 191–203. https://doi.org/10.1016/j.ecoser.2014.05.006

Held, & Soden. (2006). *Robust Responses of the Hydrological Cycle to Global Warming in: Journal of Climate Volume 19 Issue 21 (2006)*. https://journals.ametsoc.org/view/journals/clim/19/21/jcli3990.1.xml

Jonard, M., André, F., de Coligny, F., de Wergifosse, L., Beudez, N., Davi, H., Ligot, G., Ponette, Q., & Vincke, C. (2020). HETEROFOR 1.0: A spatially explicit model for exploring the response of structurally complex forests to uncertain future conditions – Part 1: Carbon fluxes and tree dimensional growth. *Geoscientific Model Development*, *13*(3), 905–935. https://doi.org/10.5194/gmd-13-905-2020

Jourdan, M., François, C., Delpierre, N., St-Paul, N. M., & Dufrêne, E. (2021). Reliable predictions of forest ecosystem functioning require flawless climate forcings. *Agricultural and Forest Meteorology*, *311*, 108703. https://doi.org/10.1016/j.agrformet.2021.108703

Knutzen, F., Averbeck, P., Barrasso, C., Bouwer, L. M., Gardiner, B., Grünzweig, J. M., Hänel, S., Haustein, K., Johannessen, M. R., Kollet, S., Müller, M. M., Pietikäinen, J.-P., Pietras-Couffignal, K.,

Pinto, J. G., Rechid, D., Rousi, E., Russo, A., Suarez-Gutierrez, L., Veit, S., … Gliksman, D. (2025). Impacts on and damage to European forests from the 2018–2022 heat and drought events. *Natural Hazards and Earth System Sciences*, *25*(1), 77–117. https://doi.org/10.5194/nhess-25-77-2025

Landis, J. R., & Koch, G. G. (1977). The measurement of observer agreement for categorical data. *Biometrics*, *33*(1), 159–174.

Lange, S. (2019). Trend-preserving bias adjustment and statistical downscaling with ISIMIP3BASD (v1.0). *Geoscientific Model Development Discussions*, 1–24. https://doi.org/10.5194/gmd-2019-36

Lévesque, M., Siegwolf, R., Saurer, M., Eilmann, B., & Rigling, A. (2014). Increased water-use efficiency does not lead to enhanced tree growth under xeric and mesic conditions. *New Phytologist*, *203*(1), 94–109. https://doi.org/10.1111/nph.12772

Li, H., Li, Z., Chen, Y., Xiang, Y., Liu, Y., Kayumba, P. M., & Li, X. (2021). Drylands face potential threat of robust drought in the CMIP6 SSPs scenarios. *Environmental Research Letters*, *16*(11), 114004. https://doi.org/10.1088/1748-9326/ac2bce

Lindner, M., Fitzgerald, J. B., Zimmermann, N. E., Reyer, C., Delzon, S., van der Maaten, E., Schelhaas, M.-J., Lasch, P., Eggers, J., van der Maaten-Theunissen, M., Suckow, F., Psomas, A., Poulter, B., & Hanewinkel, M. (2014). Climate change and European forests: What do we know, what are the uncertainties, and what are the implications for forest management? *Journal of Environmental Management*, *146*, 69–83. https://doi.org/10.1016/j.jenvman.2014.07.030

Lindner, M., Maroschek, M., Netherer, S., Kremer, A., Barbati, A., Garcia-Gonzalo, J., Seidl, R., Delzon, S., Corona, P., Kolström, M., Lexer, M. J., & Marchetti, M. (2010). Climate change impacts, adaptive capacity, and vulnerability of European forest ecosystems. *Forest Ecology and Management, Adaptation of Forests and Forest Management to Changing Climate*, *259*(4), 698–709. https://doi.org/10.1016/j.foreco.2009.09.023

Manning, C., Widmann, M., Bevacqua, E., Van Loon, A. F., Maraun, D., & Vrac, M. (2019). Increased probability of compound long-duration dry and hot events in Europe during summer (1950–2013). *Environmental Research Letters*, *14*(9), 094006. https://doi.org/10.1088/1748-9326/ab23bf

Maraun, D. (2012). Nonstationarities of regional climate model biases in European seasonal mean temperature and precipitation sums. *Geophysical Research Letters*, *39*(6). https://doi.org/10.1029/2012GL051210

Marchi, S., Jonard, M., Goosse, H., André, F., & Ghilain, N. (2024). *QUEL CLIMAT FUTUR POUR NOS FORÊTS ?*

Martinez del Castillo, E., Zang, C. S., Buras, A., Hacket-Pain, A., Esper, J., Serrano-Notivoli, R., Hartl, C., Weigel, R., Klesse, S., Resco de Dios, V., Scharnweber, T., Dorado-Liñán, I., van der Maaten-Theunissen, M., van der Maaten, E., Jump, A., Mikac, S., Banzragch, B.-E., Beck, W., Cavin, L., … de Luis, M. (2022). Climate-change-driven growth decline of European beech forests. *Communications Biology*, *5*(1), 163. https://doi.org/10.1038/s42003-022-03107-3

Masson-Delmotte, V., Zhai, P., Pirani, A., Connors, S. L., Péan, C., Berger, S., Caud, N., Chen, Y., Goldfarb, L., Gomis, M. I., Huang, M., Leitzell, K., Lonnoy, E., Matthews, J. B. R., Maycock, T. K., Waterfield, T., Yelekçi, Ö., Yu, R., & Zhou, B. (Eds). (2021). Summary for policymakers. In *Climate Change 2021: The Physical Science Basis. Contribution of Working Group I to the Sixth Assessment*

Report of the Intergovernmental Panel on Climate Change (pp. 3–32). Cambridge University Press. https://doi.org/10.1017/9781009157896.001

Meinshausen, M., Nicholls, Z. R. J., Lewis, J., Gidden, M. J., Vogel, E., Freund, M., Beyerle, U., Gessner, C., Nauels, A., Bauer, N., Canadell, J. G., Daniel, J. S., John, A., Krummel, P. B., Luderer, G., Meinshausen, N., Montzka, S. A., Rayner, P. J., Reimann, S., … Wang, R. H. J. (2020). The shared socio-economic pathway (SSP) greenhouse gas concentrations and their extensions to 2500. *Geoscientific Model Development*, *13*(8), 3571–3605. https://doi.org/10.5194/gmd-13-3571-2020

Menzel, A., Yuan, Y., Matiu, M., Sparks, T., Scheifinger, H., Gehrig, R., & Estrella, N. (2020). Climate change fingerprints in recent European plant phenology. *Global Change Biology*, *26*(4), 2599–2612. https://doi.org/10.1111/gcb.15000

Nolander, C., & Lundmark, R. (2024). A Review of Forest Ecosystem Services and Their Spatial Value Characteristics. *Forests*, *15*, 919. https://doi.org/10.3390/f15060919

Norby, R. J. (2025). Forest productivity response to elevated CO2 in free-air CO2 enrichment experiments: The 23 percent solution, revisited. *New Phytologist*, *246*(5), 1952–1959. https://doi.org/10.1111/nph.70162

Norby, R. J., & Zak, D. R. (2011). Ecological Lessons from Free-Air CO2 Enrichment (FACE) Experiments. *Annual Review of Ecology, Evolution, and Systematics*, *42*(Volume 42, 2011), 181–203. https://doi.org/10.1146/annurev-ecolsys-102209-144647

Paligi, S. S., Hackmann, C. A., Schick, J., Audisio, M., Coners, H., Mund, M., Ammer, C., & Leuschner, C. (2025). Isohydric Douglas fir shows earlier drought-induced declines in stem water status and growth than anisohydric beech. *Agricultural and Forest Meteorology*, *388*, 111294. https://doi.org/10.1016/j.agrformet.2026.111294

Pan, Y., Birdsey, R. A., Phillips, O. L., Houghton, R. A., Fang, J., Kauppi, P. E., Keith, H., Kurz, W. A., Ito, A., Lewis, S. L., Nabuurs, G.-J., Shvidenko, A., Hashimoto, S., Lerink, B., Schepaschenko, D., Castanho, A., & Murdiyarso, D. (2024). The enduring world forest carbon sink. *Nature*, *631*(8021), 563–569. https://doi.org/10.1038/s41586-024-07602-x

Penuelas, J., Canadell, J., & Ogaya, R. (2011). Increased water-use efficiency during the 20th century did not translate into enhanced tree growth. *Global Ecology and Biogeography*, *20*, 597–608. https://doi.org/10.1111/j.1466-8238.2010.00608.x

Porté, A., & Bartelink, H. H. (2002). Modelling mixed forest growth: A review of models for forest management. *Ecological Modelling*, *150*(1), 141–188. https://doi.org/10.1016/S0304-3800(01)00476-8

Rakovec, O., Samaniego, L., Hari, V., Markonis, Y., Moravec, V., Thober, S., Hanel, M., & Kumar, R. (2022). The 2018–2020 Multi-Year Drought Sets a New Benchmark in Europe. *Earth's Future*, *10*(3), e2021EF002394. https://doi.org/10.1029/2021EF002394

Rantanen, M., Karpechko, A. Y., Lipponen, A., Nordling, K., Hyvärinen, O., Ruosteenoja, K., Vihma, T., & Laaksonen, A. (2022). The Arctic has warmed nearly four times faster than the globe since 1979. *Communications Earth & Environment*, *3*(1), 168. https://doi.org/10.1038/s43247-022-00498-3

Reyer, C., Lasch-Born, P., Suckow, F., Gutsch, M., Murawski, A., & Pilz, T. (2014). Projections of regional changes in forest net primary productivity for different tree species in Europe driven by climate change and carbon dioxide. *Annals of Forest Science*, *71*(2), 211–225. https://doi.org/10.1007/s13595-013-0306-8

River discharge | Copernicus. (n.d.). Retrieved 28 May 2026, from https://climate.copernicus.eu/esotc/2022/river-discharge

Ryan, M. G., Binkley, D., & Fownes, J. H. (1997). Age-Related Decline in Forest Productivity: Pattern and Process. In M. Begon & A. H. Fitter (Eds), *Advances in Ecological Research* (Vol. 27, pp. 213–262). Academic Press. https://doi.org/10.1016/S0065-2504(08)60009-4

Saintonge, F.-X., Gillette, M., Blaser, S., Queloz, V., & Leroy, Q. (2021). Situation et gestion de la crise liée aux scolytes de l'Épicéa commun fin 2021 dans l'est de la France, en Suisse et en Wallonie. *Revue forestière française*, *73*(6), 619–641. https://doi.org/10.20870/revforfr.2021.7201

Samaniego, L., Thober, S., Kumar, R., Wanders, N., Rakovec, O., Pan, M., Zink, M., Sheffield, J., Wood, E. F., & Marx, A. (2018). Anthropogenic warming exacerbates European soil moisture droughts. *Nature Climate Change*, *8*(5), 421–426. https://doi.org/10.1038/s41558-018-0138-5

Schumacher, D. L., Zachariah, M., Otto, F., Barnes, C., Philip, S., Kew, S., Vahlberg, M., Singh, R., Heinrich, D., Arrighi, J., van Aalst, M., Hauser, M., Hirschi, M., Bessenbacher, V., Gudmundsson, L., Beaudoing, H. K., Rodell, M., Li, S., Yang, W., … Seneviratne, S. I. (2024). Detecting the human fingerprint in the summer 2022 western–central European soil drought. *Earth System Dynamics*, *15*(1), 131–154. https://doi.org/10.5194/esd-15-131-2024

Schumacher, D., Singh, J., Hauser, M., Fischer, E., Wild, M., & Seneviratne, S. (2024). Exacerbated summer European warming not captured by climate models neglecting long-term aerosol changes. *Communications Earth & Environment*, *5*. https://doi.org/10.1038/s43247-024-01332-8

Senf, C., Buras, A., Zang, C. S., Rammig, A., & Seidl, R. (2020). Excess forest mortality is consistently linked to drought across Europe. *Nature Communications*, *11*(1), 6200. https://doi.org/10.1038/s41467-020-19924-1

Senf, C., Pflugmacher, D., Zhiqiang, Y., Sebald, J., Knorn, J., Neumann, M., Hostert, P., & Seidl, R. (2018). Canopy mortality has doubled in Europe's temperate forests over the last three decades. *Nature Communications*, *9*(1), 4978. https://doi.org/10.1038/s41467-018-07539-6

Speich, M. J. R. (2019). Quantifying and modeling water availability in temperate forests: A review of drought and aridity indices. *iForest - Biogeosciences and Forestry*, *12*(1), 1. (world). https://doi.org/10.3832/ifor2934-011

Sperlich, D., Nadal-Sala, D., Gracia, C., Kreuzwieser, J., Hanewinkel, M., & Yousefpour, R. (2020). Gains or Losses in Forest Productivity under Climate Change? The Uncertainty of CO2 Fertilization and Climate Effects. *Climate*, *8*(12), 141. https://doi.org/10.3390/cli8120141

Spinoni, J., Vogt, J. V., Naumann, G., Barbosa, P., & Dosio, A. (2018). Will drought events become more frequent and severe in Europe? *International Journal of Climatology*, *38*(4), 1718–1736. https://doi.org/10.1002/joc.5291

Terrer, C., Jackson, R. B., Prentice, I. C., Keenan, T. F., Kaiser, C., Vicca, S., Fisher, J. B., Reich, P. B., Stocker, B. D., Hungate, B. A., Peñuelas, J., McCallum, I., Soudzilovskaia, N. A., Cernusak, L. A., Talhelm, A. F., Van Sundert, K., Piao, S., Newton, P. C. D., Hovenden, M. J., … Franklin, O. (2019). Nitrogen and phosphorus constrain the CO2 fertilization of global plant biomass. *Nature Climate Change*, *9*(9), 684–689. https://doi.org/10.1038/s41558-019-0545-2

Tijerín-Triviño, J., Lines, E. R., Zavala, M. A., García, M., Astigarraga, J., Cruz-Alonso, V., Dahlgren, J., & Ruiz-Benito, P. (2025). Forest Productivity Decreases in Response to Recent Changes in Vegetation

Structure and Climate in the Latitudinal Extremes of the European Continent. *Global Ecology and Biogeography*, *34*(2), e70011. https://doi.org/10.1111/geb.70011

Tumajer, J., Kašpar, J., Altman, J., Altmanová, N., Camarero, J. J., Cienciala, E., Čada, V., Čihák, T., Doležal, J., Fibich, P., Janda, P., Kaczka, R., Kolář, T., Lehejček, J., Mašek, J., Matula, R., Neudertová Hellebrandová, K., Plavcová, L., Rybníček, M., … Treml, V. (2025). Longer growing seasons will not offset growth loss in drought-prone temperate forests of Central-Southeast Europe. *Nature Communications*, *16*(1), 9535. https://doi.org/10.1038/s41467-025-64568-8

Twardosz, R., Walanus, A., & Guzik, I. (2021). Warming in Europe: Recent Trends in Annual and Seasonal temperatures. *Pure and Applied Geophysics*, *178*(10), 4021–4032. https://doi.org/10.1007/s00024-021-02860-6

Van der Perre, R., Bythell, S., Bogaert, P., Claessens, H., Ridremont, F., Tricot, C., Vincke, C., & Ponette, Q. (2015). La carte bioclimatique de Wallonie: Un nouveau découpage écologique du territoire pour le choix des essences forestières. *Forêt.Nature*, *135*, 47–58.

Walthert, L., Ganthaler, A., Mayr, S., Saurer, M., Waldner, P., Walser, M., Zweifel, R., & von Arx, G. (2021). From the comfort zone to crown dieback: Sequence of physiological stress thresholds in mature European beech trees across progressive drought. *Science of The Total Environment*, *753*, 141792. https://doi.org/10.1016/j.scitotenv.2020.141792

Wang, F., Shao, W., Yu, H., Kan, G., He, X., Zhang, D., Ren, M., & Wang, G. (2020). Re-evaluation of the Power of the Mann-Kendall Test for Detecting Monotonic Trends in Hydrometeorological Time Series. *Frontiers in Earth Science*, *8*. https://doi.org/10.3389/feart.2020.00014

Weynants, M., Vereecken, H., & Javaux, M. (2009). Revisiting Vereecken Pedotransfer Functions: Introducing a Closed-Form Hydraulic Model. *Vadose Zone Journal*, *8*, 86–95. https://doi.org/10.2136/vzj2008.0062

Xu, N., Wang, T., Wang, Y., Dong, J., & Bao, W. (2025). Photosynthetic Responses of Forests to Elevated CO2: A Cross-Scale Constraint Framework and a Roadmap for a Multi-Stressor World. *Biology*, *14*(11), 1534. https://doi.org/10.3390/biology14111534

Yin, Z., Dong, B., Wei, W., & Yang, S. (2024). Anthropogenic Impacts on Amplified Midlatitude European Summer Warming and Rapid Increase of Heatwaves in Recent Decades. *Geophysical Research Letters*, *51*(16), e2024GL108982. https://doi.org/10.1029/2024GL108982

Zhan, C., Orth, R., Yang, H., Reichstein, M., Zaehle, S., De Kauwe, M. G., Rammig, A., & Winkler, A. J. (2024). Estimating the CO2 Fertilization Effect on Extratropical Forest Productivity From Flux-Tower Observations. *Journal of Geophysical Research: Biogeosciences*, *129*(6), e2023JG007910. https://doi.org/10.1029/2023JG007910

Zimmermann, J., Hauck, M., Dulamsuren, C., & Leuschner, C. (2015). Climate Warming-Related Growth Decline Affects Fagus sylvatica, But Not Other Broad-Leaved Tree Species in Central European Mixed Forests. *Ecosystems*, *18*(4), 560–572. https://doi.org/10.1007/s10021-015-9849-x

Appendices

Appendix A :

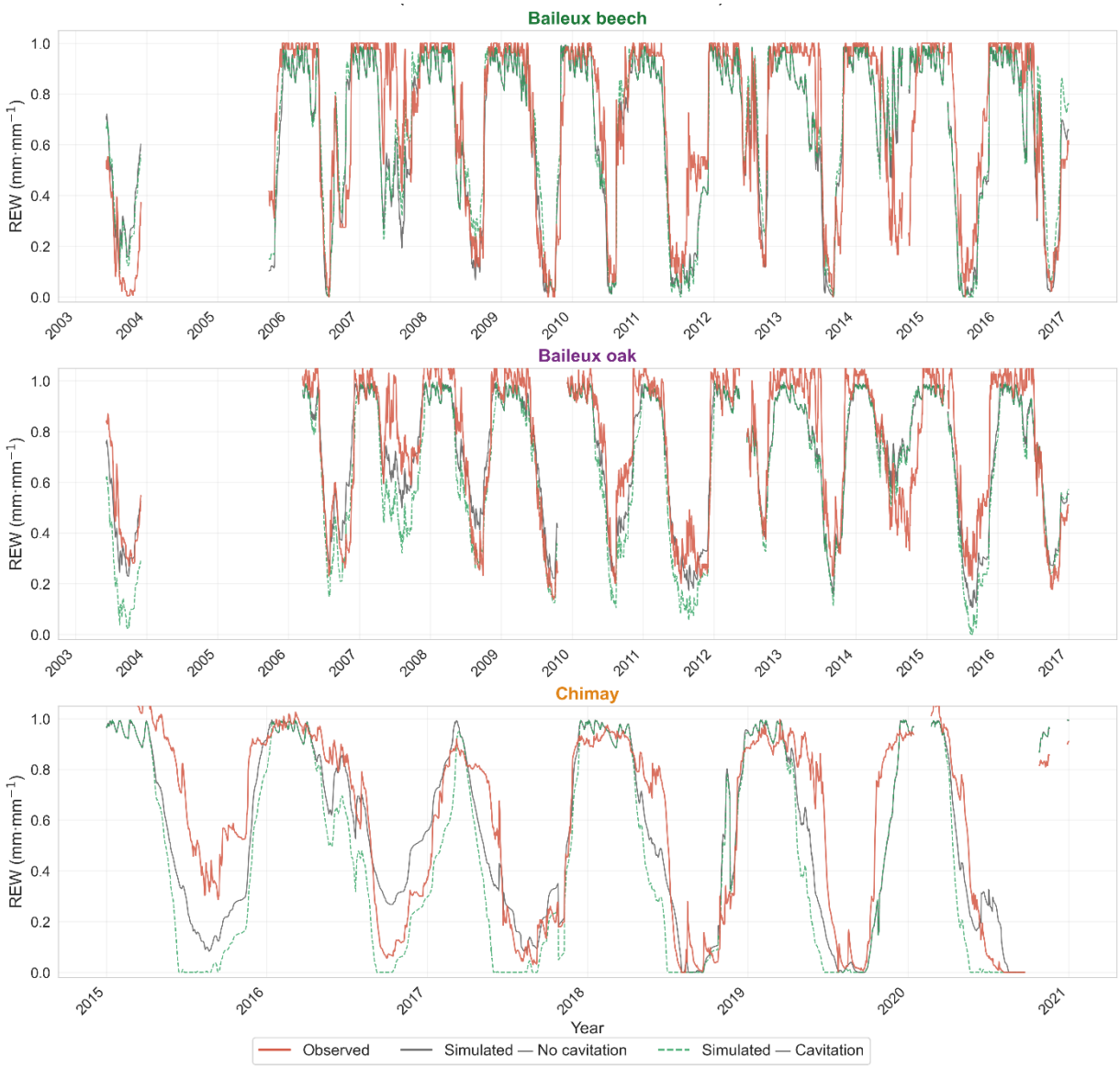

Figure A1. Daily time series of relative extractable water (REW) for the three evaluation sites, comparing observed values (red) with simulated values without cavitation module (grey) and with cavitation module (green dashed). Gaps in the observed series reflect periods without measurements.

Table A1. HETEROFOR model evaluation metrics for soil water dynamics (relative extractable water and soil water content by horizon) without the cavitation module. Bias = mean difference (simulated − observed); RMSE = root mean square error; r = Pearson correlation coefficient; n = number of daily observations.

Site	Variable	Horizon	Bias	RMSE	Pearson r	n
Baileux beech	Relative extractable water (REW)	global	-0.053	0.17	0.881	4238
Baileux beech	Soil water content by horizon	horizon 2	0.079	0.096	0.294	168
Baileux beech	Soil water content by horizon	horizon 3	0.02	0.036	0.831	4238
Baileux beech	Soil water content by horizon	horizon 4	0	0.026	0.839	4238
Baileux beech	Soil water content by horizon	horizon 5	0	0.029	0.865	4238
Baileux beech	Soil water content by horizon	horizon 6	0.081	0.086	0.858	168
Baileux beech	Soil water content by horizon	horizon 7	0.086	0.093	0.902	168
Baileux oak	Relative extractable water (REW)	global	-0.046	0.122	0.916	4010
Baileux oak	Soil water content by horizon	horizon 2	0.11	0.12	0.444	168
Baileux oak	Soil water content by horizon	horizon 3	0.157	0.159	0.865	4238
Baileux oak	Soil water content by horizon	horizon 4	0.096	0.101	0.868	4238
Baileux oak	Soil water content by horizon	horizon 5	0.097	0.1	0.868	4238
Baileux oak	Soil water content by horizon	horizon 6	0.12	0.121	0.845	168
Baileux oak	Soil water content by horizon	horizon 7	0.085	0.086	0.924	168
Chimay	Relative extractable water (REW)	global	-0.063	0.181	0.883	2075
Chimay	Soil water content by horizon	horizon 3	0.005	0.043	0.837	1937
Chimay	Soil water content by horizon	horizon 4	0.011	0.028	0.929	1957
Chimay	Soil water content by horizon	horizon 5	-0.004	0.022	0.871	1727
Chimay	Soil water content by horizon	horizon 6	0.002	0.023	0.774	1726

Table A2. HETEROFOR model evaluation metrics for soil water dynamics (relative extractable water and soil water content by horizon) with the cavitation module activated. Bias = mean difference (simulated − observed); RMSE = root mean square error; r = Pearson correlation coefficient; n = number of daily observations.

Site	Variable	Horizon	Bias	RMSE	Pearson r	n
Baileux beech	Relative extractable water (REW)	global	-0.032	0.178	0.857	4238
Baileux beech	Soil water content by horizon	horizon 2	0.08	0.094	0.386	168
Baileux beech	Soil water content by horizon	horizon 3	0.022	0.039	0.803	4238
Baileux beech	Soil water content by horizon	horizon 4	0.003	0.027	0.821	4238
Baileux beech	Soil water content by horizon	horizon 5	0.004	0.031	0.844	4238
Baileux beech	Soil water content by horizon	horizon 6	0.076	0.081	0.889	168
Baileux beech	Soil water content by horizon	horizon 7	0.078	0.086	0.9	168
Baileux oak	Relative extractable water (REW)	global	-0.099	0.161	0.906	4010
Baileux oak	Soil water content by horizon	horizon 2	0.02	0.067	0.773	4010
Baileux oak	Soil water content by horizon	horizon 3	-0.002	0.03	0.838	4010
Baileux oak	Soil water content by horizon	horizon 4	-0.058	0.062	0.831	168
Baileux oak	Soil water content by horizon	horizon 5	0.002	0.032	0.844	4010
Baileux oak	Soil water content by horizon	horizon 6	-0.023	0.03	0.842	168
Baileux oak	Soil water content by horizon	horizon 7	-0.006	0.029	0.879	4010
Baileux oak	Soil water content by horizon	horizon 8	-0.039	0.042	0.921	168
Chimay	Relative extractable water (REW)	global	-0.169	0.264	0.852	2075
Chimay	Soil water content by horizon	horizon 3	-0.009	0.054	0.774	1937
Chimay	Soil water content by horizon	horizon 4	-0.007	0.034	0.909	1957
Chimay	Soil water content by horizon	horizon 5	-0.011	0.028	0.827	1727
Chimay	Soil water content by horizon	horizon 6	-0.013	0.029	0.759	1726

Appendix B :

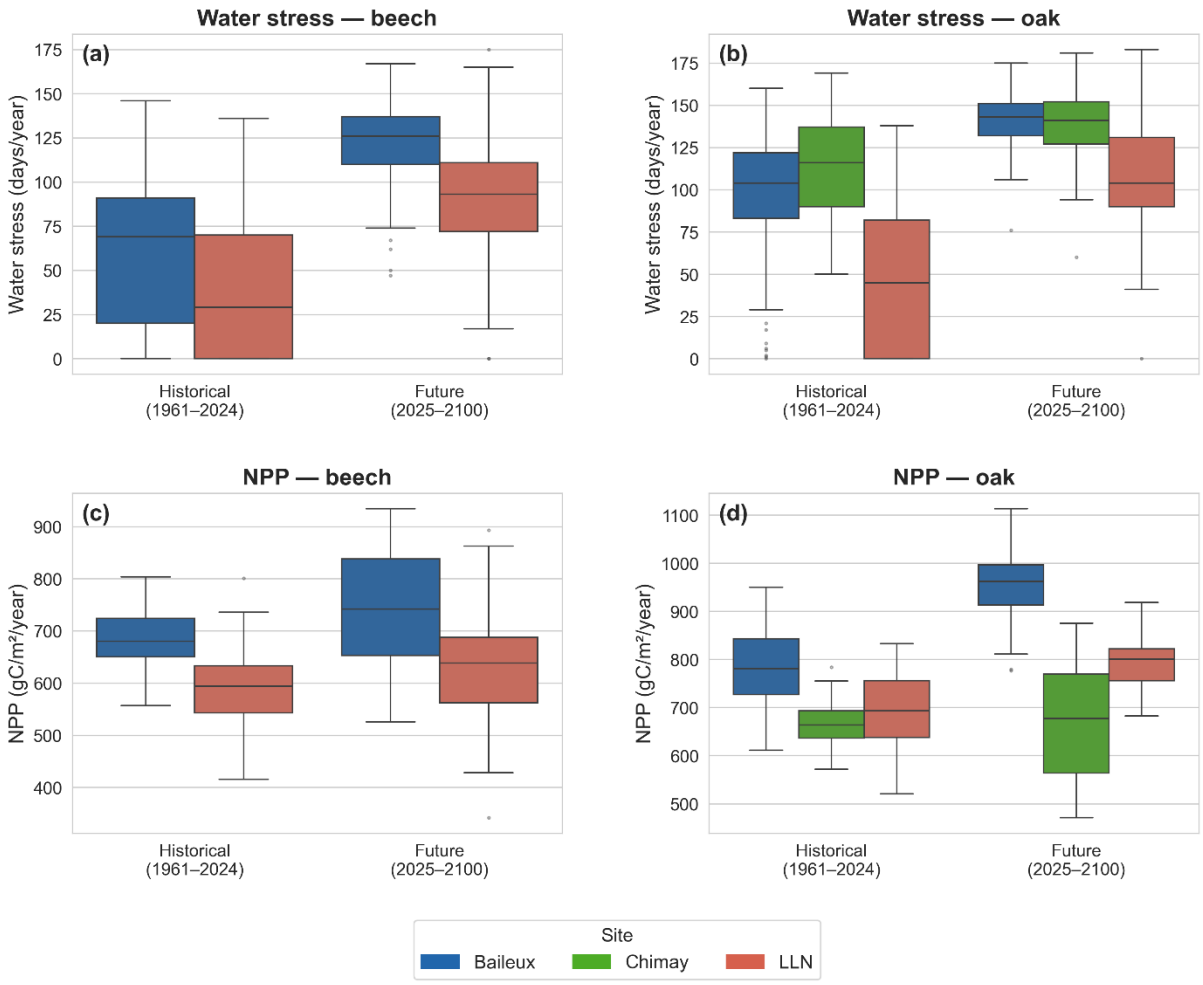

Figure B1. Site and species effects on water stress (a-b) and NPP (c-d) under historical and future CO_2 constant scenarios, with the cavitation module.

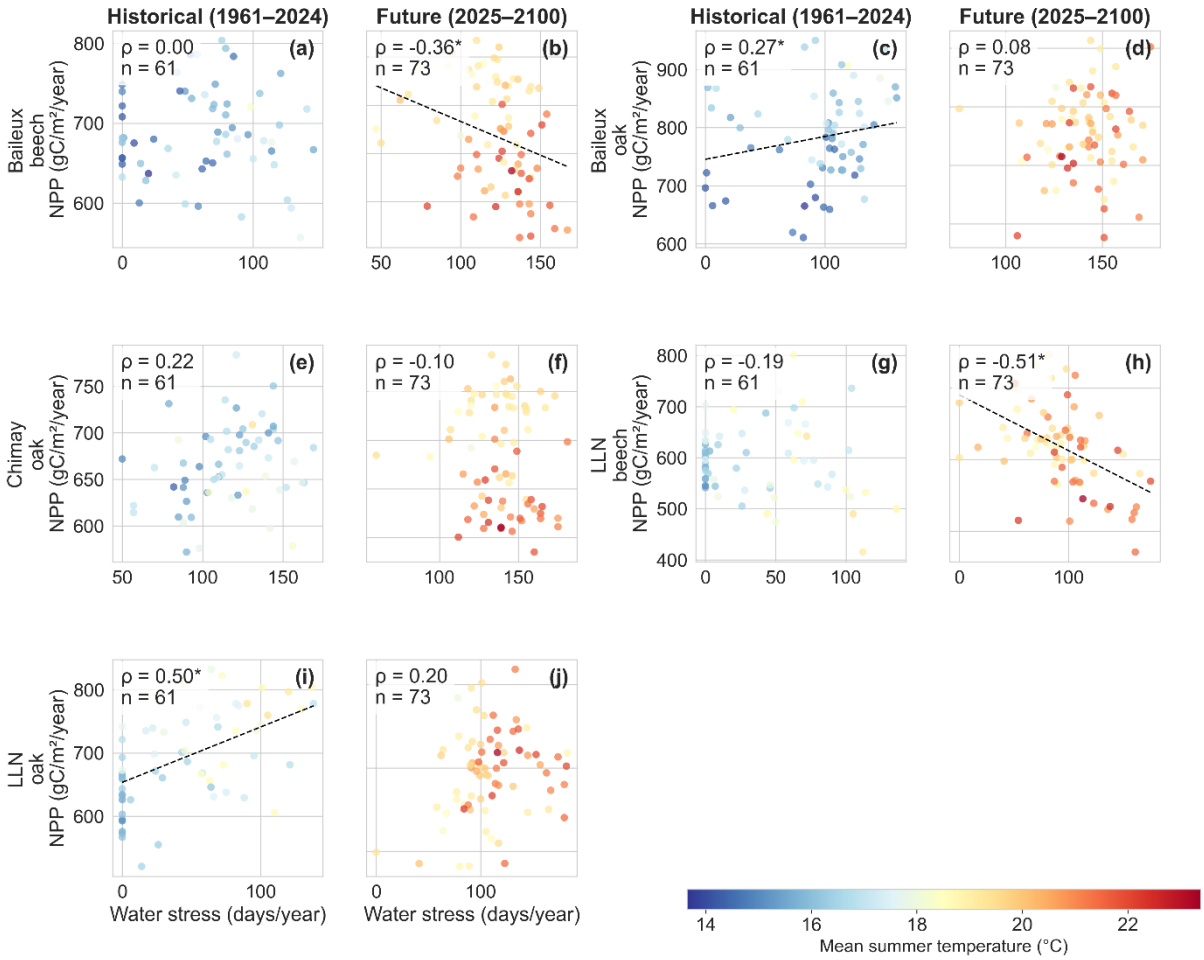

*Figure B2. NPP vs water stress for all plots under CO_2 constant scenarios, with the cavitation module. Colour indicates mean summer temperature. Dashed line = linear regression, drawn when the correlation is statistically significant. * $p < 0.05$.*

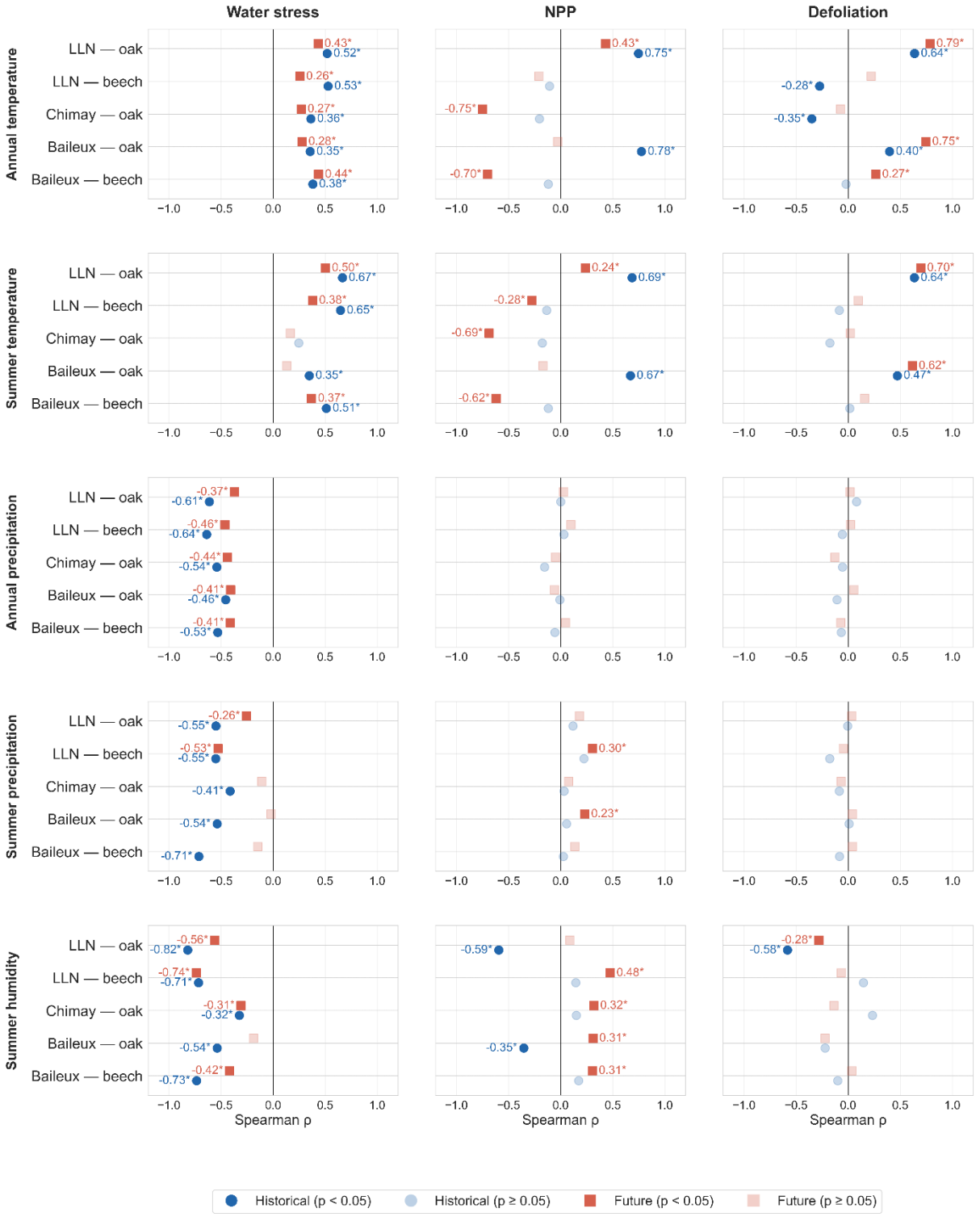

Figure B3. Spearman correlations between climatic variables and forest indicators across all plots, with the cavitation module. Filled symbols indicate significant correlations ($p < 0.05$).

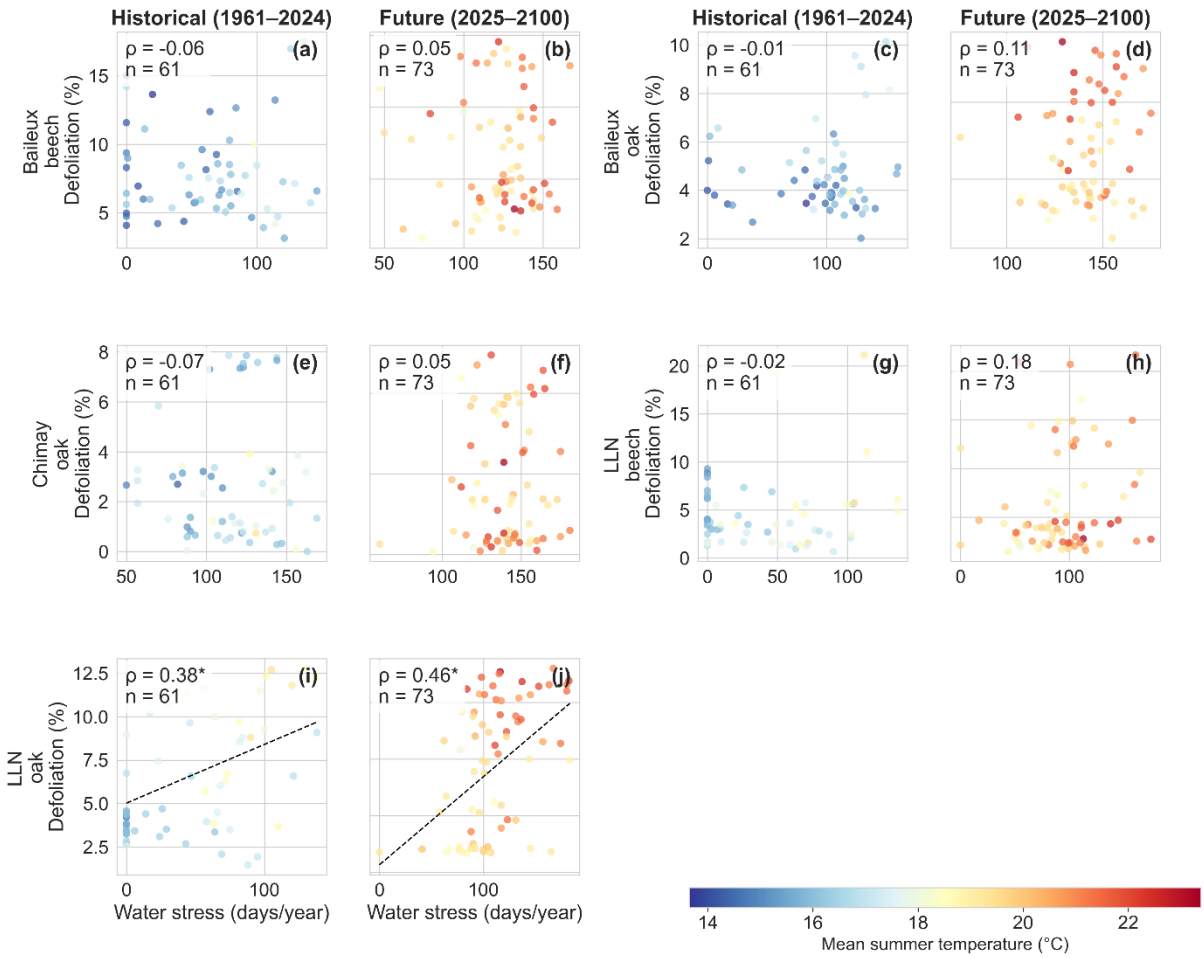

*Figure B4. Defoliation vs water stress for all plots under CO_2 constant scenarios, with the cavitation module. Colour indicates mean summer temperature. Dashed line = linear regression, drawn when the correlation is statistically significant. * $p < 0.05$.*

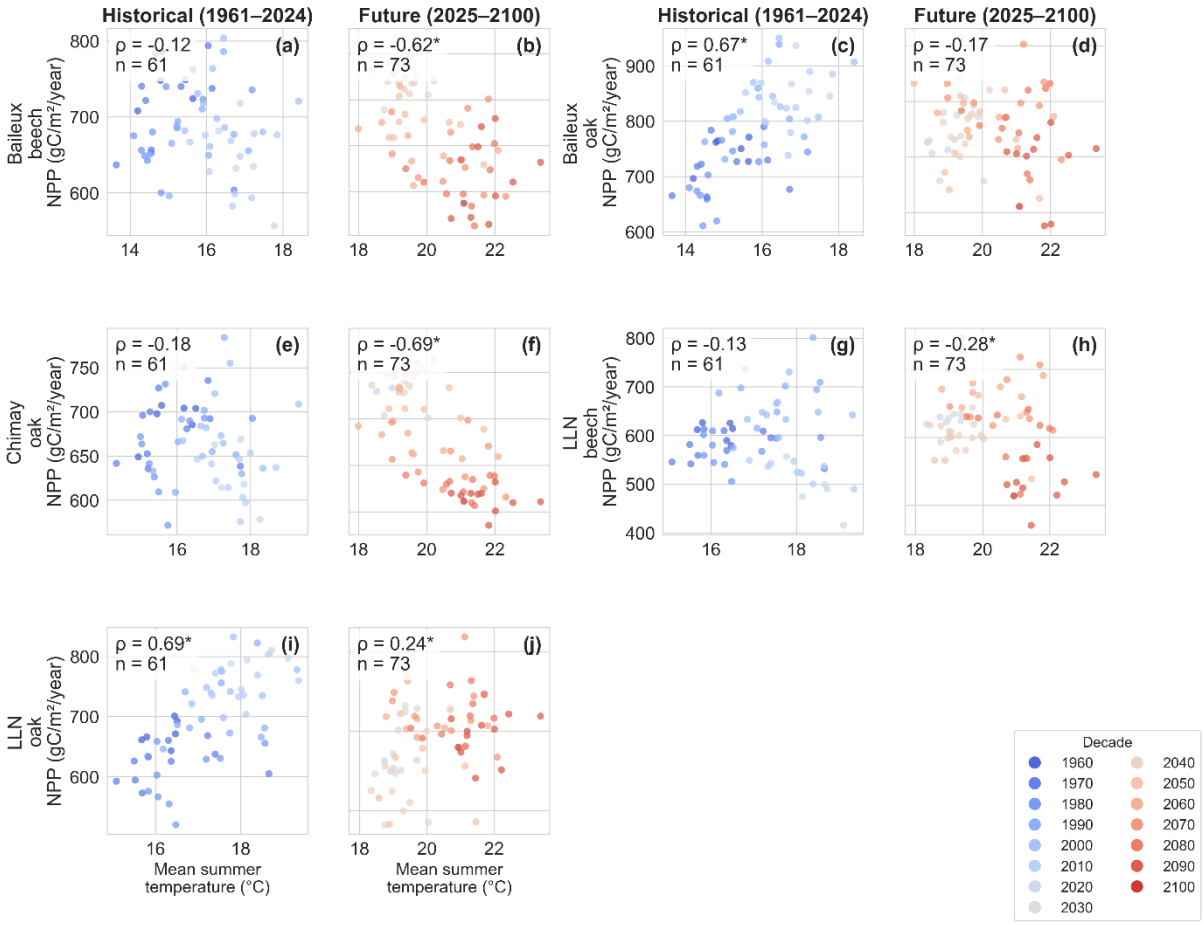

Figure B5. NPP vs mean summer temperature for all plots under CO_2 constant scenarios, with the cavitation module. Colour indicates decade.

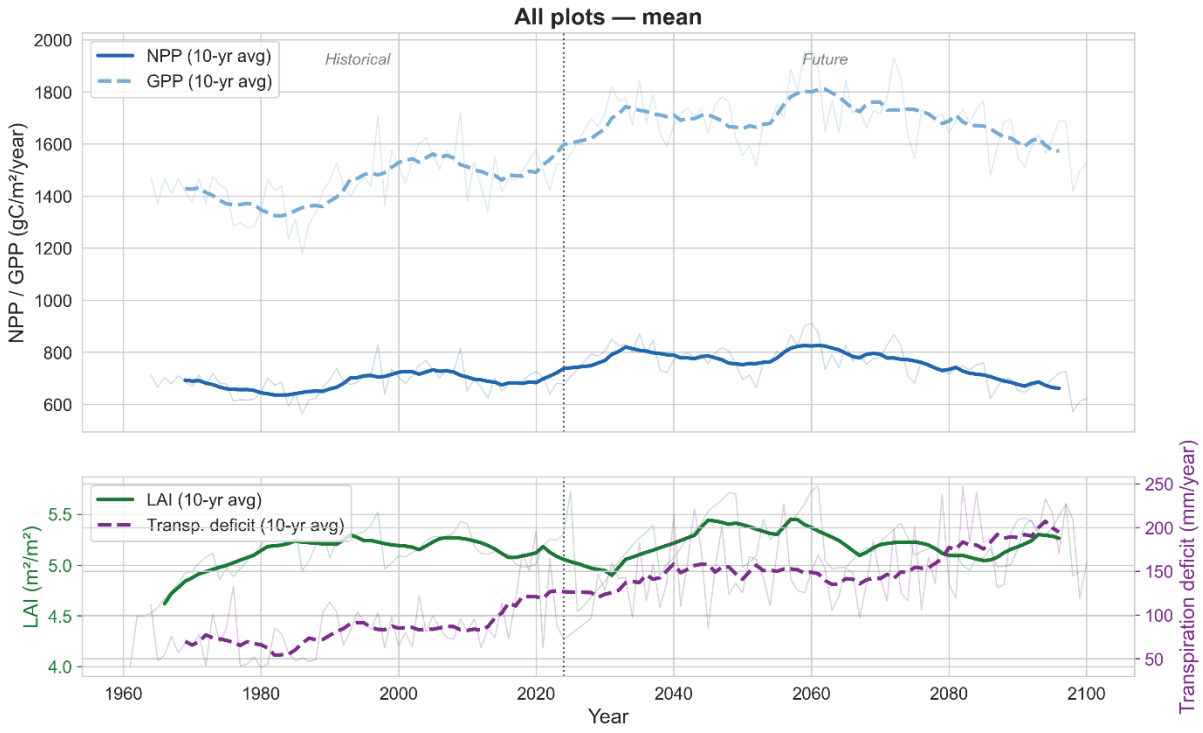

Figure B6. Mean time series of NPP, GPP (upper panel) and LAI, transpiration deficit (lower panel) averaged across all five plots, with the cavitation module activated. Thick lines = 10-year moving averages; thin lines = annual values. Dotted vertical line = 2024 transition.

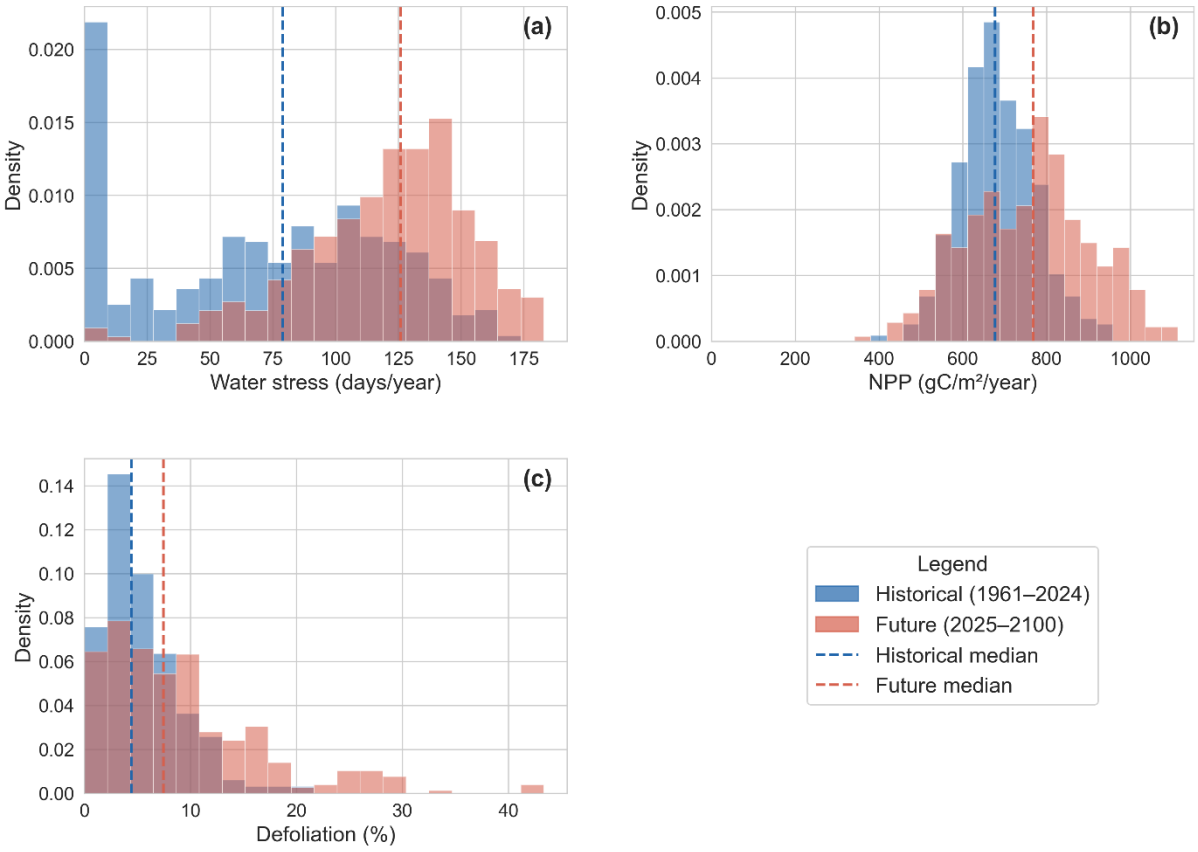

Figure B7. Historical vs future distributions of water stress (a), NPP (b) and defoliation (c) across all plots, with the cavitation module. Dashed lines indicate medians.

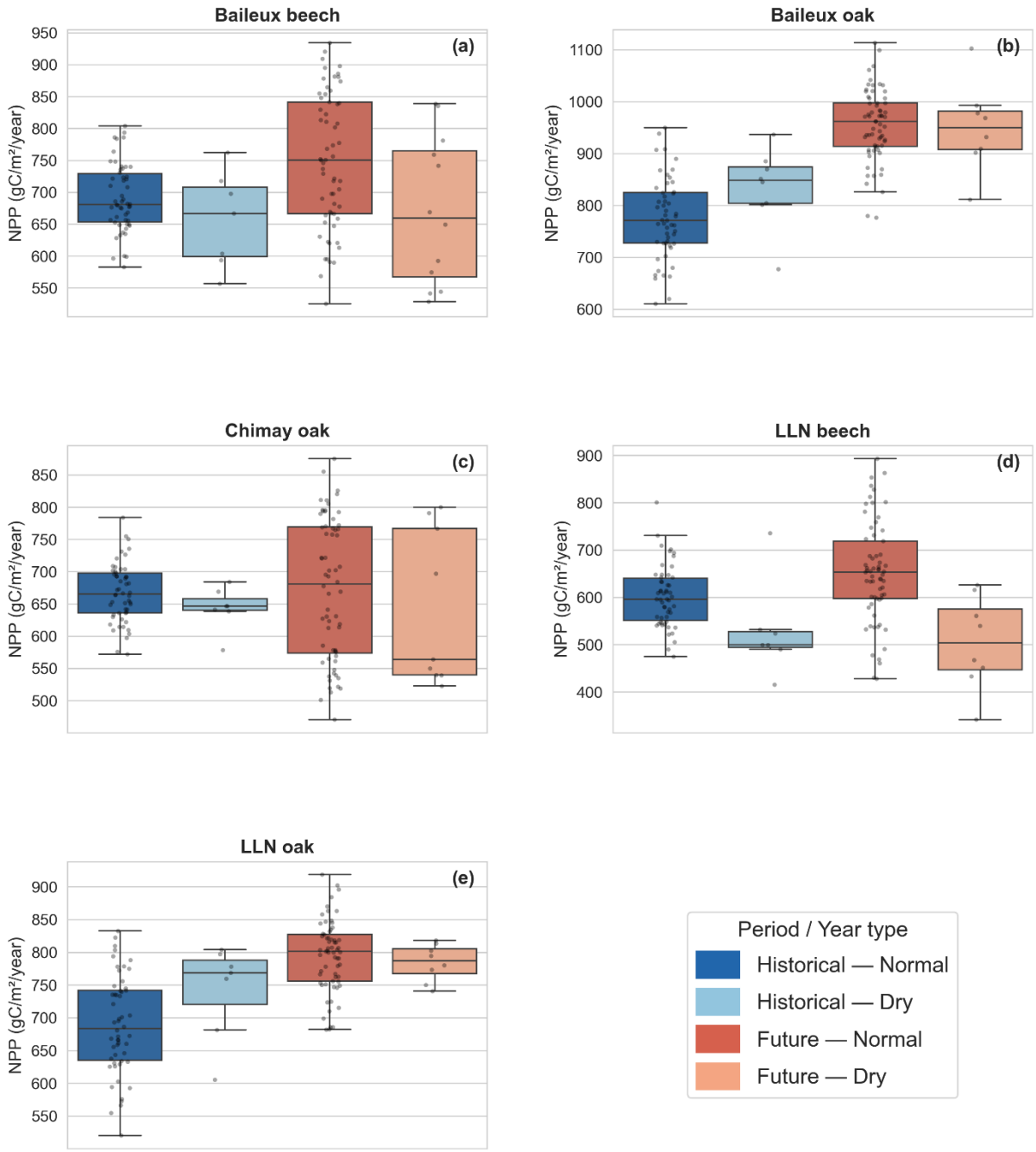

Figure B8. NPP in dry vs normal years for all plots, with the cavitation module. Dry years defined as years exceeding the 90th percentile of water stress, computed separately for each period.

Appendix C

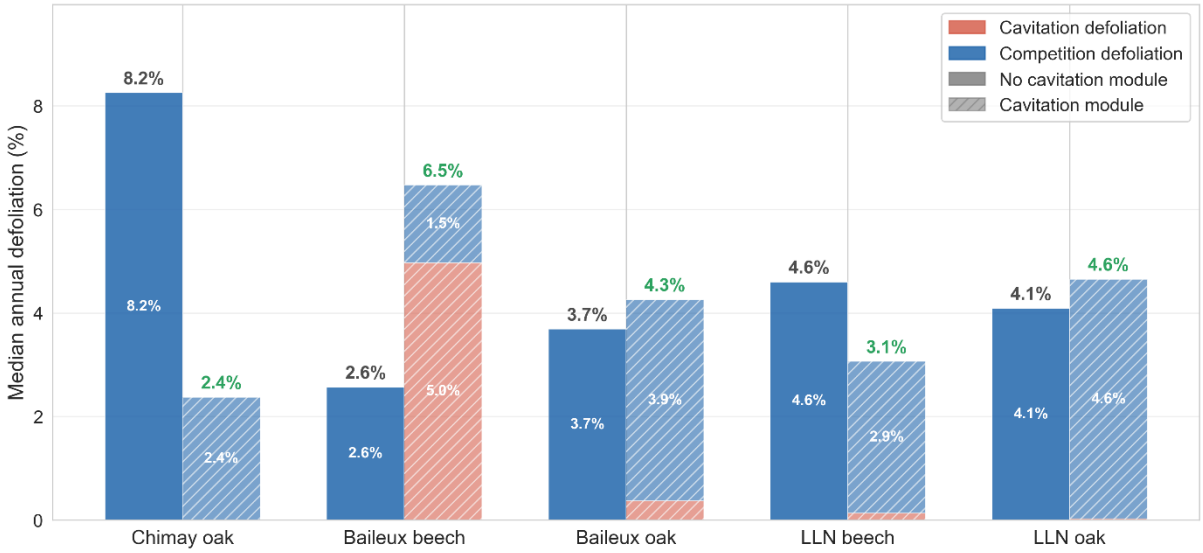

Figure C1. Median annual defoliation components across all plots for the historical period (1961-2024), with and without the cavitation module. Each group of bars shows, from left to right, the configuration without cavitation (solid fill) and with cavitation (hatched fill). Blue indicates competition-driven defoliation and red indicates cavitation-driven defoliation. Total bar height represents total defoliation. Values above bars indicate total median defoliation (%).

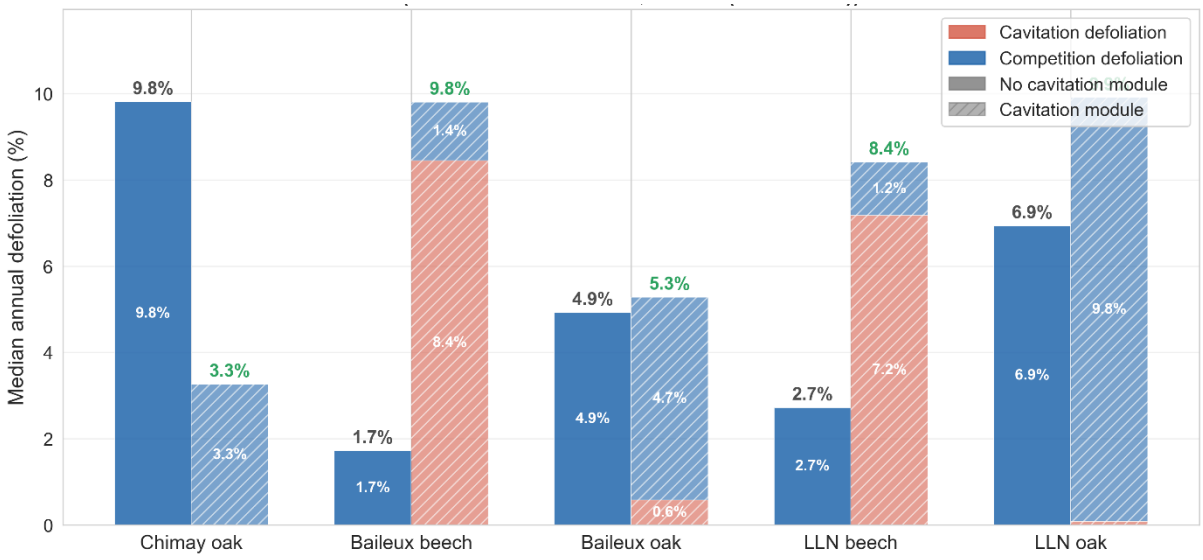

Figure C2. Median annual defoliation components across all plots for the future period (2025-2100), with and without the cavitation module. Each group of bars shows, from left to right, the configuration without cavitation (solid fill) and with cavitation (hatched fill). Blue indicates competition-driven defoliation and red indicates cavitation-driven defoliation. Total bar height represents total defoliation. Values above bars indicate total median defoliation (%).

Appendix D

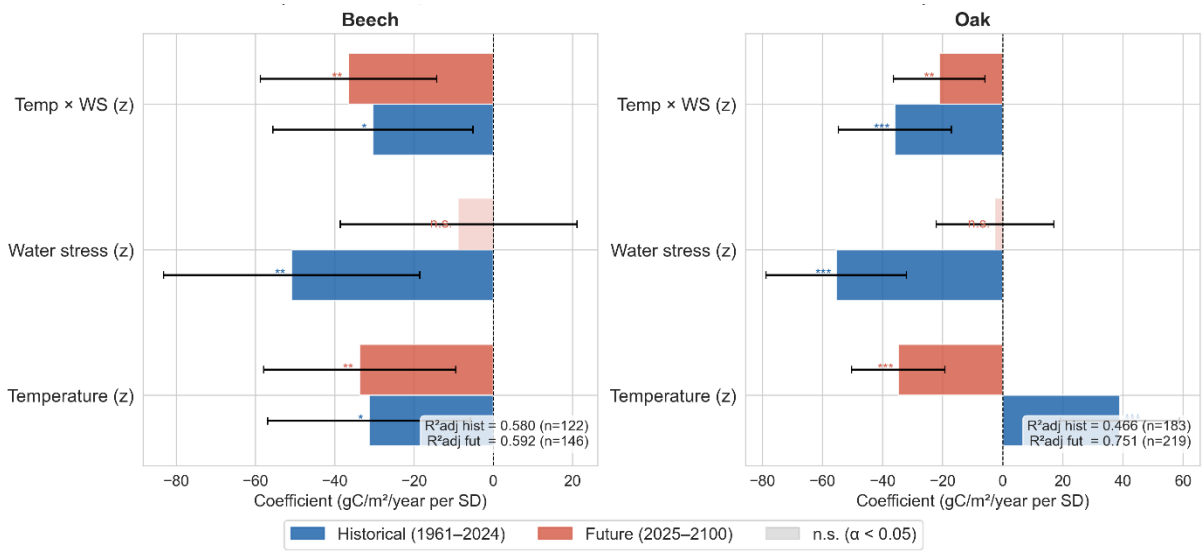

Figure D1. Standardised regression coefficients of the multiple regression model NPP ~ Temperature + Water stress + Temperature×Water stress, fitted separately for beech (left) and oak (right) and for the historical (1961-2024, blue) and future (2025-2100, orange) periods, controlling for site effect. Predictors are centred and scaled to allow direct comparison of coefficients. Transparent bars indicate non-significant coefficients (α < 0.05). Error bars represent 95% confidence intervals. Adjusted R² values are indicated for each period. All simulations use a constant CO_2 concentration without the cavitation module.

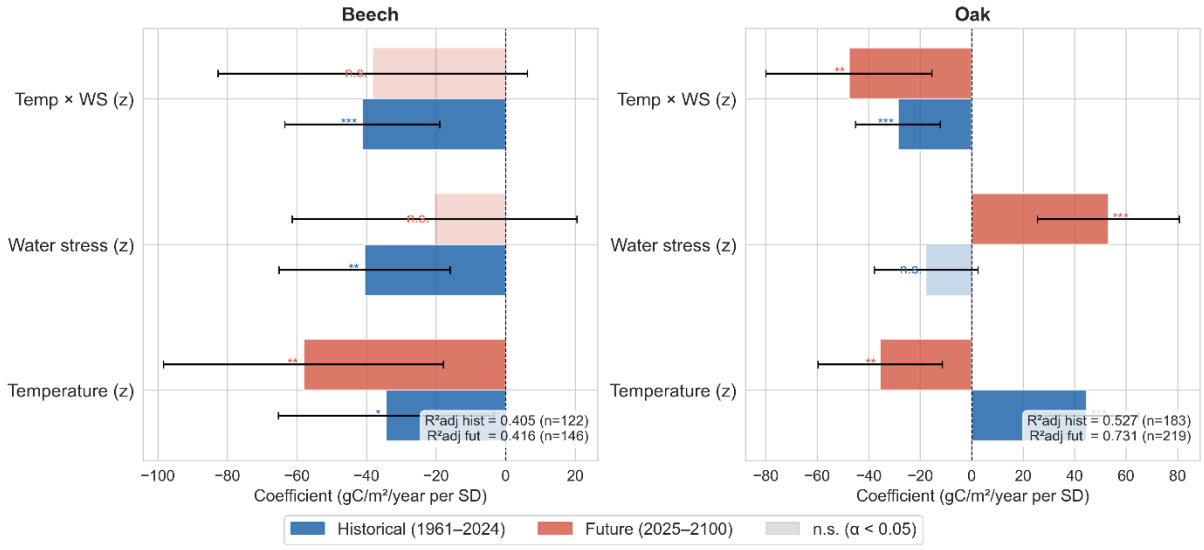

Figure D2. Standardised regression coefficients of the multiple regression model NPP ~ Temperature + Water stress + Temperature×Water stress, fitted separately for beech (left) and oak (right) and for the historical (1961-2024, blue) and future (2025-2100, orange) periods, controlling for site effect. Predictors are centred and scaled to allow direct comparison of coefficients. Transparent bars indicate non-significant coefficients (α < 0.05). Error bars represent 95% confidence intervals. Adjusted R² values are indicated for each period. All simulations use a constant CO_2 concentration with the cavitation module activated.

Appendix E

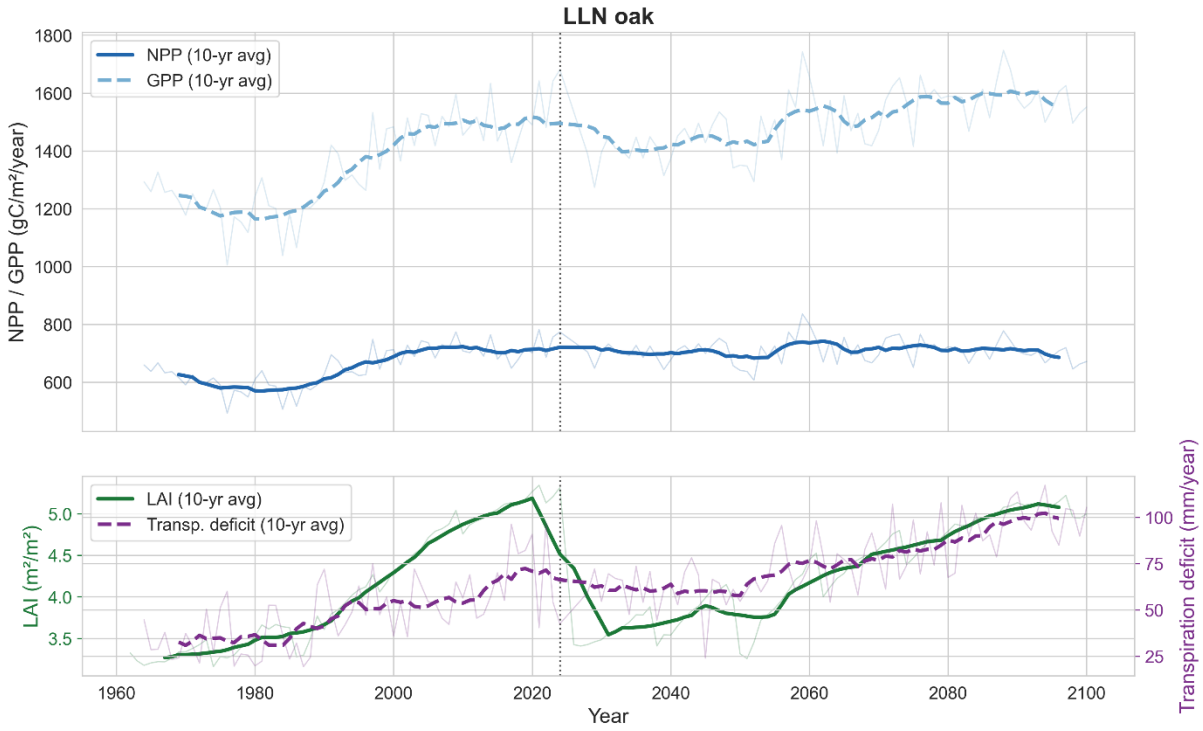

Figure E1. Time series of NPP, GPP (upper panel) and LAI, transpiration deficit (lower panel) for LLN oak, under constant CO_2 scenarios. Thick lines = 10-year moving averages; thin lines = annual values. Dotted vertical line = 2024 transition.

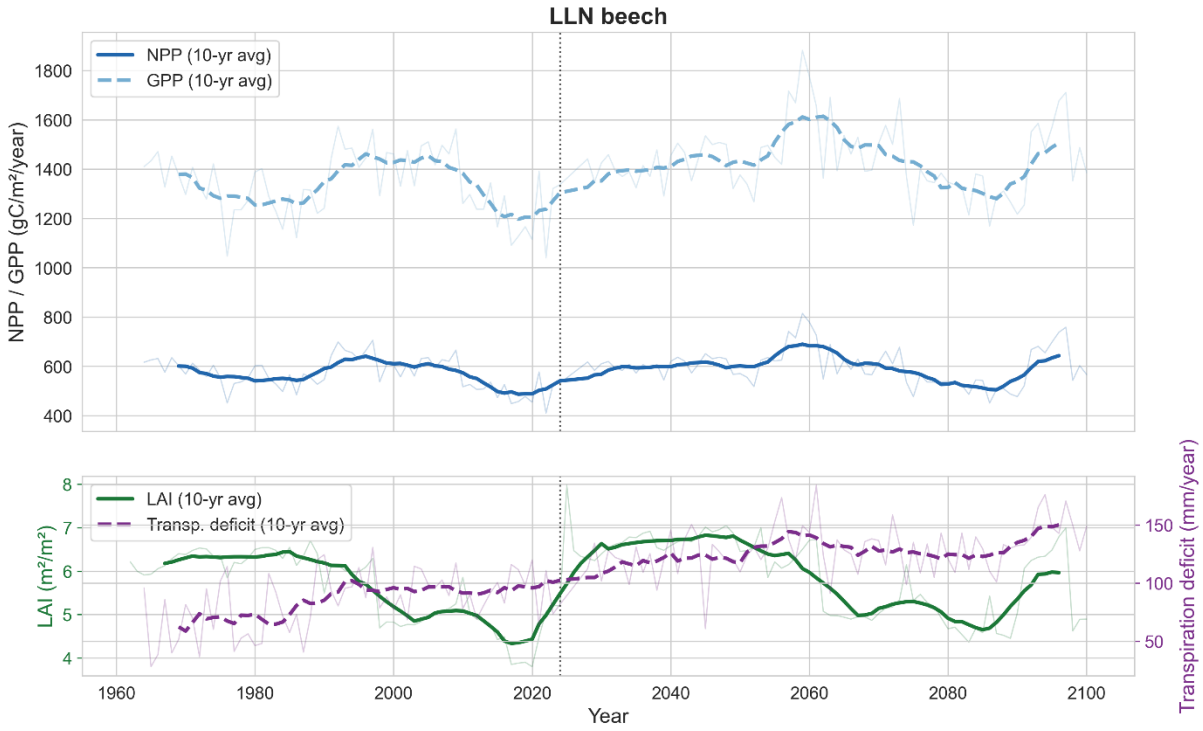

Figure E2. Time series of NPP, GPP (upper panel) and LAI, transpiration deficit (lower panel) for LLN beech, under constant CO_2 scenarios. Thick lines = 10-year moving averages; thin lines = annual values. Dotted vertical line = 2024 transition.

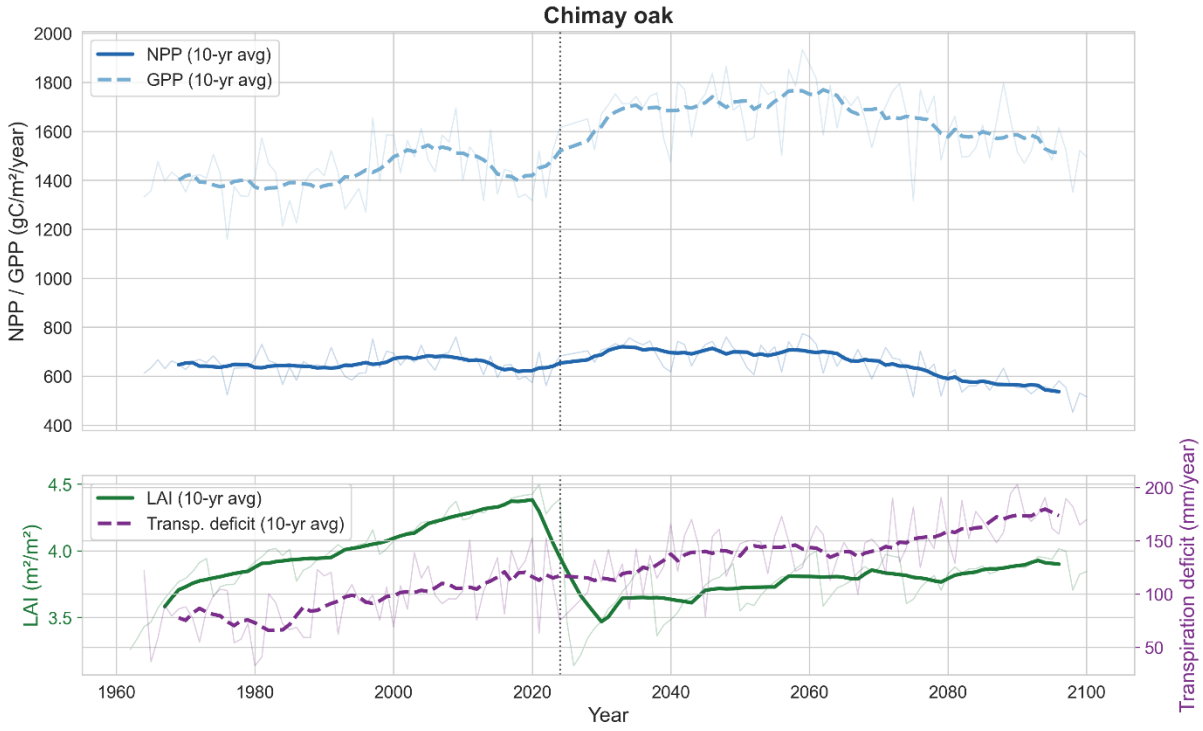

Figure E3. Time series of NPP, GPP (upper panel) and LAI, transpiration deficit (lower panel) for Chimay oak, under constant CO_2 scenarios. Thick lines = 10-year moving averages; thin lines = annual values. Dotted vertical line = 2024 transition.

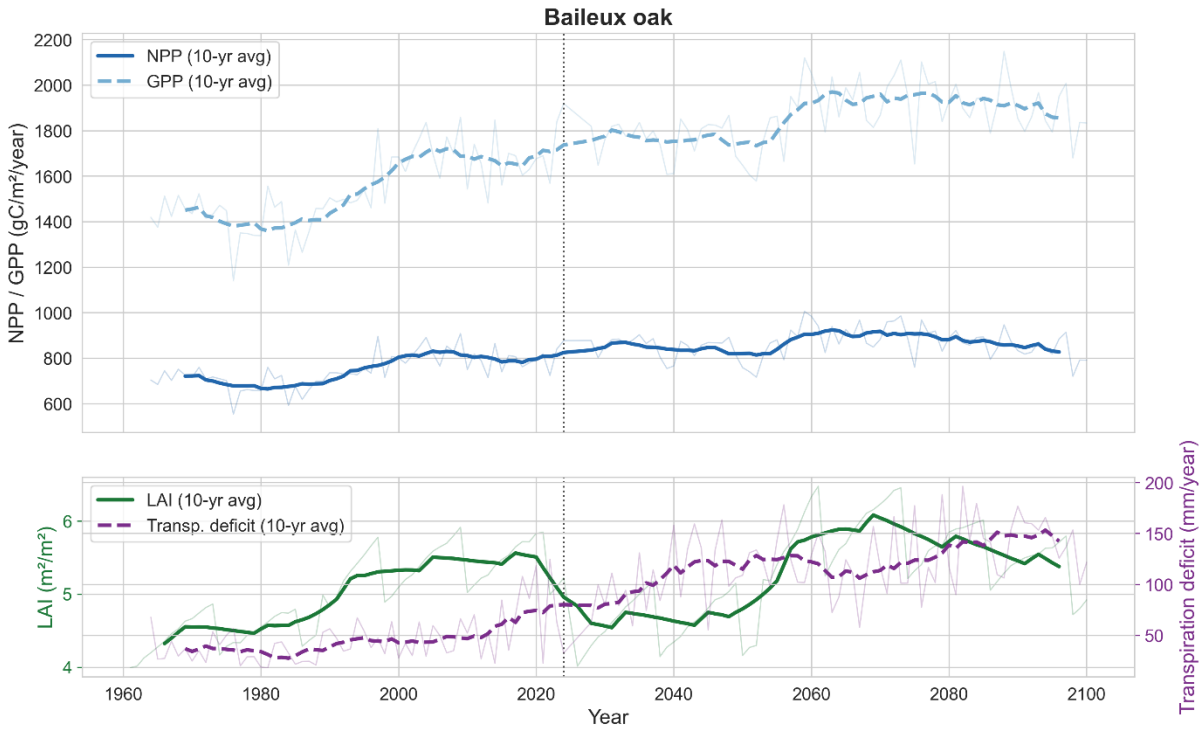

Figure E4. Time series of NPP, GPP (upper panel) and LAI, transpiration deficit (lower panel) for Baileux oak, under constant CO_2 scenarios. Thick lines = 10-year moving averages; thin lines = annual values. Dotted vertical line = 2024 transition.

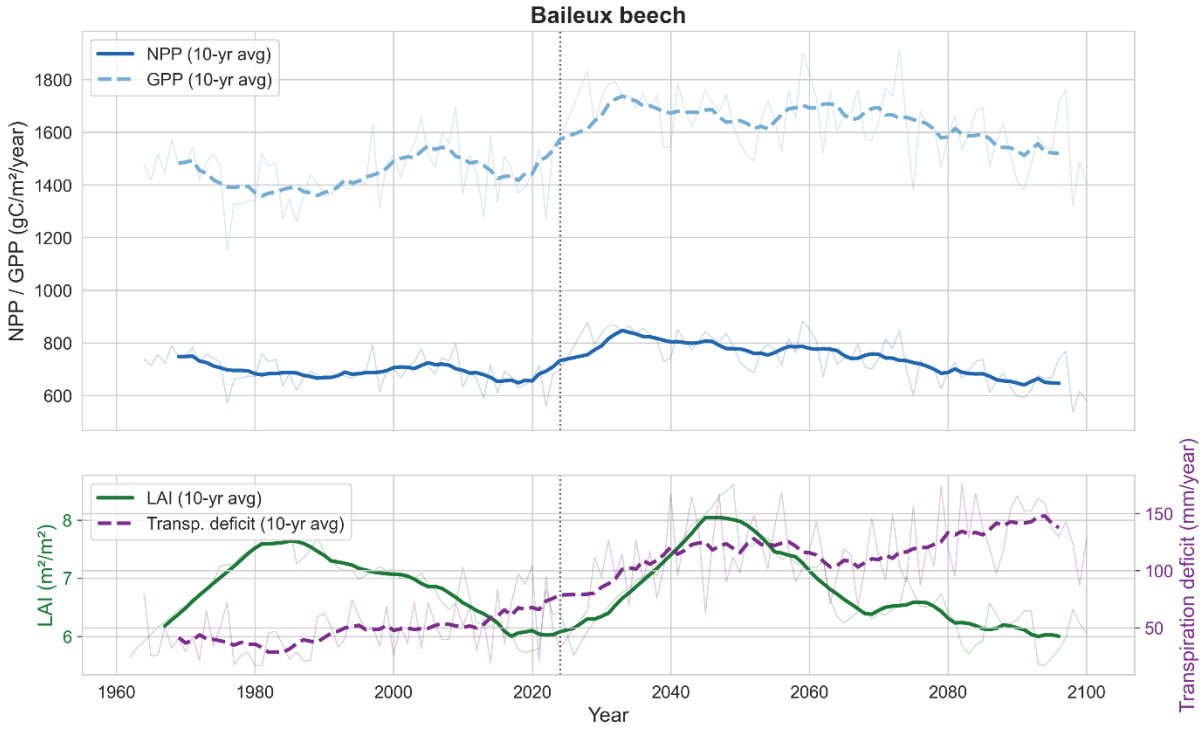

Figure E5. Time series of NPP, GPP (upper panel) and LAI, transpiration deficit (lower panel) for Baileux beech, under constant CO_2 scenarios. Thick lines = 10-year moving averages; thin lines = annual values. Dotted vertical line = 2024 transition.

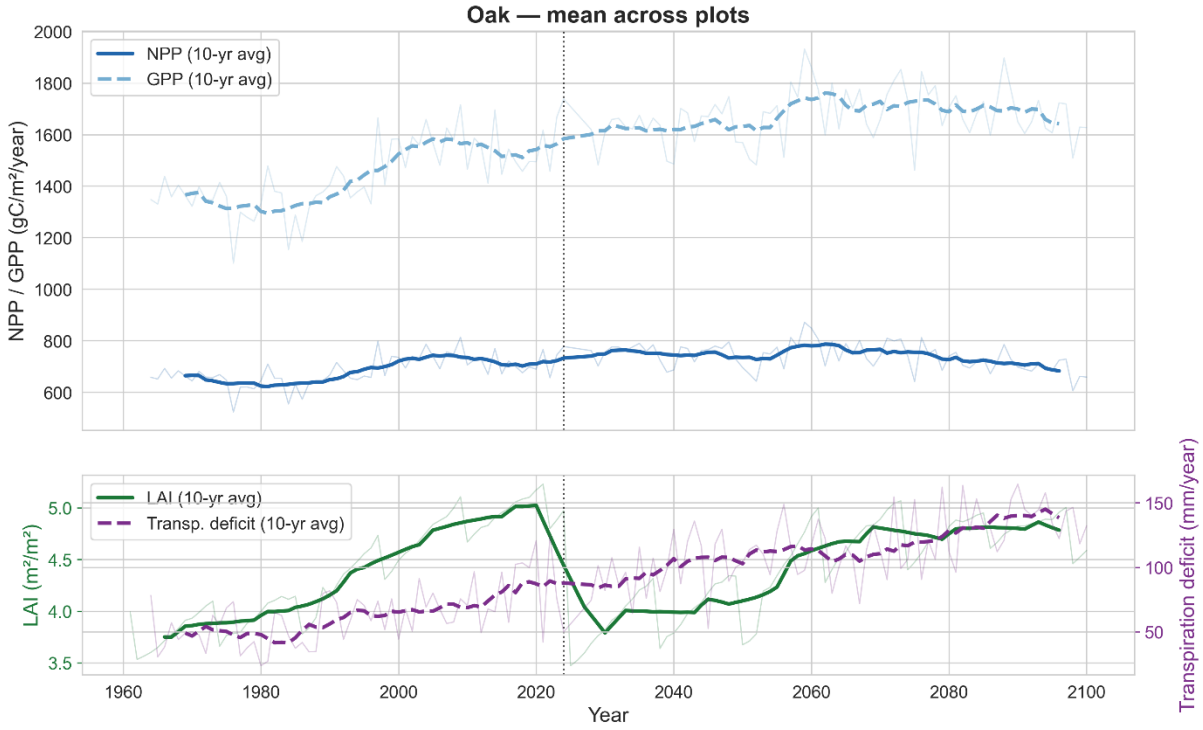

Figure E6. Time series of NPP, GPP (upper panel) and LAI, transpiration deficit (lower panel) averaged across the three oak plots (Baileux, Chimay, LLN), under constant CO_2 scenarios. Thick lines = 10-year moving averages; thin lines = annual values. Dotted vertical line = 2024 transition.

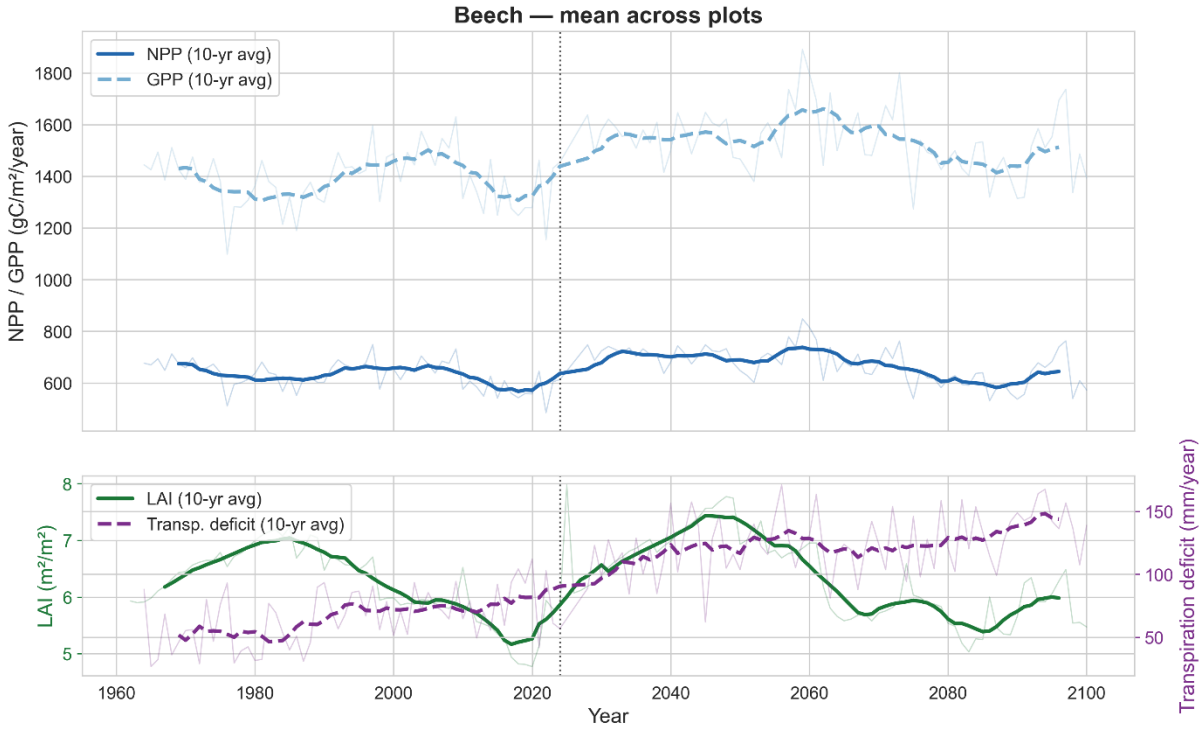

Figure E7. Time series of NPP, GPP (upper panel) and LAI, transpiration deficit (lower panel) averaged across the two beech plots (Baileux, LLN), under constant CO_2 scenarios. Thick lines = 10-year moving averages; thin lines = annual values. Dotted vertical line = 2024 transition.

Appendix F

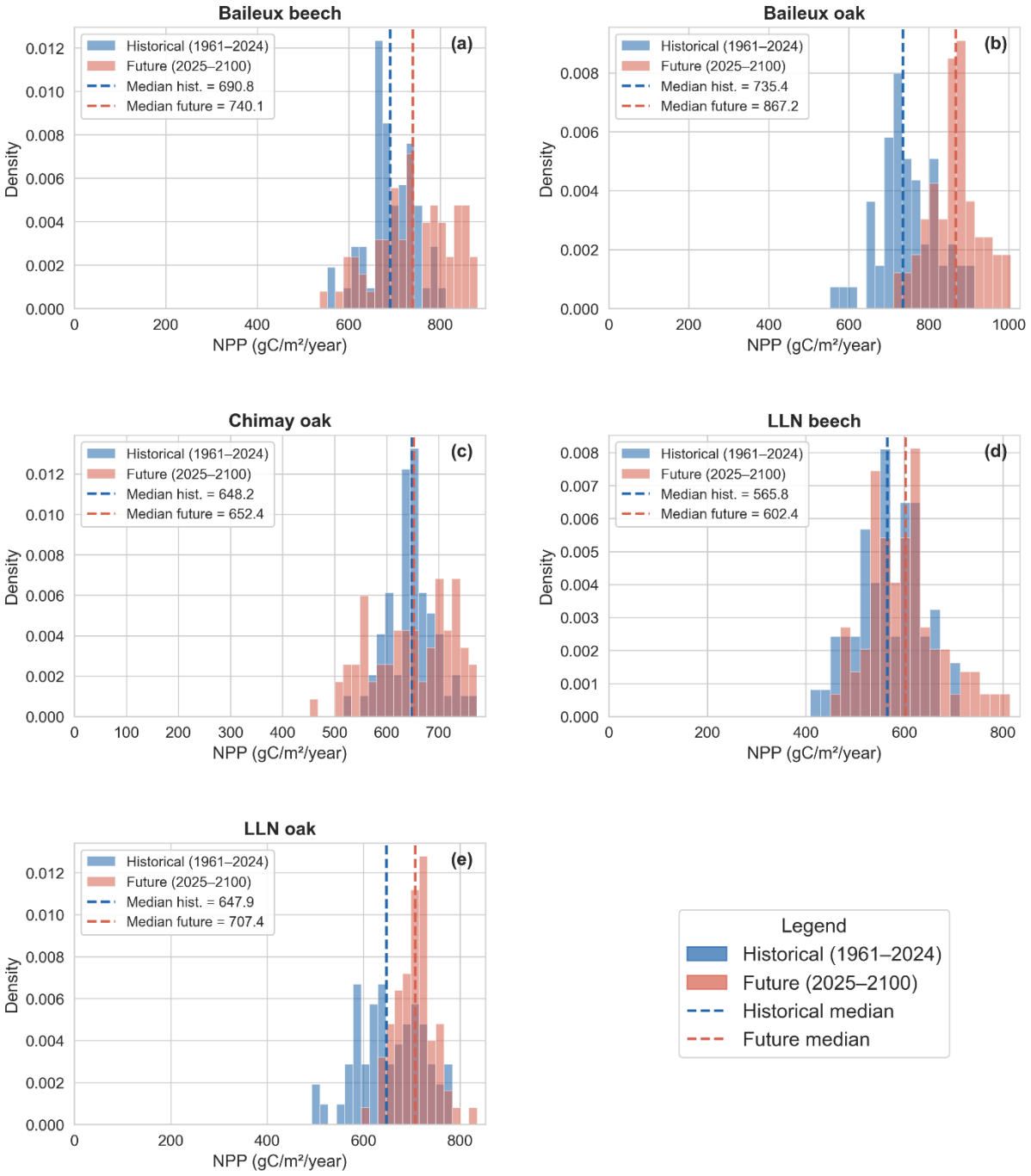

Figure F1. Historical vs future distributions of NPP across all plots. Dashed lines indicate medians.

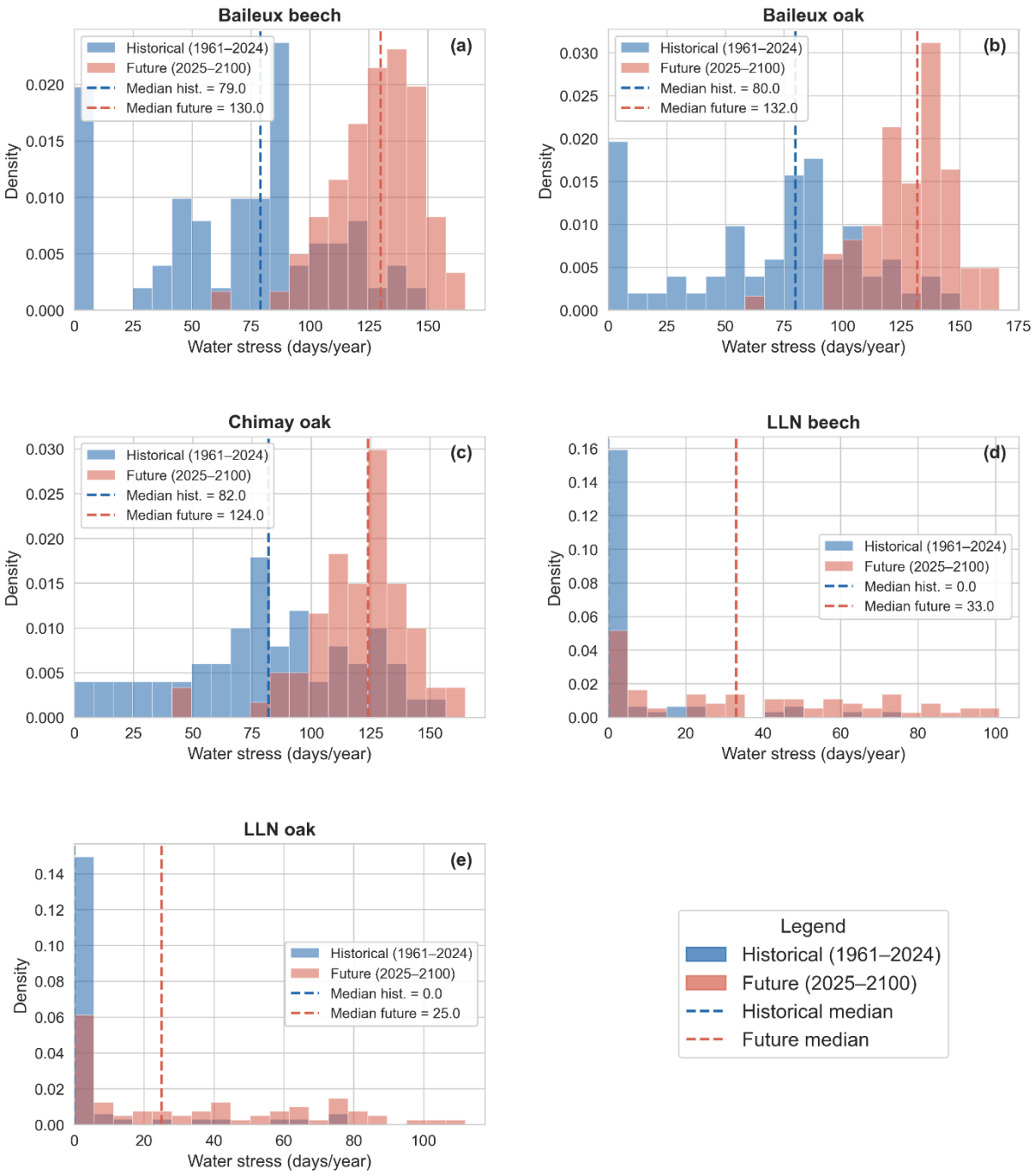

Figure F2. Historical vs future distributions of water stress across all stands. Dashed lines indicate medians.

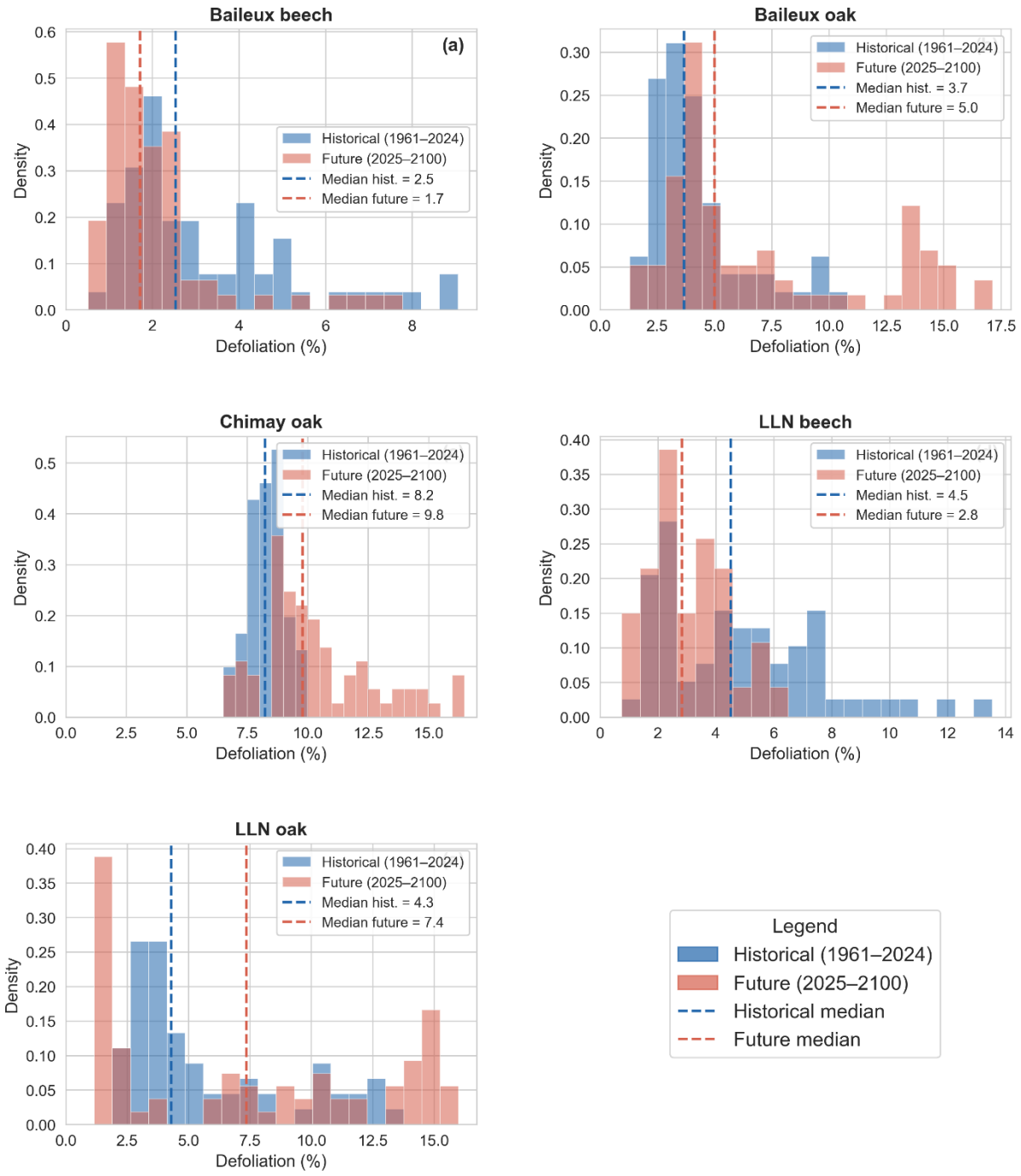

Figure F3. Historical vs future distributions of defoliation across all stands. Dashed lines indicate medians.

Appendix G

Table G1 : Continuous REW trends at LLN (Mann-Kendall/Sen slope), IRM vs GFDL-ESM4, without cavitation.

Species	Metric	IRM slope	IRM p	GFDL slope	GFDL p
Beech	REW mean	-0.00131	0.0001	-0.00024	0.3021
Beech	REW min	-0.00148	0	-0.00009	0.6607
Oak	REW mean	-0.00148	0.0006	-0.00039	0.1202
Oak	REW min	-0.00178	0.0009	-0.00036	0.2751

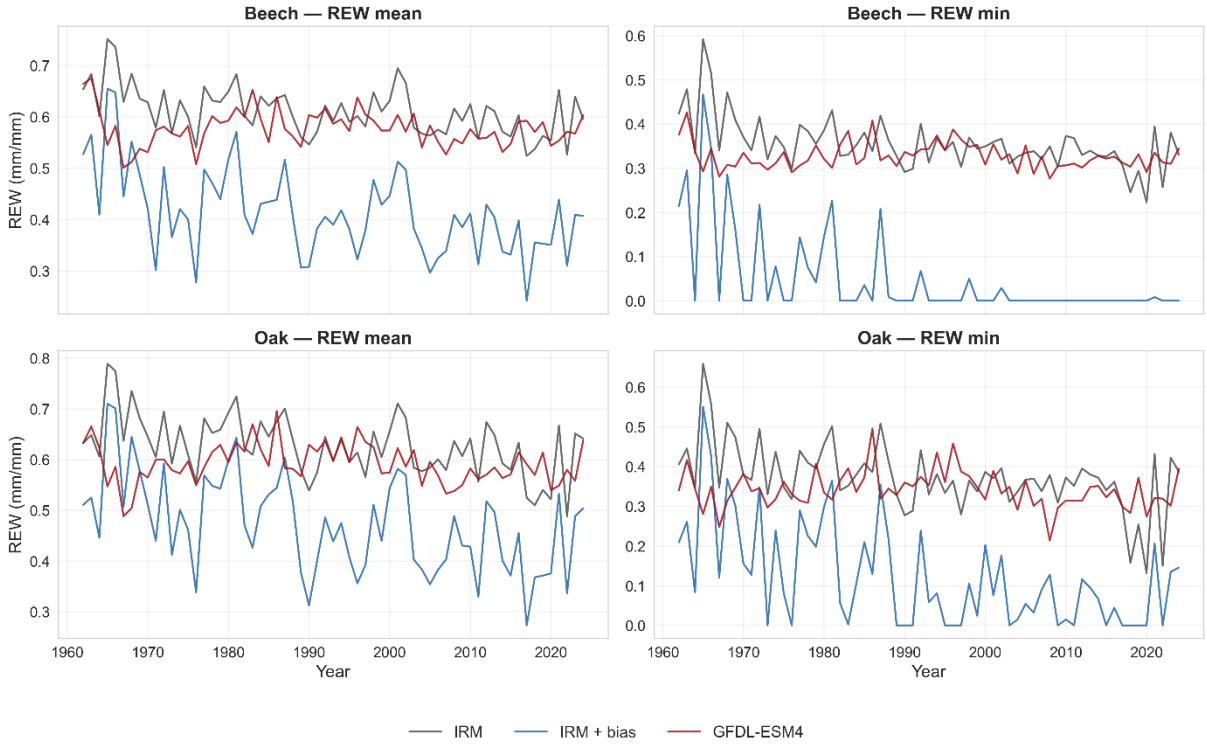

Figure G1 : Continuous relative extractable water (REW, mean and minimum annual values) at LLN, for IRM (observed), IRM+bias (IRM data shifted to GFDL-ESM4's mean summer temperature level, real IRM trend and interannual variability preserved), and GFDL-ESM4, without cavitation. Despite IRM+bias and GFDL-ESM4 sharing the same mean temperature level over the full period, IRM+bias declines markedly more than GFDL-ESM4, particularly over the most recent years: because the constant offset equalises the overall mean rather than each individual year, it also carries forward IRM's true recent acceleration and its full interannual variability, neither of which GFDL-ESM4 reproduces (attenuated interannual variance, see section 3.4.1). For beech, minimum REW under IRM+bias approaches a floor value for most years after approximately 2000, indicating that this metric reaches a physical lower limit under this configuration.

Table G2 : Continuous REW trends at LLN (Mann-Kendall/Sen slope), IRM vs GFDL-ESM4, with cavitation activated in both cases.

Species	Metric	IRM_cavit slope	IRM_cavit p	GFDL_cavit slope	GFDL_cavit p
Beech	REW mean	-0.00293	0	-0.0003	0.5218
Beech	REW min	-0.00451	0	0	0.1314
Oak	REW mean	-0.00302	0	-0.00091	0.0242
Oak	REW min	-0.00434	0	0	0.236

Table G3 : Continuous REW trends at LLN (Mann-Kendall/Sen slope), IRM vs IRM+bias.

Species	Metric	IRM slope	IRM p	IRM_adj slope	IRM_adj p
Beech	REW mean	-0.00131	0.0001	-0.00221	0.0001
Beech	REW min	-0.00148	0	0	0.0007
Oak	REW mean	-0.00148	0.0006	-0.00261	0.0001
Oak	REW min	-0.00178	0.0009	-0.00308	0.0001

Appendix H

Table H1. Trend slopes for water stress by 20-year block (Method B, without cavitation), for all sites and species.

Site	Species	Block	IRM slope	IRM p	GFDL slope	GFDL p
Baileux	beech	1965-1984	0.7158	0.6575	0.094	0.9038
Baileux	beech	1985-2004	1.8098	0.1511	0.6361	0.4778
Baileux	beech	2005-2024	-0.5256	0.7636	0.1699	0.6993
Baileux	oak	1965-1984	0.806	0.6338	0.5113	0.502
Baileux	oak	1985-2004	1.2053	0.3414	-0.5256	0.6148
Baileux	oak	2005-2024	-0.8519	0.6571	-0.2985	0.6025
Chimay	oak	1965-1984	-1.0632	0.4757	-0.7789	0.443
Chimay	oak	1985-2004	1.7068	0.177	0.4789	0.7524
Chimay	oak	2005-2024	-0.7624	0.6458	0.0504	0.9541
LLN	beech	1965-1984	0.106	0.8026	-0.6662	0.3498
LLN	beech	1985-2004	-0.2218	0.614	0.4008	0.3365
LLN	beech	2005-2024	1.5955	0.0685	-0.6895	0.2789
LLN	oak	1965-1984	0.009	0.8026	-1.203	0.053
LLN	oak	1985-2004	-0.2797	0.6289	0.3564	0.0865
LLN	oak	2005-2024	2.1391	0.0439	-0.5729	0.4467

Table H2. Trend slopes for NPP by 20-year block (Method B, without cavitation), for all sites and species.

Site	Species	Block	IRM slope	IRM p	GFDL slope	GFDL p
Baileux	beech	1965-1984	-4.0017	0.0525	-5.3494	0.0233
Baileux	beech	1985-2004	3.5704	0.0251	2.0233	0.3552
Baileux	beech	2005-2024	-3.6536	0.0904	-1.6714	0.3408
Baileux	oak	1965-1984	-3.459	0.0931	-4.9211	0.0402
Baileux	oak	1985-2004	10.3435	0	9.6523	0.0006
Baileux	oak	2005-2024	-0.6664	0.7483	2.2799	0.1902
Chimay	oak	1965-1984	-0.51	0.7623	-1.6439	0.3966
Chimay	oak	1985-2004	3.3121	0.0644	0.0074	0.9963
Chimay	oak	2005-2024	-3.3394	0.0825	1.5569	0.2323
LLN	beech	1965-1984	-4.7216	0.006	-2.3584	0.1272
LLN	beech	1985-2004	2.9154	0.2217	1.3237	0.6524
LLN	beech	2005-2024	-7.8319	0.0014	-0.2434	0.8409
LLN	oak	1965-1984	-4.3486	0.006	-3.8482	0.042
LLN	oak	1985-2004	8.4968	0	7.9644	0.0001
LLN	oak	2005-2024	0.6218	0.6763	4.677	0.0012

Table H3. Trend slopes for defoliation by 20-year block (Method B, without cavitation), for all sites and species.

Site	Species	Block	IRM slope	IRM p	GFDL slope	GFDL p
Baileux	beech	1965-1984	-0.1373	0.0391	-0.1599	0.0123
Baileux	beech	1985-2004	-0.0948	0.0012	-0.0477	0.0107
Baileux	beech	2005-2024	-0.0362	0.0187	-0.0158	0.1332
Baileux	oak	1965-1984	-0.0851	0.0099	-0.1307	0.0011
Baileux	oak	1985-2004	-0.0071	0.7842	0.1001	0.0007
Baileux	oak	2005-2024	0.3398	0	0.3029	0.0048
Chimay	oak	1965-1984	0.0728	0.0001	-0.4596	0
Chimay	oak	1985-2004	-0.1087	0.0017	-0.0081	0.7899
Chimay	oak	2005-2024	-0.024	0.3767	0.1597	0.2352
LLN	beech	1965-1984	0.1584	0.04	0.1923	0.004
LLN	beech	1985-2004	-0.1593	0.0634	-0.0861	0.2679
LLN	beech	2005-2024	0.1613	0.0711	-0.1067	0.0055
LLN	oak	1965-1984	0.0768	0.0002	0.0705	0.0001
LLN	oak	1985-2004	0.136	0.0007	0.2798	0
LLN	oak	2005-2024	0.3292	0	0.1537	0.0047

Appendix I

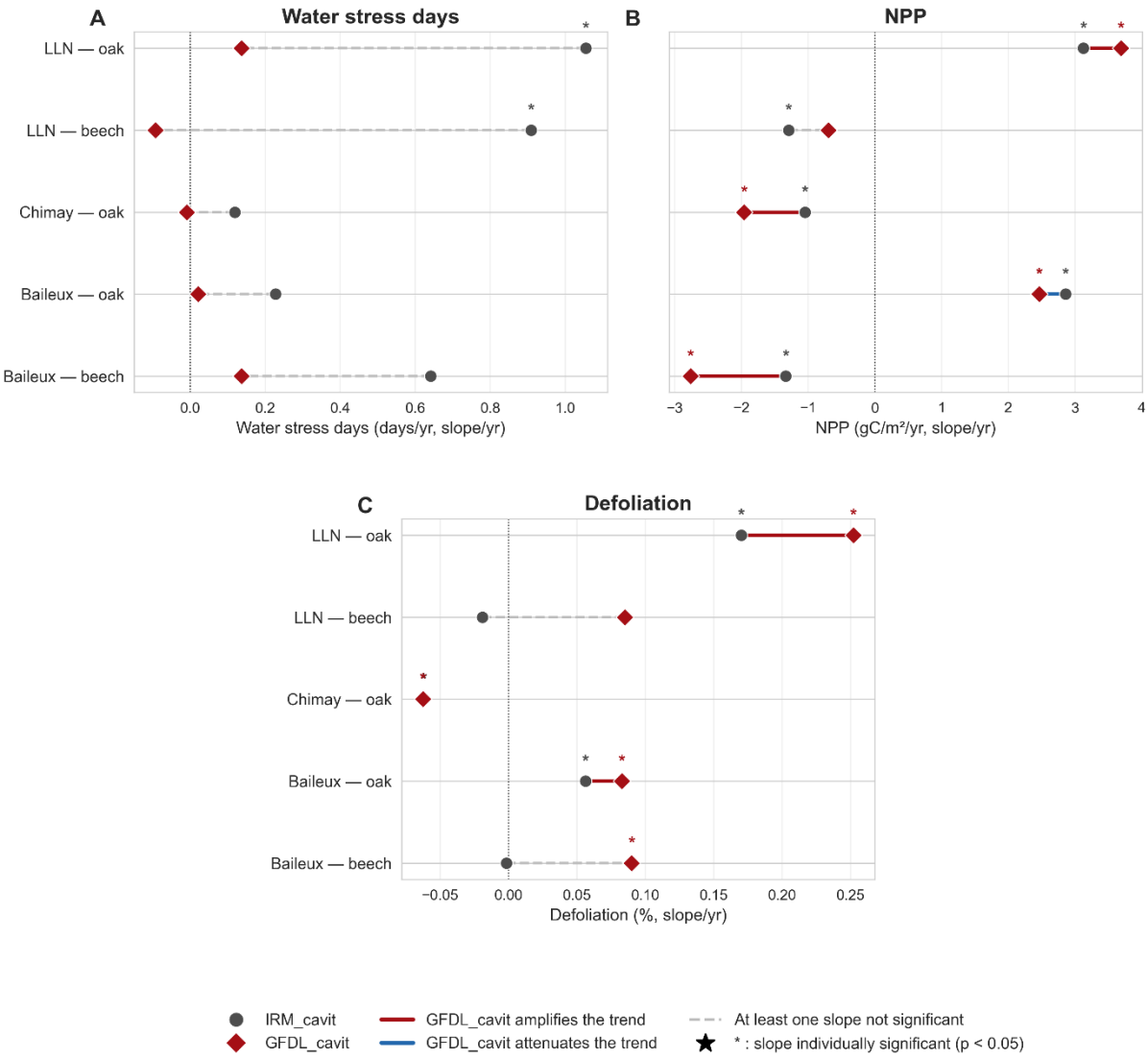

Figure I1 : Comparison of trend slopes (1961-2024) between IRM- and GFDL-ESM4-forced simulations, with cavitation activated in both cases, for water stress days (A), NPP (B), and total defoliation (C). Same conventions as Figure 20 (without cavitation).

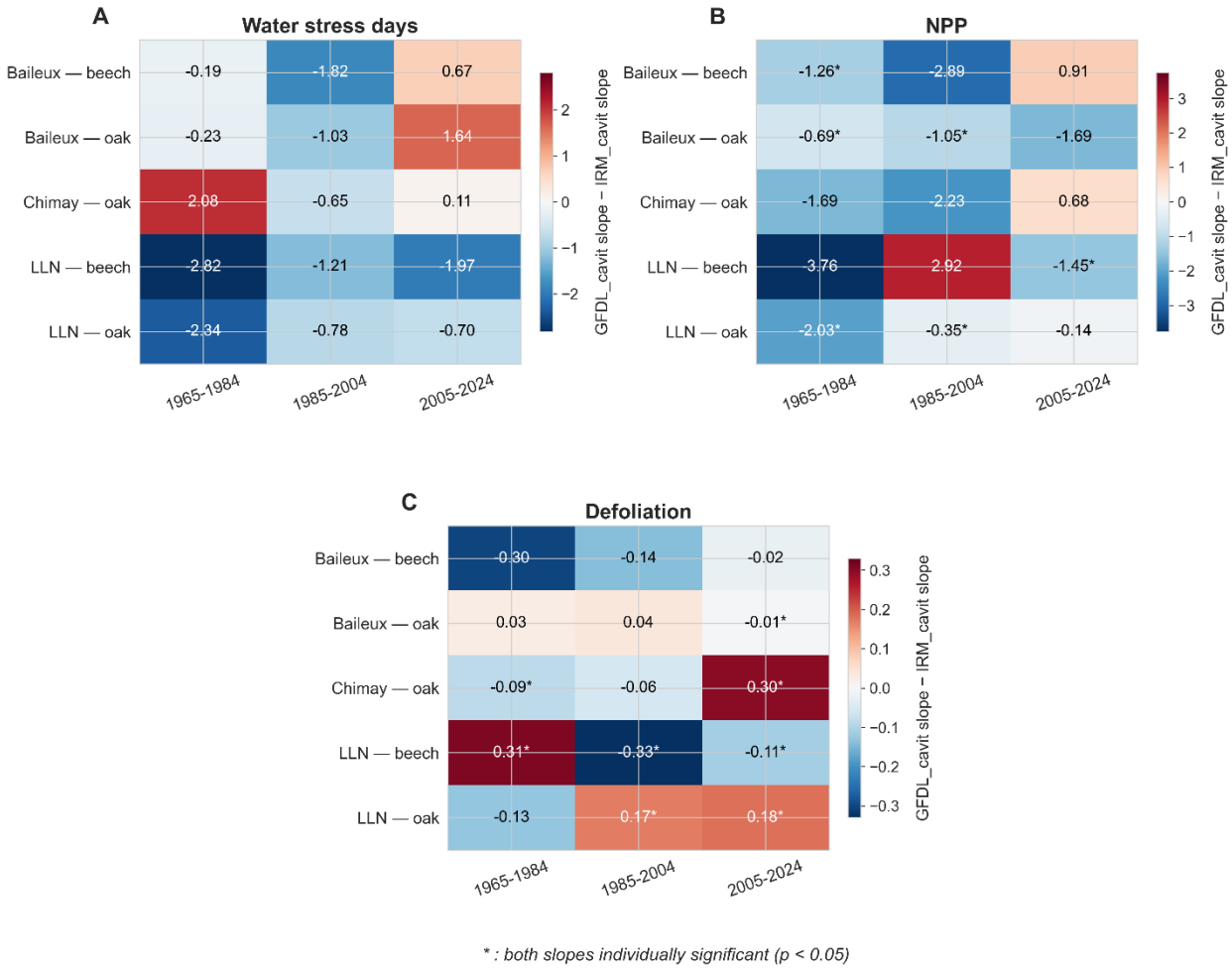

Figure 12 : Slope difference (GFDL-ESM4 − IRM) by 20-year block, with cavitation activated in both cases, for water stress days (A), NPP (B), and total defoliation (C). Same conventions as Figure 21 (without cavitation).

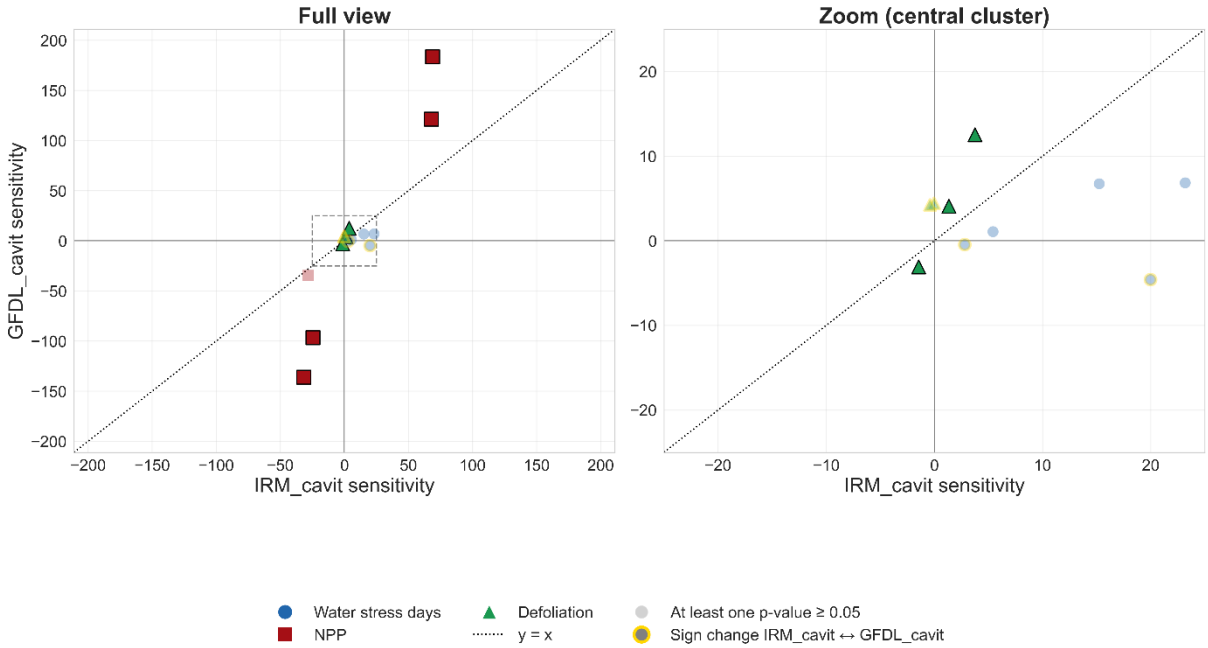

Figure 13 : Sensitivity of each indicator to warming, compared between IRM and GFDL-ESM4, with cavitation activated in both cases. Same conventions as Figure 22 (without cavitation).

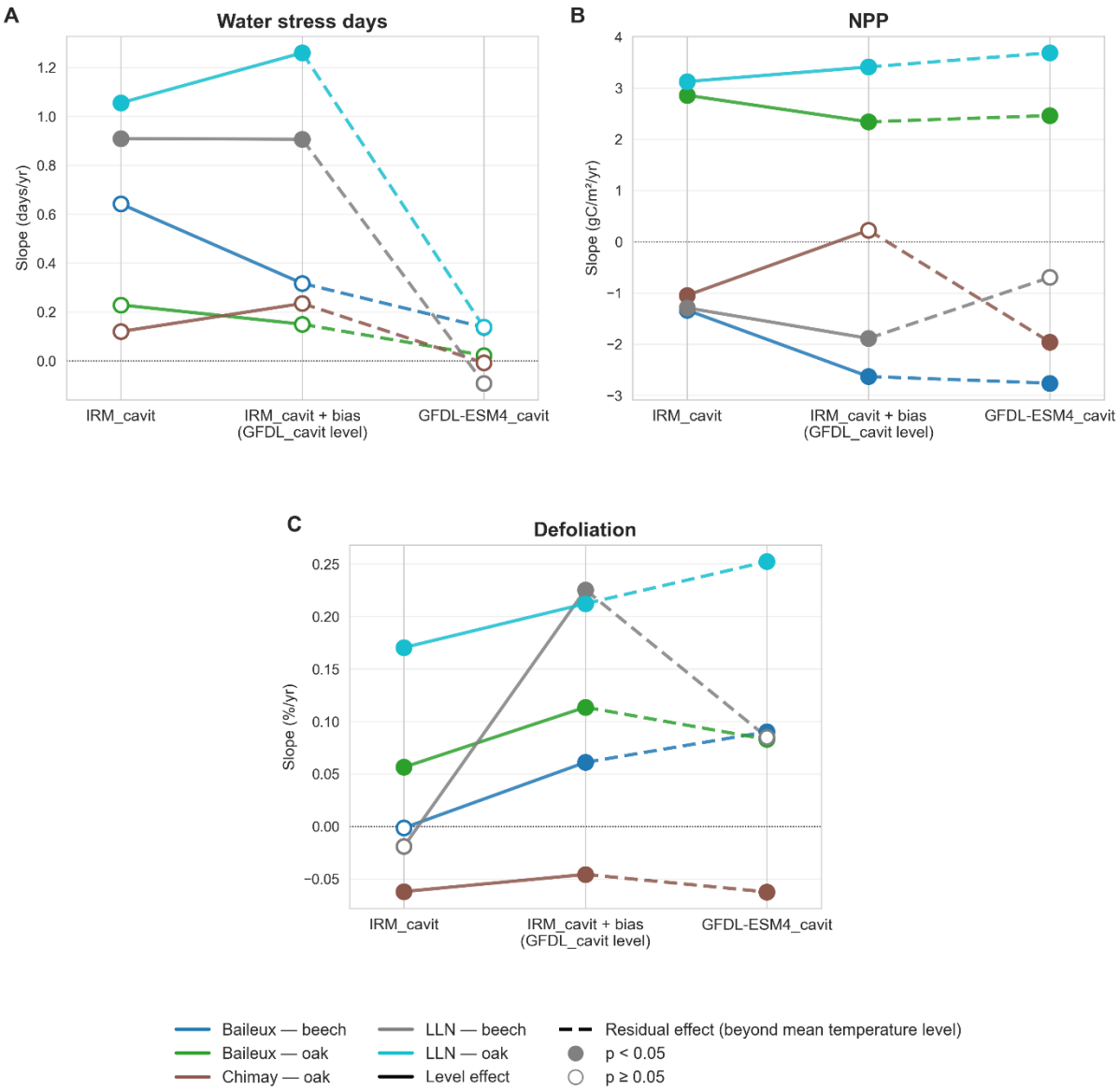

Figure I4 : Trend slope (1961-2024) under three successive climate configurations, with cavitation activated throughout: IRM+cavitation (observed climate), IRM+cavitation+bias (IRM's trend and interannual variability, with mean temperature level adjusted to that of GFDL-ESM4), and GFDL-ESM4+cavitation, for water stress days (A), NPP (B), and total defoliation (C). Same conventions as Figure 23 (without cavitation): the first segment (solid line) isolates the effect of temperature level alone; the second segment (dashed line) isolates a residual effect once this level is equalised, including in particular the climate trend. Each colour represents a site × species combination (see legend). Filled markers indicate a statistically significant slope ($p < 0.05$), open markers a non-significant slope.

Appendix J

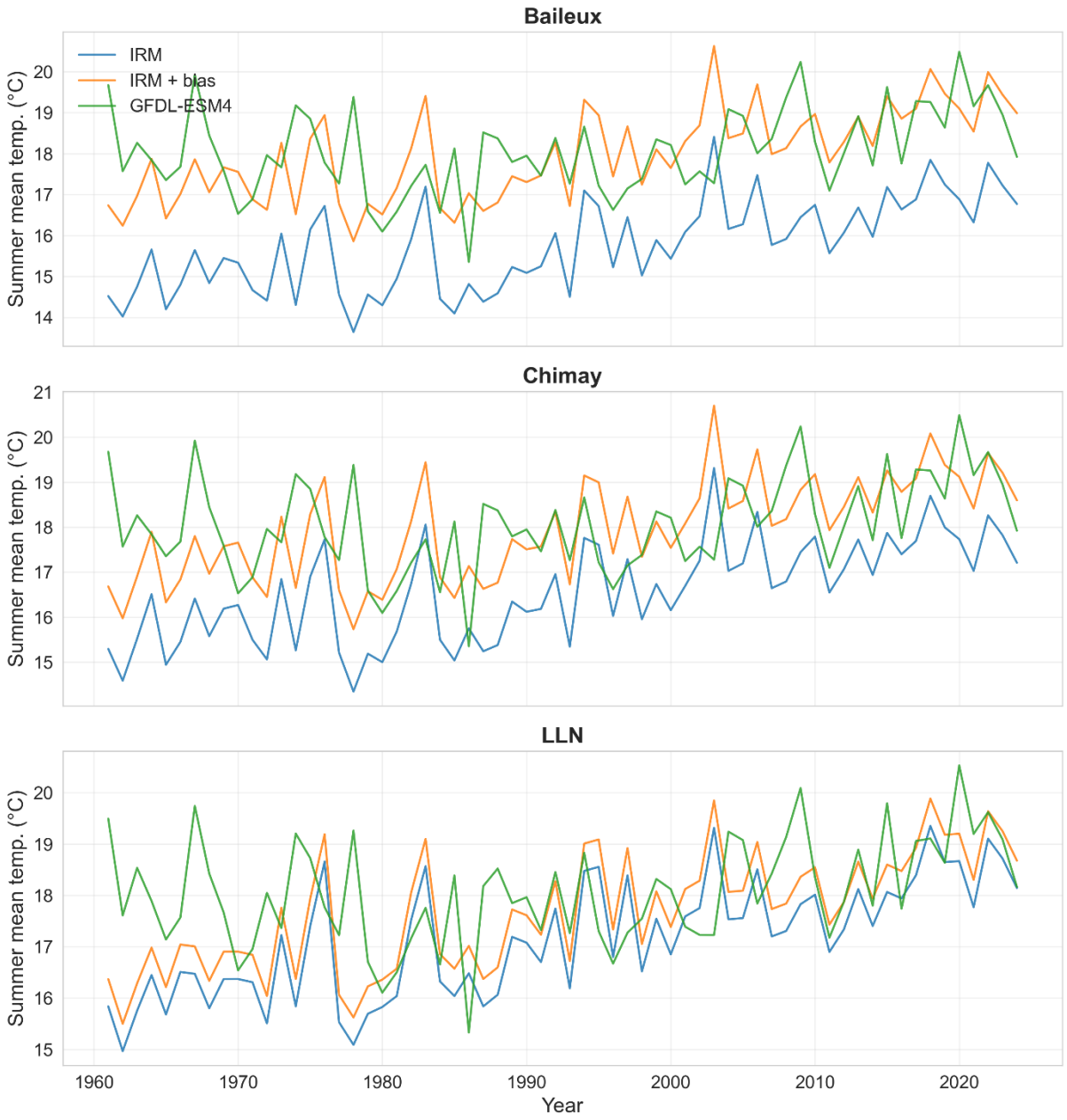

Figure J1 : Summer (June-August) mean temperature time series for the three climate forcings used in the level/residual effect test (section 3.4.3): IRM (observed), IRM+bias (IRM data shifted by a constant offset to reach GFDL-ESM4's mean summer temperature), and GFDL-ESM4, for Baileux, Chimay, and LLN (1961-2024). The close alignment between IRM and IRM+bias confirms that the interannual variability and trend of IRM are preserved in the synthetic dataset, with only the mean level shifted.

Modelling the response of forests to climate change: the impact of drought.

The case of Walloon forests simulated with the HETEROFOR model

Walloon forests cover nearly a third of the region's territory and are increasingly exposed to climate change. However, its precise impact on tree productivity, water stress and vitality remains poorly quantified at the stand scale. This is further complicated by the fact that climate models tend to underestimate the rate of recent warming observed in Europe, which raises questions about the reliability of forest projections based on them. This master thesis addresses both issues: it quantifies how climate change affects Walloon forests using a process-based model, and assesses how far biases in the climate data used propagate into these projections.

The study uses the HETEROFOR model to simulate five stands dominated by common beech and sessile oak across three sites (Baileux, Chimay, Louvain-la-Neuve), chosen to represent the pedo-climatic diversity of Wallonia. Simulations cover the historical period (1961-2024, forced by observed IRM data) and the future period (2025-2100, forced by the GFDL-ESM4 model under scenario SSP3-7.0). Eight simulation configurations were designed to isolate the effects of CO_2 fertilisation and of a hydraulic cavitation module. An additional set of historical simulations forced by GFDL-ESM4 was used to quantify how the biases of this climate model propagate through HETEROFOR.

Water stress is projected to roughly double by 2100, shifting from occasional episodes to a near-permanent condition that leaves trees little time to recover between stress periods. Net primary productivity follows a three-phase trajectory: a moderate historical increase, a peak around 2055–2060, and a subsequent decline that erases most of the gains accumulated over the 20th century, as rising temperature switches from a stimulating to a limiting factor once combined with intensifying water deficit. Sessile oak, owing to a higher hydraulic conductivity, maintains markedly more stable productivity than common beech, whose relationship with temperature deteriorates earlier under stress. Regarding climate model biases, GFDL-ESM4 was found to overestimate absolute temperature levels (+0.9 to +2.3°C depending on the site) while simultaneously underestimating the recent warming trend relative to IRM observations. These two biases pull the projections in opposite directions, and their relative weight varies by site and indicator, so no single correction can be applied uniformly across the results.

Overall, this work shows that Walloon forests face a strong intensification of water stress, and that the window to adapt forest composition before productivity gains are reversed is limited. Sessile oak emerges as a more resilient species than beech under these conditions, supporting its promotion, together with broader species diversification, as an adaptation strategy. The analysis of climate model biases also shows that they do not simply make the projections too pessimistic or too optimistic overall: their effect depends on the site and indicator considered and cannot be corrected with a single adjustment.

UNIVERSITÉ CATHOLIQUE DE LOUVAIN
Faculté des bioingénieurs
Croix du Sud, 2 bte L7.05.01, 1348 Louvain-la-Neuve, Belgique | **www.uclouvain.be/agro**